Development of a snow avalanche warning system

（雪崩発生危険度予測システムの構築）

KOMATSU, Asami

（小松　麻美）

A dissertation for the degree of Doctor of Science
Department of Earth and Environmental Sciences,
Graduate School of Environmental Studies, Nagoya University

（名古屋大学大学院環境学研究科

地球環境科学専攻

学位論文　博士（理学））

2021

Abstract

In this research, we have developed a snow avalanche warning system primarily to evaluate the hazard to traffic. At present, Japanese road administrators monitor the snow avalanche hazard only by measuring snowfall amounts. However, this simple method is not always able to estimate avalanches precisely, as additional factors such as the existence of weak layers in the snowpack and slope angle are involved in avalanche release.

Sophisticated snow-cover models, such as SNOWPACK (Bartelt and Lehning, 2002; Lehning et al., 2002) and Crocus (Brun et al., 1989, Vionnet et al., 2012) which consider numerous physical processes, require various meteorological inputs. However, the currently available datasets in Japan have a 20-km grid spacing and are updated every 6-hours. They are far from satisfactory because snow properties are very sensitive to weather conditions and can change rapidly. These limitations can be overcome by using the precipitation and surface air temperature products available on a 1-km grid, which are updated every hour.

In this study, we have developed a simple snow-cover model (SSCM) that requires only air temperature and precipitation or snow depth data as inputs. The model is intended to describe grain type, temperature, and density profiles, as well as evaluate the avalanche hazard. The physical processes incorporated into the SSCM were greatly simplified. Therefore, the simulation requires only limited computing power and allows the user to

generate numerous simulations within a short period over a wide area and at small grid scales.

After introducing the model configuration of SSCM, we have compared the model outputs with the snowpack observations. Then, application to the avalanche incidents were carried out. The SSCM can reproduce changes in snowpack properties having good accuracy that is comparable to the more sophisticated model like SNOWPACK. Comparison with the avalanche incidents also suggest the suitability of the SSCM.

On the other hand, wind causes snowdrift and non-uniform snow can accumulate, which sometimes increases the avalanche risk. The system should also consider the effect of wind over complex topography. In fact, the Stability Indexes: SIs calculated for a couple of avalanche cases are apparently larger than the values which is critical for the avalanche release. Then, we recognized the effect of snow drifts should be incorporated into the system to make it more precise.

Thus, as a next step, we developed a system to calculate snow transport and deposition across complex topography and coupled this system to the SSCM. We then applied this coupled model to the Niseko area, Hokkaido, Japan. For this target area, we have used anemometers to verify the performance of air flow simulations. Also. we assigned the wind tunnel and moving vehicle observation data to compare with calculations. For snowdrift simulation results, we used the snowdrift observations and the wind tunnel observation using the activated cray to verify the modeled snowdrift distributions. Additionally, we have calculated SI results for a strong wind case in Niseko (no avalanche) and an avalanche case in Wakkanai by the SSCM. Both results are compatible for the situation of avalanche risks.

At this stage, the avalanche warning system is mainly focused on the surface avalanche, and it doesn’t cover the full-depth avalanches in early spring when the highest air temperature is continued to be over zero degree. Considering the snow melting process precisely we would like to improve the system, which is able to forecast the danger of not only the dry snow avalanches but also the wet ones, before long.

Table of contents

I. Introduction

Snow avalanche-prone locations in Japan range from small roadside slopes to mountain ski resorts. The most common avalanche type that affects roads in winter are dry-snow slab and dry loose snow avalanches, which are usually caused by the release of a new snow layer that accumulated during a heavy snowfall over a short period. Fig. 1.1. shows a typical example and Fig. 1.2. clearly indicates the number of snow avalanches, released along the roadside, occupy the large part of the total. Further, many surface avalanches have occurred along the national road network, not only in the snowy region along the Sea of Japan, but also in the region of Tohoku on the Pacific coast. Although the latter is typically seen as a warmer region that is less affected by snowfall, since 2010 it has experienced heavy snowfall events generated by cyclones that developed rapidly along the south coast of Japan. In particular, during February 2014 a record-breaking snowstorm caused nearly 100 avalanches (Izumi et al., 2014) and more than 130 villages were isolated (Kamiishi and Nakamura, 2016). Consequently, the Ministry of Land, Infrastructure, Transport and Tourism (MLIT) of Japan instructed road administrators to enforce traffic restrictions when heavy snowfall is predicted.

The Japan Meteorological Agency (JMA) issues “Avalanche warning” during winters. However, their method depends only on the air temperature and the estimated storm snow depth. Moreover, the warning covers an area as large as a prefecture (i. e. about 4,000 km^2).

Full-depth avalanches occasionally develop from pre-existing cracks and/or folds in the snow cover. However, no clear warning signs of impending slope failure are evident prior to the release of dry-snow slab and dry loose snow avalanches. At present, Japanese road administrators monitor the snow avalanche hazard only by measuring snowfall amounts. However, this simple method is not always able to estimate avalanches precisely, as additional factors such as the existence of weak layers in the snowpack and slope angle are involved in avalanche release.

In order to develop more precise snow avalanche danger prediction system, first of all, a snow-cover model that describes the change in accumulated snowpack properties with time and the meteorological conditions. Sophisticated snow-cover models, such as SNOWPACK (Bartelt and Lehning, 2002; Lehning et al., 2002) and Crocus (Brun et al., 1989, Vionnet et al., 2012), consider numerous physical processes, which are carefully reviewed by Morin et al. (2019). Both models require various meteorological inputs, including downward short- and longwave radiation. However, the currently available datasets generated by the Global Spectral Model and provided by the Japan Meteorological Business Support Center have a 20-km grid spacing and are updated every 6-hours. They are far from satisfactory because snow properties are very sensitive to weather conditions and can change rapidly. These limitations can be overcome by using the precipitation and surface air temperature products available from the Japan Meteorological Agency (JMA) on a 1-km grid, which are updated every hour.

On the other hand, local variations in the deposition of snow and the redistribution of the previously deposited snow are governed by the interaction between topography and wind. Wind speed variations over the complicated terrain, and in particular, the subsequent erosion of snow from a ridge and deposition in a valley are key factors for determining the avalanche danger in a target area. However, Japanese avalanche warning systems rarely consider heterogeneous snow distributions in mountainous regions when assessing potential snow avalanche hazards.

Lehning et al. (2008) developed the Alpine3D numerical model, which incorporates high-resolution wind fields that are calculated using the ARPS meso-scale atmospheric model (Xue et al., 1995), to evaluate the snow distribution across steep alpine terrain. Vionnet et al. (2017) also simulated snow accumulation in alpine terrain using the Meso-NH/Crocus fully coupled snowpack/atmosphere model. The former is a non-hydrostatic atmospheric model (Lafore et al., 1998), and the latter is a detailed snowpack model (Brun et al., 1992).

In this study, firstly, a simple snow-cover model (SSCM), that requires only air temperature and precipitation or snow depth data as inputs, was developed. The model is intended to describe grain type, temperature, and density profiles, as well as evaluate the avalanche hazard. The physical processes incorporated into the SSCM were greatly simplified. Therefore, the simulation requires only limited computing power and allows the user to generate numerous simulations within a short period over a wide area and at small grid scales. “Simple” means that this model needs a few input data without snow details, thus this requires shorter time. Short computation time has the advantage for warning system. Then the performance of the model is verified by comparing with snow pit observations and previous avalanche incidents.

Secondary, a system to calculate snow transport and deposition across complex topography was developed and coupled to the SSCM. Then it was then applied to the Niseko ski area in Hokkaido, Japan to assess potential snow avalanche hazards. Although the altitude of Mt. Annupuri is only about 1300 m above sea level (a.s.l.), the snow is completely dry in winter and very popular among skiers. Therefore, the local communities and ski area managers strongly desire a more precise avalanche warning system. Furthermore, the local government and National Research Institute for Earth Science and Disaster Resilience (NIED) have established six anemometers across the target area, which can be used to verify the performance of this procedure. We also attempted to simplify the procedures as much as possible to reduce the computational requirements of the model and generate numerous simulations within a short period, which is ideal for modeling a range of snow avalanche scenarios in near real-time.

In this thesis, we describe our processes and achievements to develop the snow avalanche warning system. In Chapter II, we introduce the simple snow-cover model (SSCM). After showing the motivation of the research, previous works including the sophisticated models of SNOWPACK and Crocus are briefly introduced. Then, the model description of SSCM is explained. Following the comparison between the model output and the snow pit observations, we applied the SSCM to the snow avalanche incidents in Japan. Limitation of the model and the future work are also pointed out. Chapter III is the snowdrift simulation part. Subsequently to the brief introduction of the previous work, our strategies to simulate the wind distribution, the blowing snow and, consequently, the snow drift are described. In addition to the field observations, wind tunnel experiments and moving vehicle observations in order to evaluate the model output are introduced, and finally in Chapter IV, we summarize the conclusive results of the present work and give the future scope.

Fig. 1.1. A surface snow avalanche released from the roadside slope in Hokkaido, Japan.

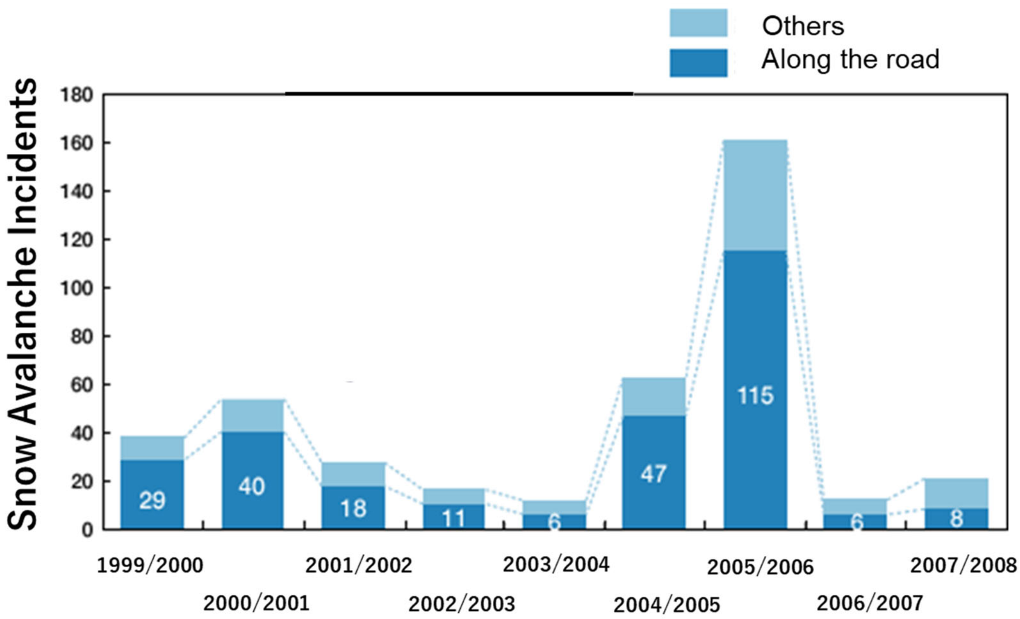

Fig. 1.2. Number of the snow avalanche incidents.

(Cited from "https://www2.ceri.go.jp/snow/nadare/06.html" and partly modified)

II. A simple snow-cover model for Avalanche Warning in Japan

1. Introduction

Avalanche-prone locations in Japan range from small roadside slopes to mountain ski resorts. The most common avalanche type that affects roads in winter are dry-snow slab and dry loose snow avalanches, which are usually caused by the release of a new snow layer that accumulated during a heavy snowfall over a short period. Recently, many avalanches have occurred along the national road network, not only in the snowy region along the Sea of Japan, but also in the region of Tohoku on the Pacific coast. Although the latter is typically seen as a region that is less affected by snowfall, since 2010 it has experienced heavy snowfall events generated by cyclones that developed rapidly along the south coast of Japan. In particular, during February 2014 a record-breaking snowstorm caused the historical maximum snow depth of 114 cm at Koufu, Yamanashi and nearly 100 avalanches were recorded (Izumi et al., 2014) and more than 130 villages were isolated (Kamiishi and Nakamura, 2016). Consequently, the Ministry of Land, Infrastructure, Transport and Tourism (MLIT) of Japan instructed road administrators to enforce traffic restrictions when heavy snowfall is predicted.

Full-depth avalanches occasionally develop from pre-existing cracks and/or folds in the snow cover. However, no clear warning signs of impending slope failure are evident prior to the release of dry-snow slab and dry loose snow avalanches. At present, Japanese road administrators monitor the snow avalanche hazard only by measuring snowfall amounts. However, this simple method is not always able to estimate avalanches precisely, as additional factors such as the existence of weak layers in the snowpack and slope angle are involved in avalanche release.

Sophisticated snow-cover models, such as SNOWPACK (Bartelt and Lehning, 2002; Lehning et al., 2002) and Crocus (Brun et al., 1989, Vionnet et al., 2012), consider numerous physical processes, which are carefully reviewed by Morin et al. (2019). Both models require various meteorological inputs, including downward short- and longwave radiation. However, the currently available datasets generated by the Global Spectral Model and provided by the Japan Meteorological Business Support Center, do not include radiation data. In contrast, predictions of precipitation amount and air temperature are readily available and relatively accurate. Schmucki et al. (2014) used the SNOWPACK model to calculate the snow depth and the snow water equivalent using input data that are commonly available from an automatic weather station (AWS). As the radiation flux was not measured, parameterized radiation fluxes were applied, and the model outputs were compared with the field observations. Although the model performed well in general, no detailed discussion was provided of the snowpack properties, such as profiles of snow type, density, temperature, and the shear strength of snow, which are known to be key factors in avalanche release. Further, we have to note that the data by the Japan Meteorological Business Support Center have a 20-km grid spacing and are updated every

6-hours. They are far from satisfactory because snow properties are very sensitive to weather conditions and can change rapidly. These limitations can be overcome by using the precipitation and surface air temperature products available from JMA on a 1-km grid, which are updated every hour.

In this study, we have developed a simple snow-cover model (SSCM) that requires only air temperature and precipitation or snow depth data as inputs. The model is intended to describe grain type, temperature, and density profiles, as well as evaluate the avalanche hazard. The physical processes incorporated into the SSCM were greatly simplified. Therefore, the simulation requires only limited computing power and allows the user to generate numerous simulations within a short period over a wide area and at small grid scales.

In this chapter, we provide an outline of our SSCM. Although it has been developed aiming for the operational avalanche warning, we use the observed meteorological data and the performance of the model is verified by comparing with snow pit observations and previous avalanche incidents.

2. Data and study methods

2.1 Model description

The process used to generate the avalanche warnings, including the estimate of snowpack properties simulated by the SSCM, is shown schematically in Fig. 2.1. The calculations are run from two to three days before the snowfall and the outputs are the snow properties from the snow surface to the base of the newly fallen snow every hour. The only inputs to the model are air temperature and precipitation or snow depth. The hourly snowfall amount is added to the snowpack as a new layer and its temperature is set to the air temperature. In the present study, we assume rainfall did not occur during the study period. Other snowpack properties (e.g., snow density, thickness, grain type, and shear strength from the surface to the bottom) are estimated for each layer. Then, by considering the slope angle, the snow stability index (SI: the ratio of shear stress to the snow's shear strength, see Fig. 2.2.) is estimated.

Our model estimates the possibility of an avalanche being released during a storm or over a couple of days following a snowfall. This is because the potentially weak layers are located mostly within or just below the newly accumulated snow. This differs from other detailed models, such as SNOWPACK and Crocus, in which the simulations are carried out for the entire depth of the snow cover.

Ideally, the snow temperature should be obtained by solving the heat transfer equation. However, in this study, in order to make all the processes as simple as possible, we applied the procedures shown below. Since we use hourly snowfall to set one layer, the thickness of each layer is supposed to be fairly small. Thus, the snow temperature at time i and depth j, $T_s(i,j)$ (°C), can be set using the approach by Suizu (2002) that considers each layer and its adjacent layers at one time step before using Eq. (2.1), as follows:

$$T_s(i,j) = \frac{\left(T_a(i-1) + T_a(i)\right)}{2} \qquad j = 1$$

$$T_s(i,j) = \frac{\left(T_s(i-1,1) + T_s(i,1) + T_s(i-1,2)\right)}{3} \qquad j = 2$$

$$T_s(i,j) = \frac{\left(T_s(i-1,j-2) + T_s(i-1,j-1) + T_s(i-1,j)\right)}{3} \qquad for\ j \geq 3 \tag{2.1}$$

The precipitation amount, given as input p in kg m^{-2}, is converted to the new snowfall depth H_0 (m) according to the new snow density ρ_0 in kg m^{-3}:

$$\rho_0 = \begin{cases} 54 & for\ T_a \leq -2\ °C, \\ 79 + 12.5\ T_a & for\ T_a > -2\ °C \end{cases} \tag{2.2}$$

Equation (2) was developed by Suizu (2002) based on the observations of Endo et al. (2002) and Kajikawa (1989), where T_a is the air temperature.

Except for the surface layer, the snow density is derived from viscous compression theory. The density of a layer at time i is derived from that at $i-1$ and the overburden pressure caused by the snow layers above. Endo et al. (2004) derived the relationship between the viscosity coefficient and the density based on several observations made by Kojima (1967), Nakamura (1988), Kajikawa and Ono (1990), Yamanoi and Endo (1998), and others. The viscosity coefficient η (Pa s) is defined as follows:

$$\eta = \begin{cases} C_1 \rho^{a} & for\ \rho \leq 200\ kg\ m^{-3} \\ C_2 \exp(k\rho) & for\ \rho > 200\ kg\ m^{-3} \end{cases} \qquad (2.3)$$

where C_1 is $1.78\exp(-0.0958\,T_s)$, C_2 is $3.44 \times 10^{6}\exp(-0.0958\,T_s)$, and a and k are 3.69 and 0.0253, respectively. Using the above procedures, temporal evolution of the thickness H of each snow layer can be obtained.

We classified the grain type using the scheme of Saito and Enomoto (2003). This scheme uses the effective temperature gradient g_t, which was introduced by Yamazaki (2001), to identify the point where depth hoar (DH) begins to form, and g_t is defined as follows:

$$g_t = \begin{cases} \Gamma\, f(T_s) & for\ \Gamma \geq 10\ ^{\circ}\mathrm{C}\ m^{-1} \\ 0 & for\ \Gamma < 10\ ^{\circ}\mathrm{C}\ m^{-1} \end{cases} \qquad (2.4)$$

Here, $\Gamma = \frac{\partial T_s}{\partial z}$ is the temperature gradient, and,

$$f(T_s) = \frac{D_v(T)\delta(T)}{D_v(T_0)\delta(T_o)} \cong 1 + 0.073T_s + 0.00197{T_s}^{2} + 0.0000187{T_s}^{3}$$

$$for -40\ ^{\circ}\mathrm{C} \leq T \leq 0\ ^{\circ}\mathrm{C}\ and\ T_0 = 0\ ^{\circ}\mathrm{C} \qquad (2.5)$$

D_v is the diffusion coefficient of water vapor and δ is the differential coefficient of saturated vapor density with respect to temperature. Both decrease as temperature decreases. The time integral G_t of g_t can be expressed as:

$$G_t(t + \Delta t) = G_t(t) + g_t\,\Delta t \qquad (2.6)$$

Based on G_t and the snow density ρ, the grain type can be classified as decomposing and fragmented precipitation particles (DF), rounded grains (RG), faceted crystals (FC), or DH as is shown in Fig. 2.3. Grain types and their characteristics can be found in the International Classification for Seasonal Snow on the Ground (Fierz et al., 2009). Symbols and the two-letter upper case abbreviation codes of the main morphological grain shape classes are introduced in Appendix A with the specific characteristics.

When the grain type is classified as precipitation particles (PP) or DF or RG, the shear strength of snow can then be calculated as follows (Yamanoi and Endo, 2002):

$$\sigma_A = 9.40 \times 10^{-4} \rho^{2.91} \qquad (2.7)$$

where σ_A is in Pa.

If instead the grain type is classified as FC or DH, the shear strength is set as follows (Abe et al., 2005):

$$\sigma_B = 3.91 \times 10 \exp(10^{-2} \rho) \qquad (2.8)$$

where σ_B is expressed in Pa.

Consequently, the shear strength of the snow differs significantly depending on whether G_t is greater than 29 (°C cm^{-1} h) or not, and whether the grain type is hoar or not, even for a given snow density. Thus, to bridge the gap between Eq. (2.7) and Eq. (2.8), we added Eq. (2.9) to our calculation procedures:

$$\sigma = -\frac{G_t - 19}{39 - 19}(\sigma_A - \sigma_B) + \sigma_A \qquad for\ 19 < G_t < 39 \ (°\mathrm{C}\ cm^{-1}\ \mathrm{h}) \qquad (2.9)$$

where σ is also expressed in Pa.

Finally, the snow stability index (SI_j) , which is the ratio of shear strength to shear stress in the snow as is shown in Fig. 2.2, can be calculated as:

$$SI_j = \frac{\sigma}{\left(\sum_{j=1}^{n} \rho_j H_j g\right) \sin\theta} \qquad (2.10)$$

where θ is the slope angle, ρ_j is the snow density of the layer at the depth j, and H_j is the snow thickness over the depth j.

Perla (1977) reviewed 80 avalanche cases and found that the average SI value was 1.66, with a standard deviation of 0.98; the minimum value was 0.19, and the maximum value was 6.4. He also concluded that SI < 1.5 is critical for avalanche release. Further, Sommerfeld (1984) suggested that SI ≤ 1.5 is the threshold for avalanche risk. In Japan, Hirashima et al. (2006, 2008) indicated that an SI threshold of 2 was appropriate for evaluating avalanche susceptibility.

The snow melting process was also incorporated into the model. We used the degree-hour method by applying the degree-day method by Kojima et al. (1983). The amount of snow melt M_h (m h^{-1}) is obtained from

$$M_h = \kappa \frac{T_a}{\rho_{ss}} \qquad (2.11)$$

where ρ_{ss} (kg m^{-3}) is the density of the surface snow, and κ (m °C^{-1} h^{-1}) is the degree-hour factor that is derived from the degree-day factor κ_{day} (cm °C day^{-1}) as follows:

$$\kappa = \frac{\kappa_{day}}{24} \qquad (2.12)$$

We set κ_{day} to 5.0, as derived from snowmelt observations in a mountainous area by Kawashima et al. (2002).

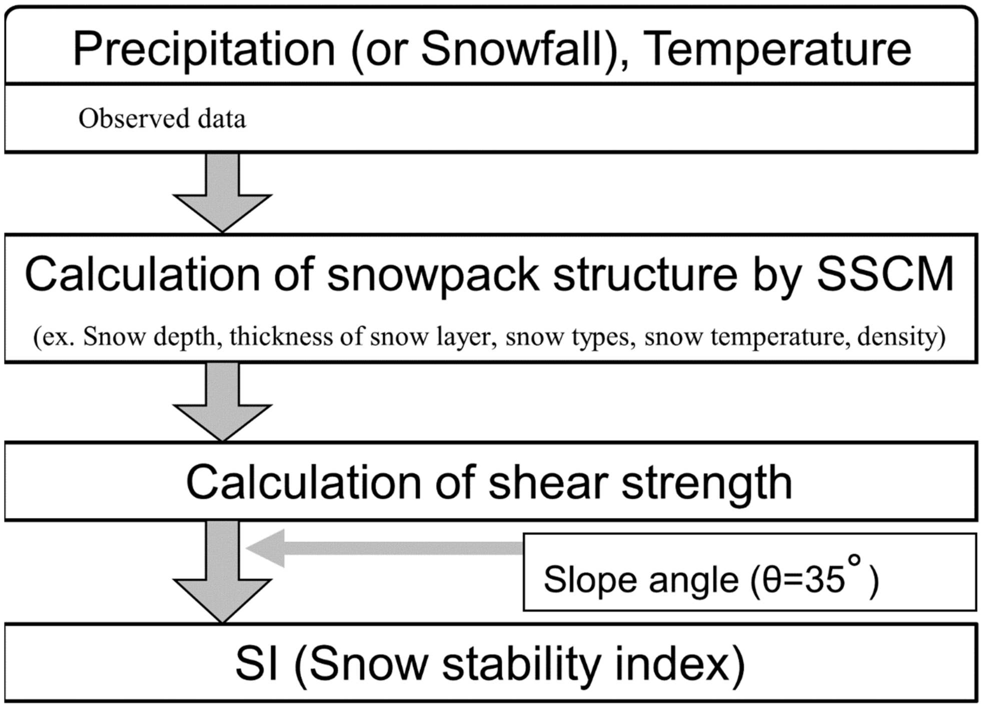

Fig. 2.1. Schematic diagram of the simple snow cover model (SSCM).

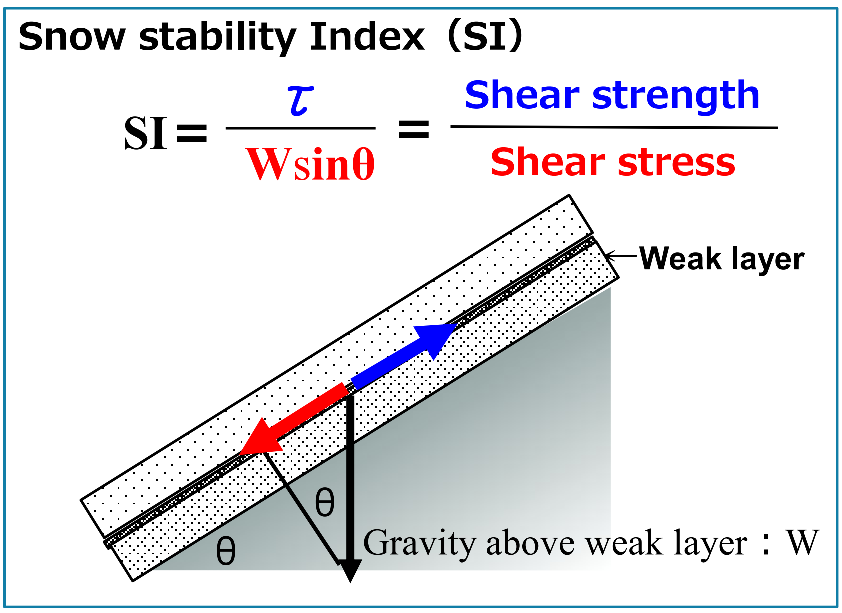

Fig. 2.2. A conceptual diagram of Snow stability index (SI).

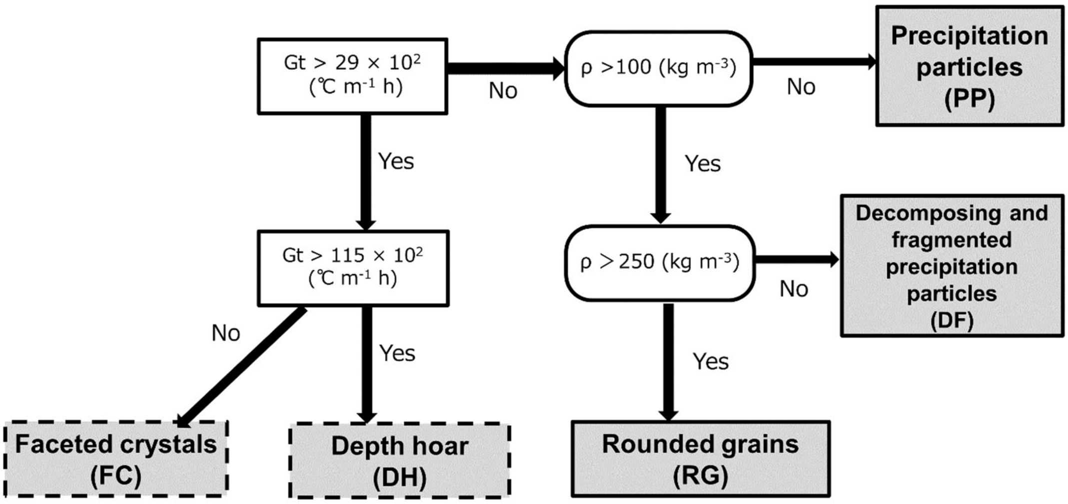

Fig. 2.3. SSCM classification of snow type.

Here, T_a (°C) is air temperature, ρ (kg m^{-3}) is snow density, and G_t (°C m^{-1} h) is the time integral of the effective temperature gradient introduced in Eq. (2.6).

2.2 Observed data and avalanche incidents for model evaluations

Eight snow pit observations were carried out at Mikuni Pass and two at Kiritachi Pass, in Hokkaido (Fig. 2.4.). Fig. 2.5. shows the observed snow profiles at Mikuni Pass. After 40 cm of new snowfall on 25 January, 2013, measurements were conducted every four hours from 27 to 29 January, 2013. Meteorological elements were measured every 10 minutes at an automatic weather station (AWS) operated by the Hokkaido Regional Development Bureau (RDB), Ministry of Land, Infrastructure, Transport and Tourism (MLIT). Meteorological data from 25 to 29 January, 2013 are shown in Fig. 2.6. After 40 cm of new snow fell on 25 January, 2013, the temperature decreased rapidly towards the morning of 26 January, 2013 and then remained around –12 °C.

The snow pit observations were performed approximately 10 m from the AWS; snow temperature, density, and grain type were measured every 10 cm. Further, the shear strength of the snow was observed directly using a shear frame near the bottom, and also indirectly every 10 cm via snow hardness measurements using a push–pull gauge. In the latter case, the values obtained were converted into shear strength following Yamanoi et al. (2004), who derived the following relationship:

$$\sigma = 0.0180 S^{1.18} \qquad (2.13)$$

where S (Pa) is snow hardness and σ (Pa) is the shear strength. Evaluations were also carried out for other nine pit observations.

FC was detected as a weak layer at a depth of 50 cm below the snow surface. Hereafter, we focus on the snow above this weak layer and investigate the changes in the snow properties. During the observation period, the snow type above the weak layer was mostly DF. The grain type in the weak layer changed from FC to DH, and its shear strength decreased.

Further, we calculated SI values using the SSCM for 12 avalanche events in Japan listed in Fig. 2.4. Two cases among them are introduced below.

First one is the snow avalanche broke out at Sekiyama Pass (No. 10 in Fig. 2.4. and Fig. 2.7., 670 m above sea level), Miyagi in 2014. On February 15, 2014, a developing cyclone moved northwards up the east coast of Japan and delivered a large amount of snow. At Sekiyama Pass, a large dry surface avalanche was released at around 09:55 on February 15 and blocked the highway for 10 days. More detailed description can be found in Abe et al. (2016). Meteorological data collected by JMA at their Nikkawa AMeDAS station, which is about 10 km from the pass and 400 m lower in elevation, are shown in Fig. 2.8. Nearly 30 cm of new snow accumulated before the avalanche release. The air temperature was in the range of –4 to –1 °C.

Second one was released at Notsuka pass, Hokkaido in 2018. On February 5–6, 2018, a stationary cyclone delivered a large amount of snow to the mountain passes of Hokkaido. At Notsuka Pass (Fig. 2.4.; 522 m above sea level), an avalanche was released at around 1600 JST on February 5 and blocked the highway for 20 hours. Meteorological data collected at the AWS station by the Hokkaido RDB, which is 1.4 km away and 60 m higher than the avalanche site, showed nearly 40 cm of new snow had accumulated over the preceding two days and the air temperature was in the range –8 to –5 °C, as shown in Fig. 2.9.

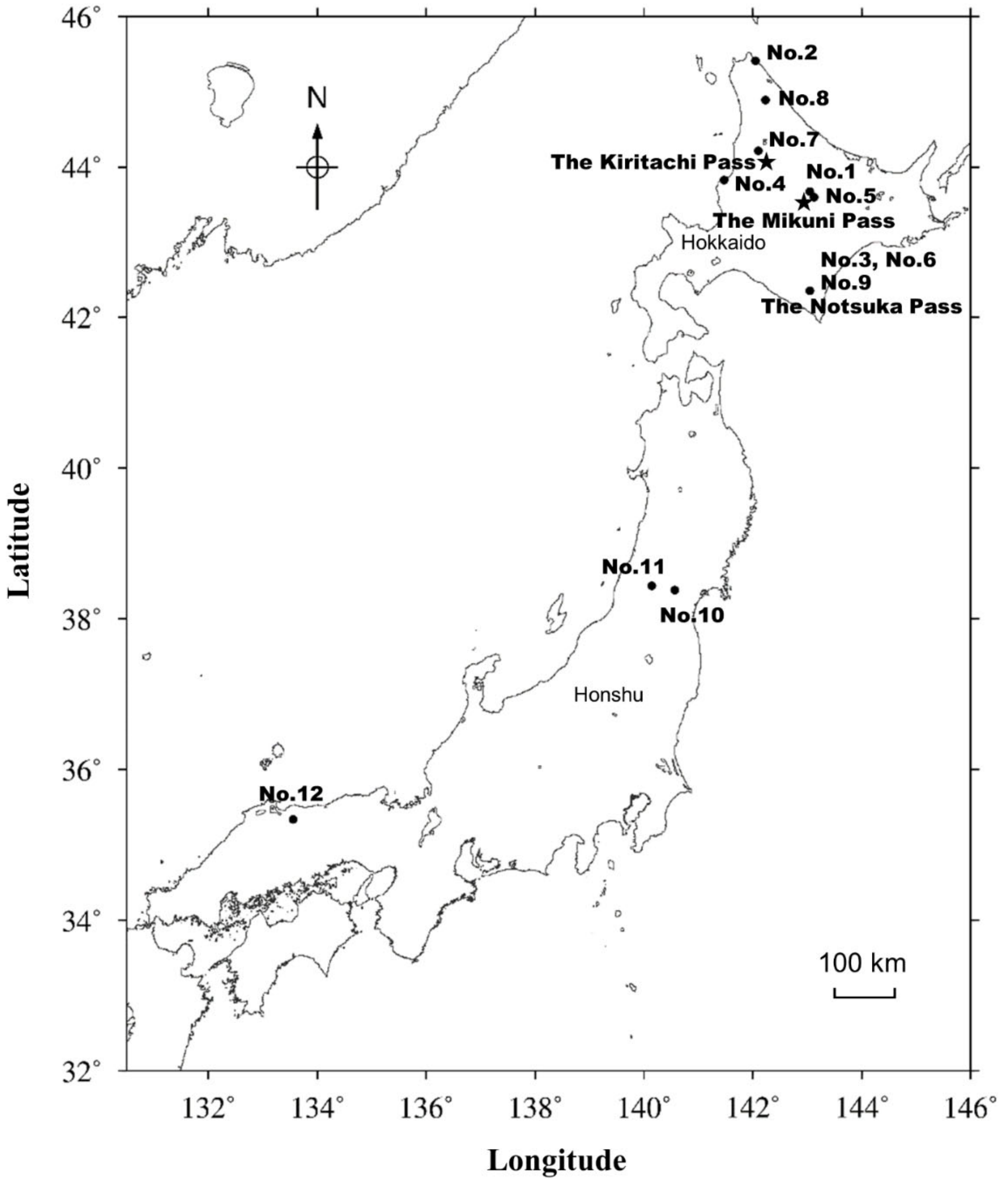

Fig. 2.4. Location of the study sites showing (★) snow pit observations in Table 2.1. and (●) avalanche cases in Table 2.2.

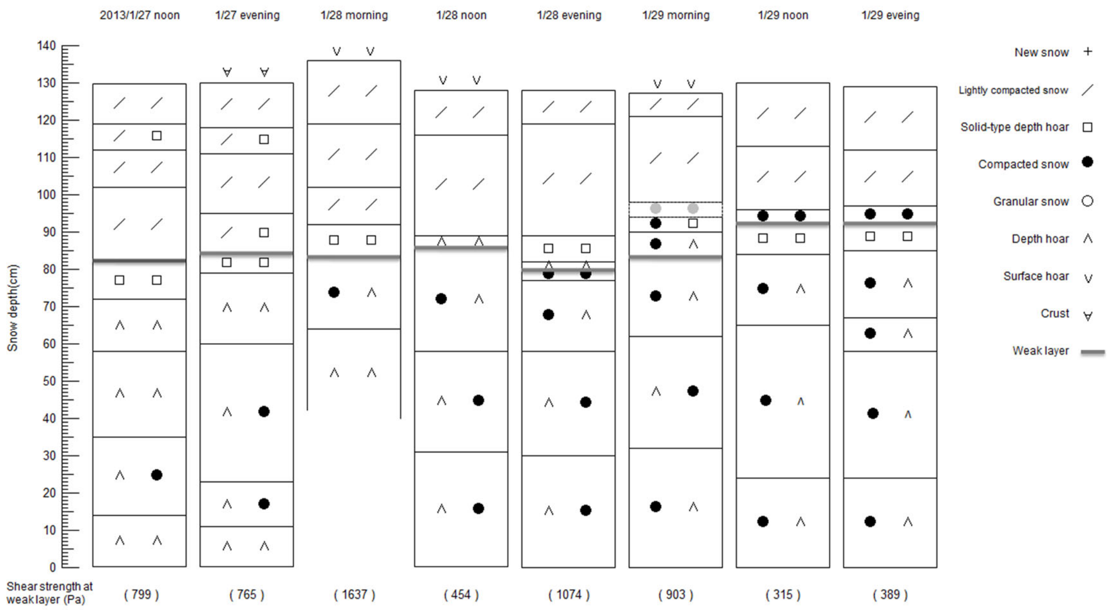

Fig. 2.5. Observed snow profiles at Mikuni Pass for January 27–29, 2013. The heavy gray line indicates the weak layer. The shear strength of this weak layer is provided in parentheses, under the profiles.

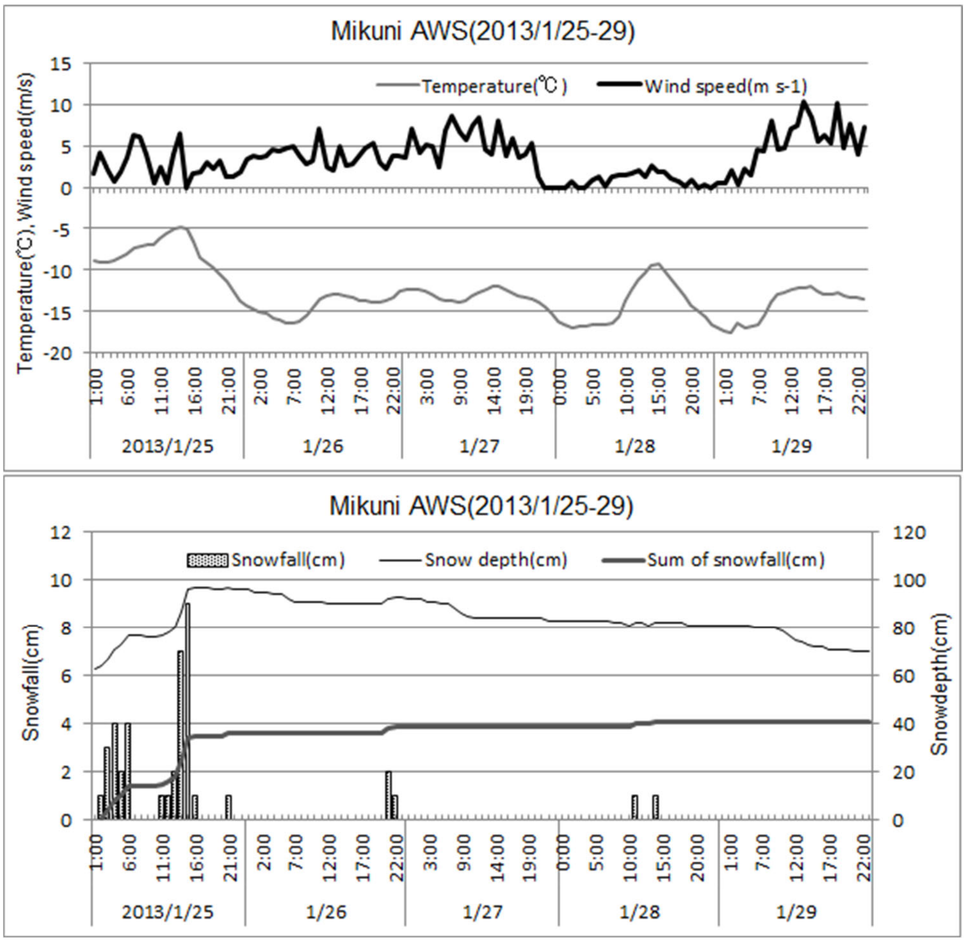

Fig. 2.6. Time series of weather conditions at Mikuni AWS for January 25–29, 2013.

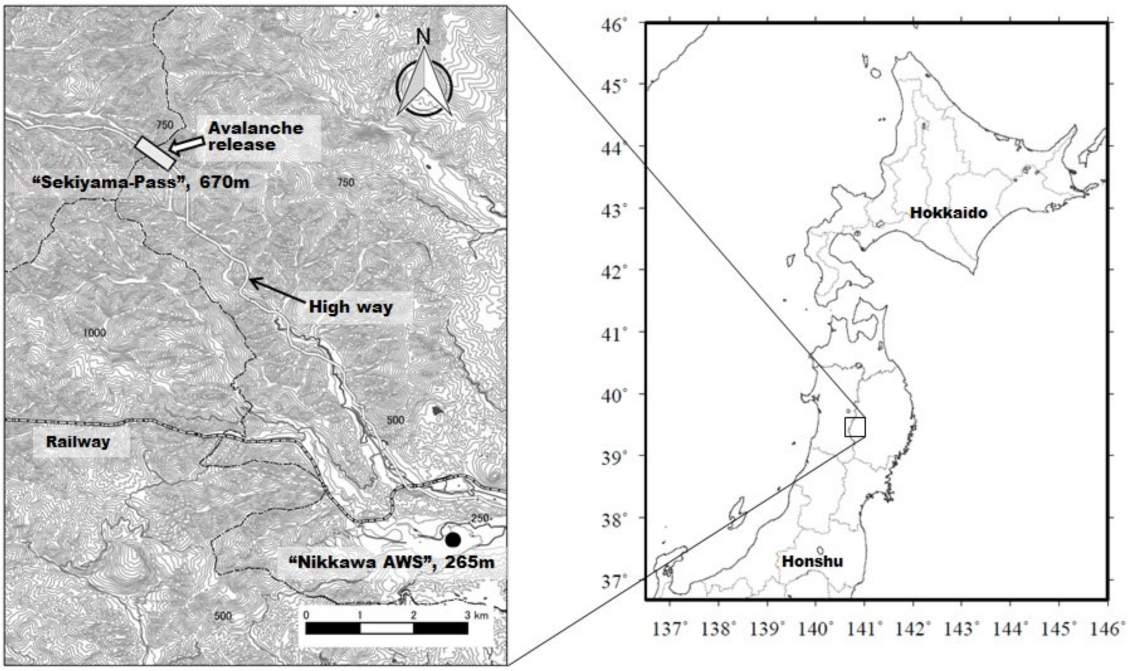

Fig. 2.7. Location of the study sites at Sekiyama Pass in Tohoku, Japan. Terrain is indicated by contour lines at 25 m intervals.

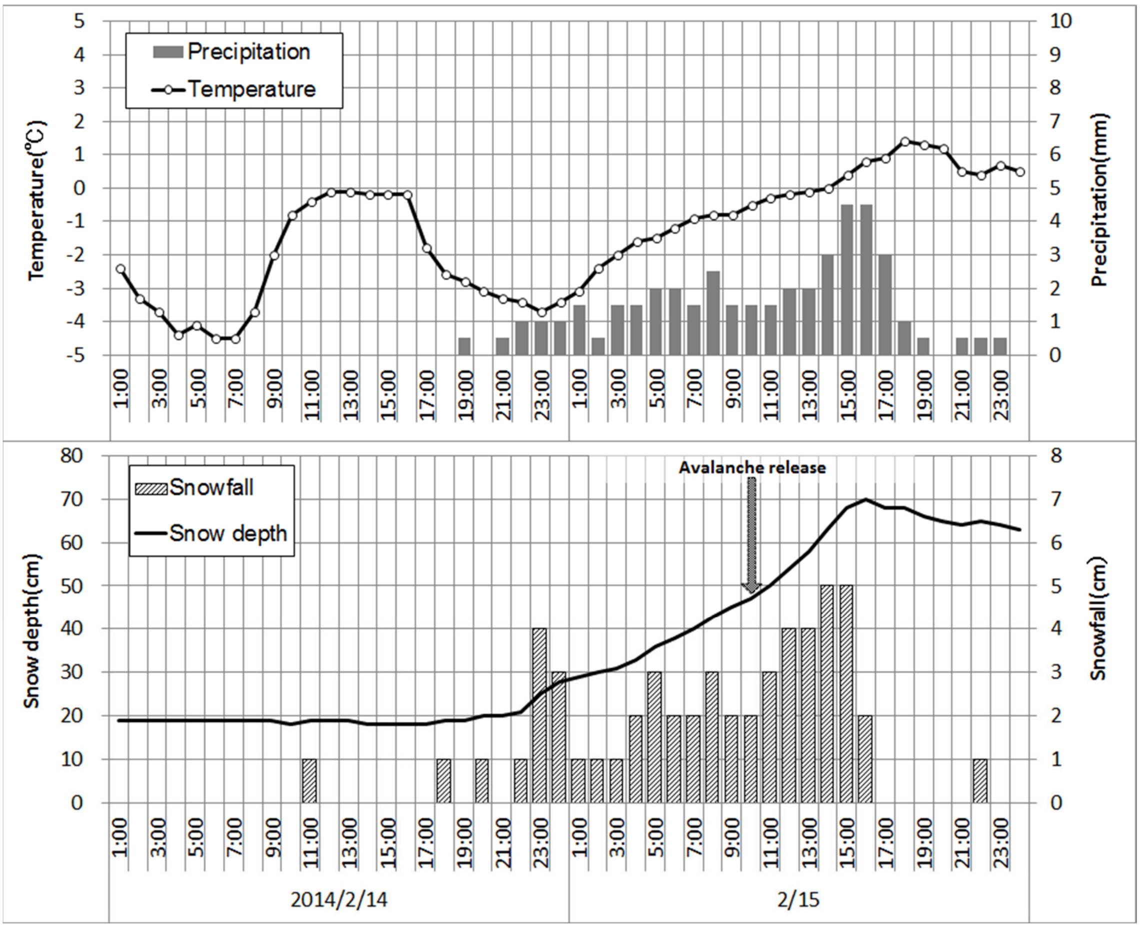

Fig. 2.8. Time series of weather and snow conditions at Nikkawa AMeDAS on February 14 and 15, 2014.

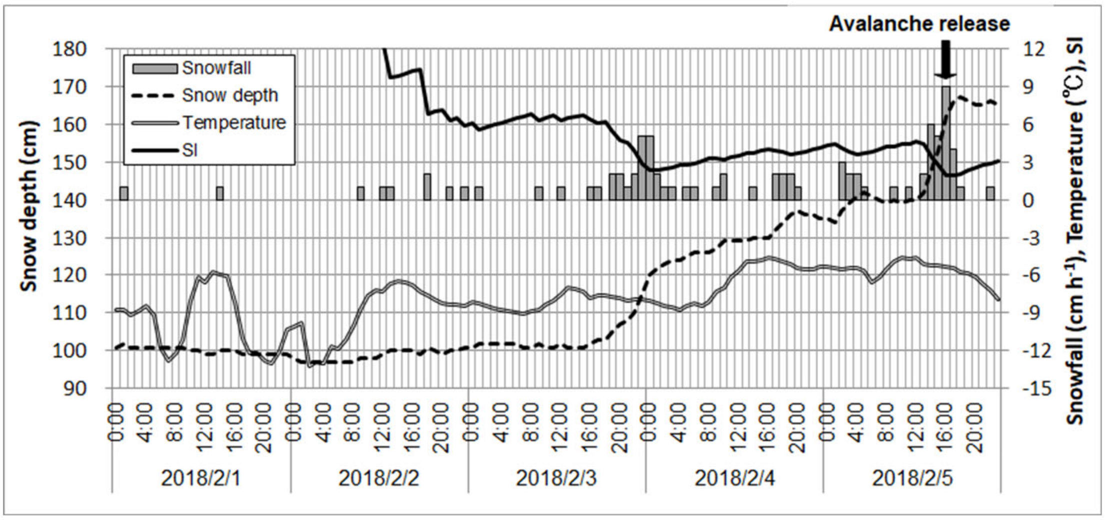

Fig. 2.9. Time series of air temperature, snow depth, snowfall at Notsuka Pass AWS, and SI calculated using the SSCM for February 1–5, 2018.

3. Results

The snow profiles simulated by the SSCM for Mikuni Pass for January 25–29, 2013 are shown in Fig.2.10. Calculations were carried out using the meteorological data shown in Fig. 2.6. Approximately 40 cm of snowfall was recorded at Mikuni AWS during January 25 (Fig.2.6.). However, the maximum amount of accumulated snow measured in the snow pit above the weak layer was about 50 cm on the morning of January 28 (Fig.2.5.). Data from the AWS were used for the simulation, but we note that the snowfall recorded by the AWS (i.e., 40 cm) was 10 cm less than suggested by the observations from the snow pit (i.e., 50 cm). Fig. 2.5. and Fig. 2.10. show that the general trend of simulated snow depth are fairly in good agreement with the observations. The weak layer of FC observed at 50 cm below the surface (Fig. 2.5.) was reproduced well by the SSCM (Fig. 2.10.). However, the snow type is slightly different, as the observations record lightly compacted snow, whereas the SSCM simulated new snow.

Fig. 2.11. shows the SSCM outputs for Mikuni Pass as well as the observed data at 1600 JST 28 January 2013. Overall snow heights often vary over distances of meters even on fairly flat terrain (Lehning et al., 2001). In fact, as is stated above, observed snow height at 10 m away from Mikuni AWS was 0.48 m, while simulated one based on the AWS data was 0.27 m. Thus, we stretched the SSCM profile linearly to compensate for the snow depth differences according to Lehning et al. (2001) and Lundy et al. (2001); modeled and measured snow heights were each assigned a unit height and a normalization of depth is performed. Then, the profile parameters were compared. Further, in Table 2.1, four agreement scores, namely, the mean bias (observed value – model value), root mean square error (RMSE), Pearson's correlation coefficient, and Willmott and Wick's index of agreement (Willmott and Wicks, 1980) were obtained for the snow temperature, density, and shear strength (Lundy et al., 2001). The agreement scores for the grain types were calculated as the simple average over the number of observed layers (Lehning et al., 2001).

Although the simulated temperatures in Fig. 2.11. (a) are around 2 °C lower than the observations, the general trend from the surface to the bottom is similar. Thus, Pearson's correlation coefficient was high as shown in Table 2.1. (a). From the surface to 0.2 of the normalized depth, the difference in the density was within 100 kg m^{-3} (Fig. 2.11. (b)). Although the deviation becomes larger near the bottom, the agreement score for the total snow height was acceptable (Table 2.1. (a)). The shear strength values obtained from both the observations and SSCM in Fig. 2.11. (c) showed good agreement. Particularly the calculated values corresponded well with the values measured using the shear frame. As shown in Table 2.1. (a), all of the scores were reasonably well reproduced. Our pit observations showed DF between 0.4 and 1.0 of the normalized depth range. This layer represents the snow that fell on January 25 and changed to DF over the observation period. However, this layer remained as PP in the SSCM run. Below this layer, FC appeared both in the observations and the SSCM simulation. We calculated normalized distances which are the measure of agreement for the combinations of basic grain types according to Lehning et al. (2001). A score of "1" indicates perfect agreement and "0" stands for no agreement. Score in Table 2.1. (a) was satisfactorily high.

In addition to the example shown in Fig.2.11. and Table 2.1. (a), other ten observations at Mikuni and Kiritachi were compared with the SSCM (see Table 2.1. (b)); comparisons for all measurements with the assigned unit heights are shown in Appendix B. All of the scores for the snow temperature, shear strength, and grain type were reasonably high, as was the case in Table 2.1. (a). In fact, they are similar to, or even better than, the scores obtained using the SNOWPACK model by Lundy et al. (2001) and Hirashima et al. (2004). On the other hand, the score for the density was lower than the others. The SSCM often outputs a lower density than the observations, probably reflecting the lower snow temperature simulation (as shown in Fig. 2.11.). However, the bias in Table 2.1. (b) was not large and did not have a significant effect on the shear strength, which is key for the snow avalanche warnings.

In this study we also completed simulations using the SNOWPACK model developed by Bartelt and Lehning (2002) and Lehning et al. (2002). The SNOWPACK simulation was conducted for all of the snow layers, but Fig. 2.12. shows only the results from above the weak layer (40 cm below the surface) to allow direct comparisons with the SSCM output.

SNOWPACK showed the snow temperature at a depth of 90 cm to be –10 °C, which is almost the same as the observations at this depth. However, the observed gradient in snow temperature from 90 cm depth to the surface (135 cm) was much longer than the SNOWPACK simulation. The observed snow temperature gradient from the surface to the weak layer is larger than that of SNOWPACK. The snow surface temperature generated using SNOWPACK was about 15 °C warmer than the observed temperature. The density simulate by SNOWPACK (Fig. 2.12. (b)) was slightly greater than the observed density, and the density of the granular snow layer was 1.5× greater than the observations. In addition, SNOWPACK showed that the grain type above a depth of 120 cm was new snow. No new snow was recorded in the observations. SNOWPACK showed 25 cm of lightly compacted snow, compared with the 40 cm recorded in the observations. The grain type below 95 cm depth was similar in both the observations and the SNOWPACK simulation. The SNOWPACK shear strength of the lightly compacted snow in Fig. 2.12.(d) agrees reasonably well with the observations (500–800 Pa). However, the value for new snow simulated by SNOWPACK (600 Pa) differed significantly from the observed value of 200 Pa. Each normalized results are shown in Appendix B.

The SSCM calculation for the avalanche released at the Nikkawa AMeDAS for February 14–16, 2014 is shown in Fig. 2.13. The precipitation and air temperature data from the AWS station are applied as inputs to the SSCM. It shows that as the depth of new snow increased rapidly on February 15, the SI decreased rapidly, and when the SI fell below 3.0, the avalanche was released. After 1300 JST on February 15, the grain type in the new snow layer gradually changed to lightly compacted snow, and as the total snow depth decreased the SI value increased accordingly.

On the other hand, the SSCM calculation for the avalanche released at Notsuka Pass around 1600 JST on February 5 is shown in Fig. 2.14. As the depth of PP increased on February 4, the SI decreased rapidly. Then, although it increased gradually, the SI fell again due to the snowfall in the afternoon of February 5. When the SI dropped below 2.5, the avalanche was released; the model was able to accurately simulate the avalanche danger.

We also calculated SI values using the SSCM for 10 other avalanche events listed in Fig. 2.4. The obtained SI values are summarized in Table 2.2. The specific details except for above two incidents are shown in Appendix C. The minimum SI value was 0.9, and the maximum was 4.9, with an average of 2.4 and a standard deviation of 1.1. These are closely comparable with the values in the review by Pelra (1977).

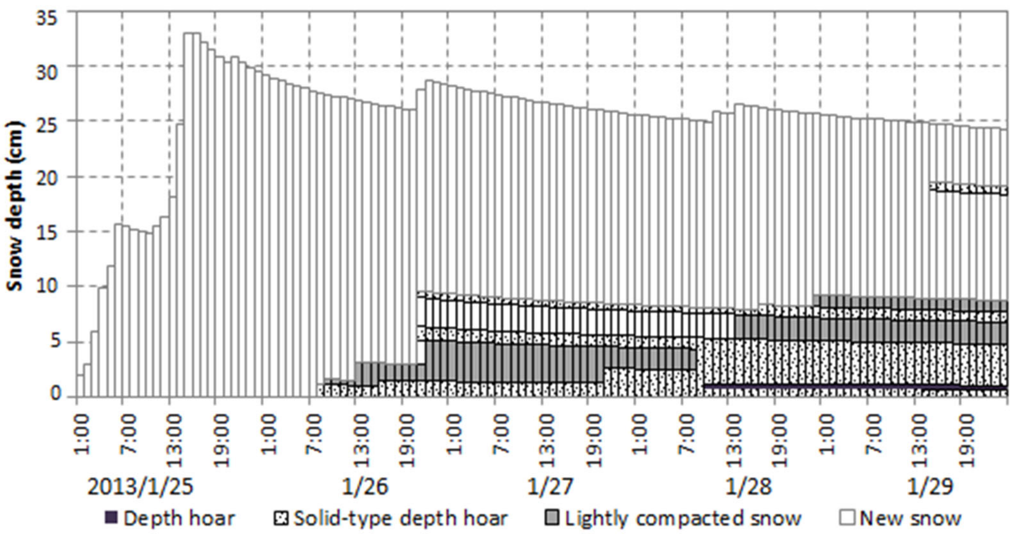

Fig. 2.10. Snow profiles generated by the SSCM for Mikuni Pass for January 25–29, 2013.

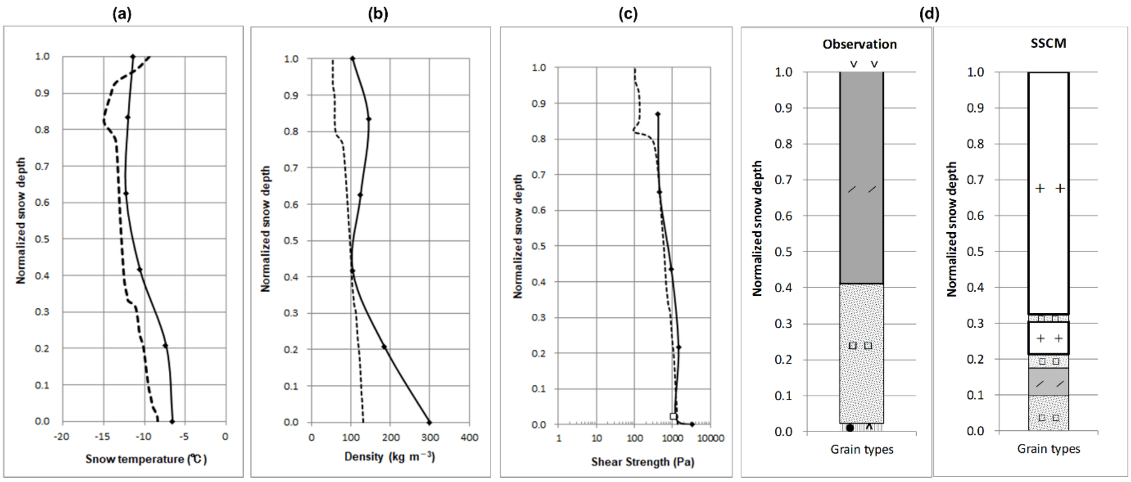

Fig. 2.11. Properties of the snow layer measured (solid line) and calculated by the SSCM (dashed line) using the data from the Mikuni AWS at 1600 JST 28 January 2013. Measured and modeled snow heights (0.48 and 0.27 m, respectively) are each assigned a unit height. Profiles of (a) snow temperature, (b) density, (c) shear strength converted from snow hardness, and (d) grain types are shown. Square in (c) indicates the shear strength (measured using a shear frame) and the symbols in (d) follow the International Classification for Seasonal Snow on the Ground (Fierz et al., 2009). The descriptions of each symbols are shown in Appendix. A.

Table 2.1. Statistical analysis of the simulated and observed snowpack parameters for (a) the Mikuni Pass, Hokkaido at 1600 JST 28th January 2013, and (b) the Mikuni Pass in January 2013 and the Kiritachi Pass in February 2013 and March 2014.

(a) The Mikuni Pass (1600 JST 28th January 2013)

	n	Bias	RMSE	r	d
Snow temperature	6	2.6 °C	3.0 °C	0.9	0.7
Density	6	68.5 kg m^{-3}	85.8 kg m^{-3}	0.7	0.5
Shear strength	6	539.2 Pa	872.7 Pa	0.9	0.7

	n	Score
Grain types	6	0.9

(b) All cases for the Mikuni pass and the Kiritachi pass

	n	Bias	RMSE	r	d
Snow temperature	48	1.6 °C	2.6 °C	0.8	0.8
Density	48	38.2 kg m^{-3}	53.5 kg m^{-3}	0.6	0.6
Shear strength	46	39.4 Pa	507.2 Pa	0.6	0.7

	n	Score
Grain types	50	0.9

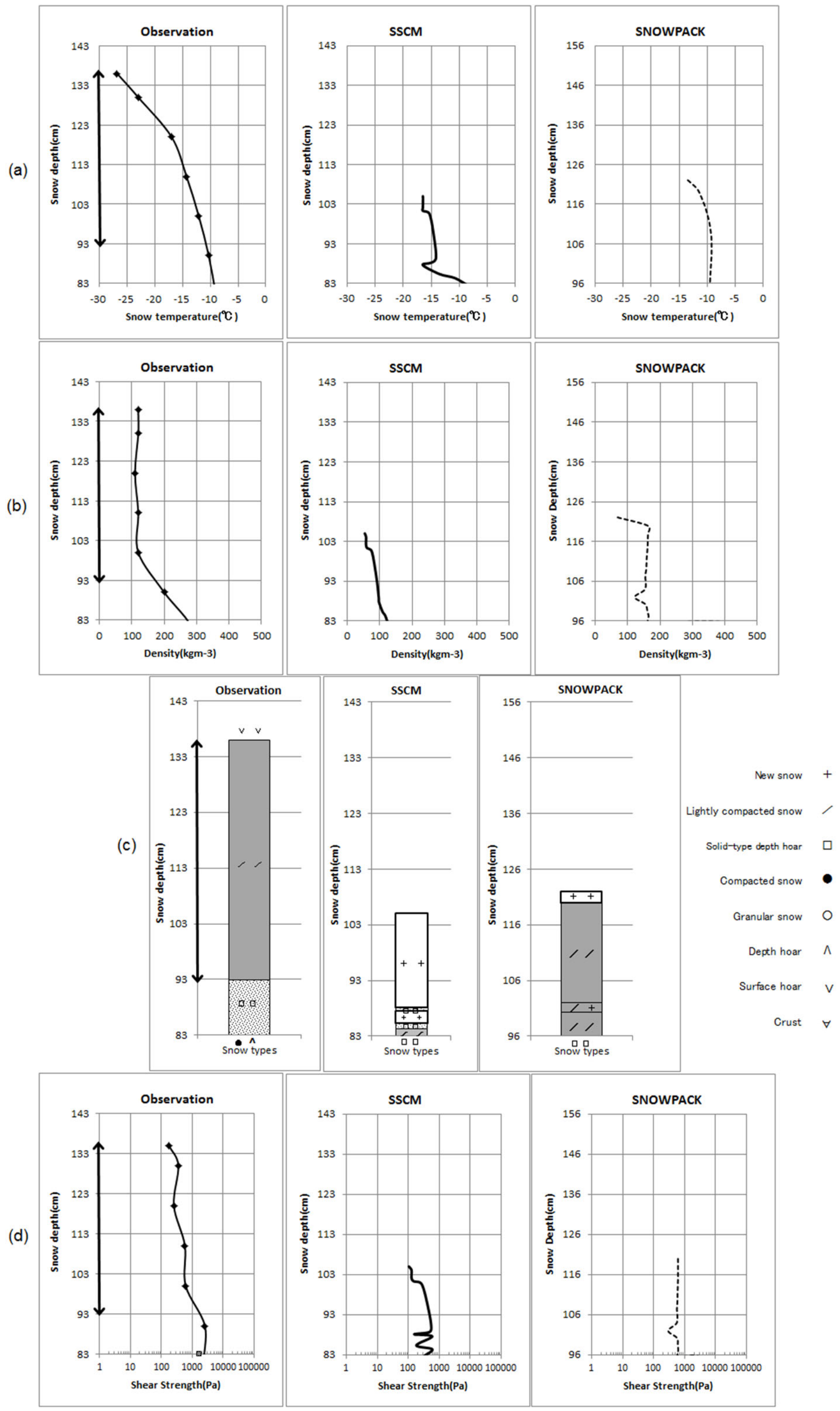

Fig. 2.12. Properties of the snow layer measured calculated using data from the Mikuni AWS at 0800 28 January, 2013 (left) and simulated by the SSCM (center) and SNOWPACK (right). Snow depths simulated by SSCM and SNOWPACK are shown

above the observed weak layer of snow at 93 cm depth and comparisons were made for the overlying layers (arrows). (a) Snow temperature distributions. (b) Density distributions. (c) Snow types distributions. (d) Shear strength distributions. Measured shear strength was converted from snow hardness using the method of Yamanoi et al. (2004). The square symbol at 83 cm depth in the observations indicates the shear strength that was directly measured using the shear flame test.

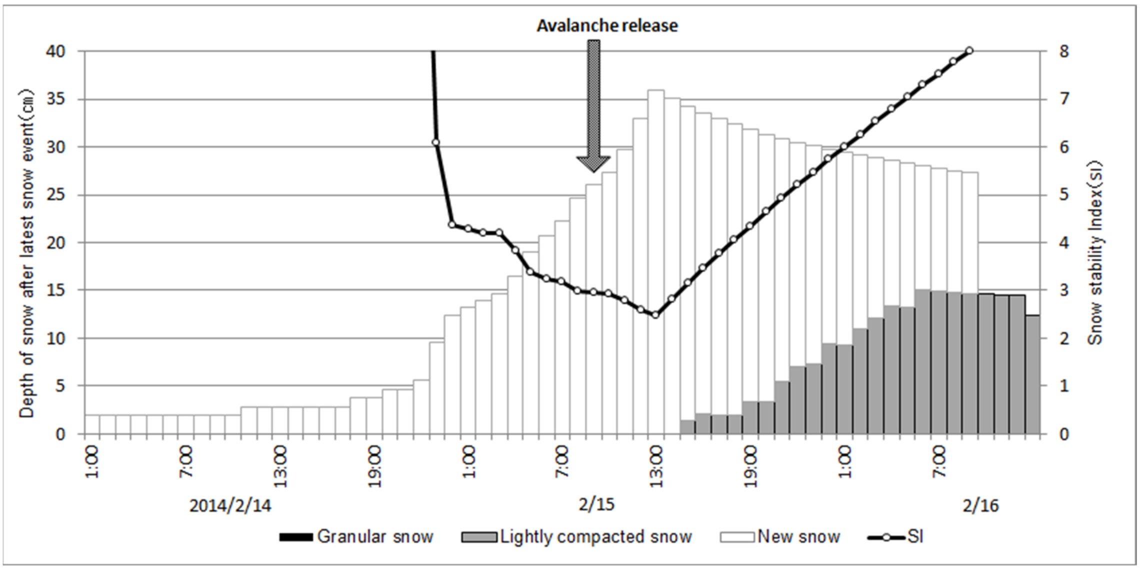

Fig. 2.13. Snow profiles generated by SSCM at the Nikkawa AMeDAS for February 14–16, 2014.

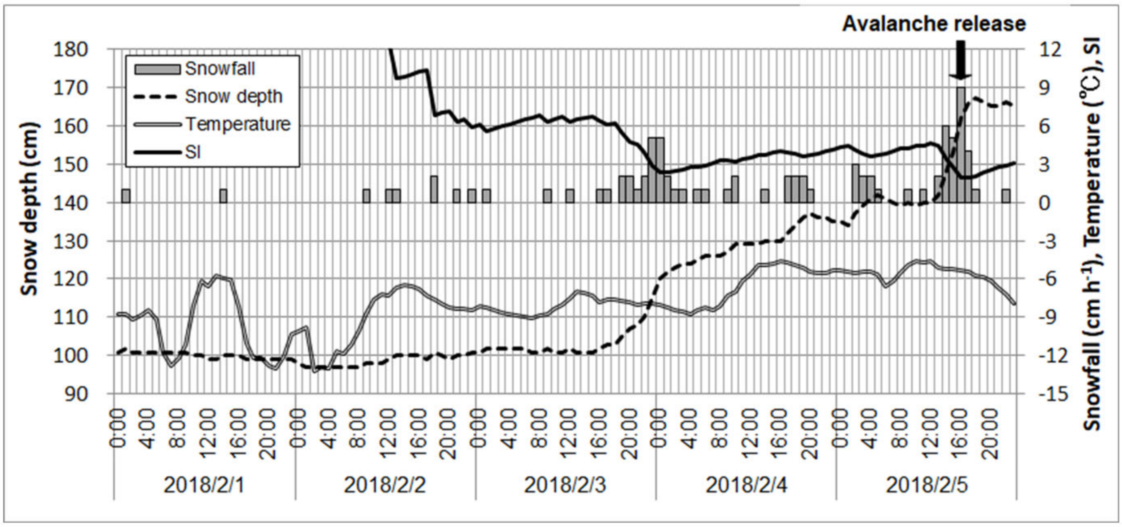

Fig. 2.14. Time series of air temperature, snow depth, snowfall at Notsuka Pass AWS, and SI calculated using the SSCM for February 1–5, 2018.

Table 2.2. Data for the 12 avalanches mentioned in the text. Events 1–9 occurred in Hokkaido; events 10-12 occurred in Honshu. The altitudes of events 8 and 12 correspond to the avalanche release points; for other events altitudes correspond to the elevations where the roads were covered with debris. SI values are obtained from the SSCM simulations.

No.	Location	Release altitude (m)	Debris runout altitude (m)	Release date	SI
1	The Sekihoku Pass		844	1100 JST 14th January 2004	2.5
2	Wakkanai		12	1845 JST 13th February 2008	0.9
3	The Notsuka Pass		423	1700 JST 19th February 2010	3.4
4	Bekkari		55	0330 JST 24th January 2011	2.0
5	The Mikuni Pass		1147	0300 JST 11th December 2012	3.4
6	The Notsuka Pass		522	1600 JST 5th February 2018	1.9
7	The Kiritachi Pass		259	1500 JST 24th January 2020	1.4
8	Pinneshiri	527		1200 JST 1st February 2020	1.3
9	The Notsuka Pass		522	0800 JST 6th March 2020	4.9
10	The Sekiyama Pass		670	0955 JST 15th February 2014	2.9
11	Ooisawa		400	0655 JST 9th February 2014	2.8
12	Okudaisen	758		1200 JST 31th December 2010	1.4

4. Discussion and conclusions

We developed an SSCM in this study that can reproduce, within reasonable accuracy, the changes in snowpack properties that follow a large snowfall, and is therefore suitable for use as an avalanche warning tool. However, room for improvement remains.

Firstly, as shown in Fig. 2.11. (a), although the overall trend of the snow temperature calculated by the SSCM agreed well with the observations and the correlation coefficients were high, the simulated temperatures were generally lower than the observations.

Consequently, the model tends to simulate a lower snow density because, as shown in Eq. (2.3), snow viscosity is a function of snow temperature. In fact, the values of bias in Table 2.1 are larger than those reported by Lundy et al. (2001) and Hirashima et al. (2008). As described before, we calculated the snow temperature simply following Eq. (2.1) without applying the heat transfer equation, and it might cause the differences. However, the SNOWPACK model, which incorporates the above process as well as the heat balance on the snow surface, also occasionally simulated systematic differences from the surface to the base (Lundy et al., 2001). In particular, large deviations were recognized near the surface. Thus, this issue is left for future consideration.

Secondly, as shown in Fig. 2.11. (d), the snowfall on 25th January changed to DF in the observations but remained as PP in the SSCM run. This suggests that the viscous compression process as well as the snow temperature calculation should be improved.

When we applied the SSCM to the avalanche incidents in Table 2.2, the calculated SI values were similar to those reported by Pelra (1977). It suggests the suitability of the SSCM for use as an avalanche warning system, although the model has not been combined with meteorological forecasts at this stage. The system should also consider the effect of wind over complex topography. Wind causes snowdrift and non-uniform snow can accumulate, which sometimes increases the avalanche risk. In fact, in Table 2.2, the

SI for avalanche case 6 at Notsuka Pass is apparently larger than the values suggested by Sommerfeld (1984) and Hirashima et al. (2006, 2008). In our calculation, we input the meteorological data from the Notsuka AWS station, which is located on the lee side of the mountain, but the wind speed was probably much higher near the avalanche release area and this is likely to have caused greater snow accumulation. The effect of snow drifts should thus be incorporated into the model to make it more precise.

Additionally, comparing the SSCM and SNOWPACK outputs, we identified the following differences. The SSCM offers a useful approach to the prediction of surface avalanche that may develop within a few days of a heavy fall of snow and so could help to prevent future avalanche-related disasters. On the other hand, the SSCM is not skillful with respect to seasonal simulations, and this is because the physical processes related to snow melting encoded in the SSCM are simpler than those used in SNOWPACK.

III. Calculation of snowdrift distribution over complex topography to improve the accuracy of snow avalanche warning systems

1. Introduction

Snow avalanches causes the substantial damages on not only the road and the railway transportations but in the various aspects of the human activities in the snowy region. Komatsu and Nishimura (2020) developed a simple snow-cover model (SSCM) that only requires the air temperature and precipitation or snow depth as input data to evaluate snow avalanche hazards. The SSCM can reproduce, within reasonable accuracy, changes in snowpack properties and snow avalanche incidents after a large snowfall. However, it has been revealed that the effect of wind over complex topography should be additionally considered. Wind speed is generally high near an avalanche source area, such that greater snow transport and accumulation occur on the leeward slope. Snow drifting should therefore be incorporated into the SSCM to improve the accuracy of the model results.

Lehning et al. (2008) developed the Alpine3D numerical model, which incorporates high-resolution wind fields that are calculated using the ARPS meso-scale atmospheric model (Xue et al. 1995), to evaluate the snow distribution across steep alpine terrain. Vionnet et al. (2017) also simulated snow accumulation in alpine terrain using the Meso-NH/Crocus fully coupled snowpack/atmosphere model. The former is a non-hydrostatic atmospheric model (Lafore et al. 1998), and the latter is a detailed snowpack model (Brun et al. 1992). However, Japanese avalanche warning systems rarely consider heterogeneous snow distributions in mountainous regions when assessing potential snow avalanche hazards.

Here we developed a system to calculate snow transport and deposition across complex topography and coupled this system to the SSCM. We then applied this coupled model to the Niseko ski area in Hokkaido, Japan (Fig. 3.1), to assess potential snow avalanche hazards. Although the altitude of Mt. Annupuri is only about 1,300 m above sea level (a.s.l.), the snow is completely dry in winter and very popular among skiers. Therefore, the local communities and ski area managers strongly desire a more precise avalanche warning system. Furthermore, the local government and National Research Institute for Earth Science and Disaster Resilience (NIED) have established six propeller anemometers across the target area (Fig. 3.1), which can be used to verify the performance of this procedure. Five of them are set at 3 m high and one at Hanazono is 10 m, and all the data are recorded every 10 minutes. We also attempted to simplify the procedures as much as possible, comparing to the sophisticated models like Alpine 3D, to reduce the computational requirements of the model and generate numerous simulations within a short period, which is ideal for modeling a snow avalanche scenario within one hour.

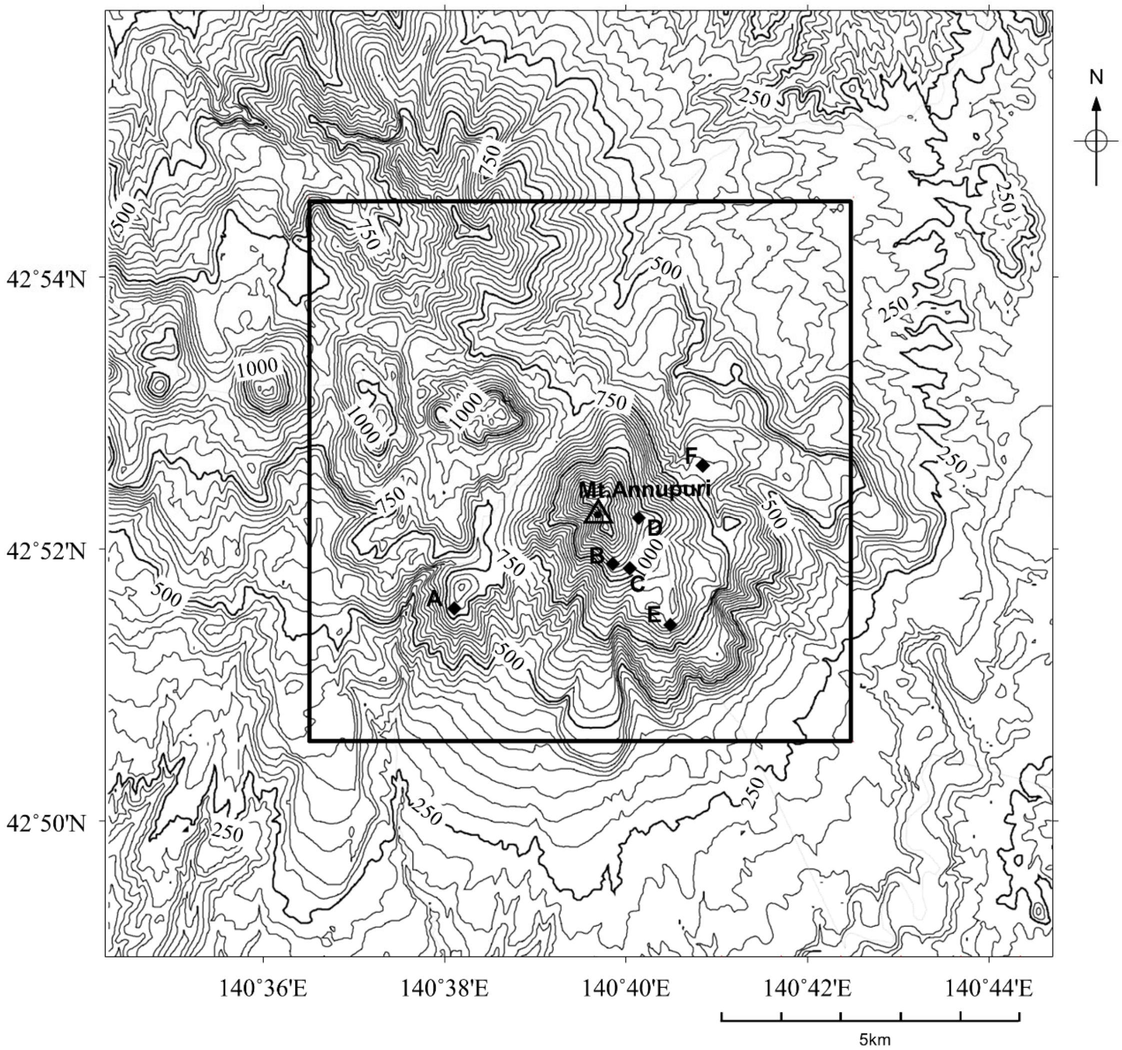

Fig. 3.1. Topographic map of the model domain across the Niseko region. Detailed analyses are conducted within the area that is enclosed by the black square. The locations of the wind observation stations are also shown: Moiwa (A), Annupuri (B), Yunosawa (C), Hirafu (D), Village (E), and Hanazono (F).

2. Methodology

2.1 Model

Wind-induced snow transport can be divided into two general transport modes: saltation and suspension (Bagnold 1941). Here we apply continuum mixture theory to this turbulent mixture of air and snow particles. The particle concentrations in the suspension layer are calculated using the conservation equation for the snow–air mixture, and the wind field is calculated using the Reynolds-averaged Navier–Stokes equation. The effect of the saltation layer is included as the lower boundary condition of the diffusion equation. Our model consists of air flow and blowing snow simulations that are based on Uematsu et al. (1991) and Sato and Yasuda (2014). We first simulate the wind field over the terrain to obtain the friction velocity distributions and calculate the snowdrift transport. We then obtain erosion and/or deposition rates via the divergence of the snow transport rate. Generalized curvilinear coordinates along the surface topography are used during the calculations (Murakami et al. 1989).

2.1.1 Air flow simulation

Air flow was simulated based on the conservation of mass and momentum as follows:

$$\frac{\partial u_i}{\partial x_i} = 0 \qquad (3.1)$$

and

$$\frac{\partial u_i}{\partial t} + \frac{\partial u_i u_j}{\partial x_j} = -\frac{1}{\rho}\frac{\partial p}{\partial x_i} + \frac{\partial}{\partial x_j}\left\{ \upsilon_t \left[\frac{\partial u_i}{\partial x_j} + \frac{\partial u_j}{\partial x_i} \right] \right\}, \quad (3.2)$$

where x_i is the spatial coordinate system (x, y, z), u_i is the average wind speed vector (u, v, w; m s^{-1}), t is time (s), p is air pressure (kg m^{-1} s^{-2}), ρ is air density (1.29 kg m^{-3}), and υ_t (m^2 s^{-1}) is the coefficient of eddy viscosity. The standard k–ε model under the neutral condition was applied for υ_t as follows:

$$\upsilon_t = C_\mu \frac{k^2}{\varepsilon}, \quad (3.3)$$

$$\frac{\partial k}{\partial t} + \frac{\partial k\, u_j}{\partial x_j} = \frac{\partial}{\partial x_j}\left[\frac{\upsilon_t}{\sigma_k}\frac{\partial k}{\partial x_j} \right] + \upsilon_t \left[\frac{\partial u_i}{\partial x_j} + \frac{\partial u_j}{\partial x_i} \right] \frac{\partial u_i}{\partial x_j} - \varepsilon, \quad (3.4)$$

$$\frac{\partial \varepsilon}{\partial t} + \frac{\partial \varepsilon\, u_j}{\partial x_j} = \frac{\partial}{\partial x_j}\left[\frac{\upsilon_t}{\sigma_\varepsilon}\frac{\partial \varepsilon}{\partial x_j} \right] + C_{1\varepsilon}\frac{\varepsilon}{k}\upsilon_t \left[\frac{\partial u_i}{\partial x_j} + \frac{\partial u_j}{\partial x_i} \right] \frac{\partial u_i}{\partial x_j} - C_{2\varepsilon}\frac{\varepsilon^2}{k}, \quad (3.5)$$

where k is turbulent energy (m^2 s^{-2}), ε is the dissipation rate of turbulent energy (m^2 s^{-2}), and C_μ, $C_{1\varepsilon}$, $C_{2\varepsilon}$, σ_k, and σ_ε are constants. Here we used $C_\mu = 0.09$, $C_{1\varepsilon} = 1.44$, $C_{2\varepsilon} = 1.92$, $\sigma_k = 1.0$, and $\sigma_\varepsilon = 1.3$ from Launder and Spalding (1974).

At the inlet boundary condition, logarithmic vertical wind profiles were assumed in the model and the boundary conditions were set as

$$u = v = w = 0 \quad (3.6)$$

at the bottom and

$$u = u_{ini}, v = v_{ini}, w = 0 \qquad (3.7)$$

at the top of the domain. Furthermore, the radiation condition of Orlanski (1976) is adopted at the lateral boundaries.

The friction velocity at the snow surface was obtained as

$$u_* = \frac{u(z)\,\kappa}{\ln\left(\frac{z}{z_0}\right)}, \qquad (3.8)$$

where $u(z)$ is wind speed (m s^{-1}) at level z (m), κ is the von $Kármán$ constant (0.4), and z_0 is surface roughness (10^{-4} m, Kikuchi 1981). z_0 was used to define the logarithmic profile of wind velocity at the inflow boundary.

2.1.2 Snow transport simulation

The vertically integrated snowdrift flux q (kg m^{-1} s^{-1}) in the saltation layer is expressed as

$$q = \int_0^h (u_s\, \Phi)\; dz, \quad (3.9)$$

where u_s is the mean horizontal particle velocity (m s^{-1}), Φ is the snowdrift density (kg m^{-3}), and h is the thickness of the saltation layer (m). We employ the expression for q as proposed by Iversen et al. (1980):

$$q = C\left(\frac{\rho}{g}\right)\frac{|w_f|}{u_{*t}}\, {u_*}^2 (u_* - u_{*t}), \qquad (3.10)$$

where g is the acceleration of gravity, w_f is the snow-particle fall speed, u_{*t} is the threshold friction velocity, and C is a constant. Following Uematsu et al. (1991), w_f, C, and u_{*t} were set to 0.5 m s^{-1}, 1.0 and 0.2 m s^{-1} respectively for the simulations in this study.

The suspension is calculated using the following diffusion equation:

$$\frac{\partial \Phi}{\partial t} + \frac{\partial(\Phi\, u_i)}{\partial x_i} = \frac{\partial}{\partial x_i}\left(\upsilon_s \frac{\partial \Phi}{\partial x_i}\right) - \frac{\partial(w_f\, \Phi)}{\partial x_3}, \qquad (3.11)$$

where Φ is snowdrift density (kg m^{-3}) in the suspension layer and υ_s is the eddy diffusion coefficient of snow. υ_s is assumed to be equal the momentum diffusivity of υ_t in this study.

The snowdrift density at the upper boundary is expressed as

$$\Phi_H = \frac{P_{re}}{|W_f|}, \qquad (3.12)$$

where P_{re} is the snowfall rate (kg m^{-2} s^{-1}). The upper boundary of suspension is the height where snowdrift density becomes zero.

The lower boundary of the suspension layer is in contact with the saltation layer. Therefore, the mean snowdrift density of the saltation layer Φ_h, which can be obtained by dividing q with u_s (= u_h) and h, is considered the lower boundary condition of the suspension layer. We note that the thickness of the saltation layer may change with the development of wind-driven snow transport; however, in this study, we assumed a constant thickness of 0.25 m which corresponds to the height of the first layer above the ground.

2.1.3 Deposition or erosion rates

The snowdrift rate S (kg m^{-2} s^{-1}) is defined as the mass of snow that accumulates on a unit horizontal area per unit time, and is calculated as the sum of the deposition rate D and erosion rate E:

$$S = D - E. \qquad (3.13)$$

D and E are expressed as follows:

$$D = |w_f|\Phi_h \qquad (3.14)$$

and

$$E = \frac{q|w_f|}{u_h\, h}, \qquad (3.15)$$

respectively.

The snow depth change within a unit time H (m) is then obtained by dividing S by the new snow density (10^2 kg m^{-3}).

2.1.4 Set up of numerical simulation

A numerical simulation method of SIMPLER developed by Patankar (1981) is applied to obtain a three-dimensional wind field. The wind field over the Niseko region is calculated using a digital elevation map with a 50-m grid interval that was supplied by the Geospatial Information Authority of Japan (GSI). The model spans 14 × 14 × 3.5 km in the $X \times Y \times Z$ domain. A stretched grid of 25 layers, in which 11 layers exist in the lowest 10 m, was applied for the vertical one. We focused on the 10 × 10 km area indicated by the black square in Fig. 3.1, which covers all of the ski fields and wind measurement locations, for the analysis presented in the following section.

2.2 Wind observations in the target area

As is described before, the local government of Niseko and National Research Institute for Earth Science and Disaster Resilience (NIED) have installed six anemometers across the target area (Figure 3.1) and the data are utilized for the model verifications. The detailed locations and altitudes are listed in Table 1.1 and anemometers set at Anuupuri ((B) in Fig. 3.1) and Hanazono ((F) in Fig. 3.1) are shown in Fig. 3.2 and 3.3.

Table 1.1. Locations of anemometers set in the Niseko area.

	Moiwa	**Annupri**	**Yunosawa**	**Hirafu**	**Village**	**Hanazono**
Latitude(°N)	42°51′33.64″	42°52′01.62″	42°52′00.21″	42°52′22.49″	42°51′35.18″	140°40′37.55″
Longitude（°E)	140°38′06.30″	140°39′38.25″	140°39′49.28″	140°39′55.30″	140°40′16.08″	42°52′45.70″
Elevation (m)	682	1,087	1,035	1,065	917	707

Fig. 3.2. Anemometer installed at Annupuri ((B) in Fig. 3.1).

Fig. 3.3. Anemometer installed at Hanazono ((F) in Fig. 3.1).

2.3 Wind tunnel experiment

Wind tunnel experiments are also carried out for the model verifications.

In order to investigate the air flow around the structures applying the wind tunnel experiment, strictly speaking, we need to take into account the similarity law: that is "Reynolds number *Re* " needs to be adjusted.

$$R_e = \frac{U\,L}{\upsilon} \qquad (3.16)$$

where $U\ (m\ s^{-1})$ is the representative value of wind speed, $L\ (m)$ is that of length, $\upsilon\ (m^2\ s)$ is the kinematic viscosity. However, occasionally it is inevitable to set *U* as extremely large because the scale *L* of the model is generally much smaller than the real one. Thus, in this study, we applied the well-known following idea. That is "the flow around the structures become insensitive to *Re* over the critical value of $Re = 10^5$ " .

On the other hand, in order to validate the output of the snow accumulation (erosion and deposition), we carried out the wind tunnel experiments using the activated cray. Overviews of wind tunnel observation with the activated cray are introduced in Oikawa et al. (2007) and Tsutsumi (2009).

Tsutsumi (2009) mentioned that the physical properties of activated cray are close to the natural snow. Particularly, the threshold friction velocity when the drifting starts and the angle of repose, are almost the same as shown in Table 3.2. Oikawa et al. (2007) also discussed the similarly among the wind tunnel observations using the activated clay and the walnuts, and the snow field observation as shown in Table 3.3. Both two important parameters of the threshold friction velocity ratio (moving critical velocity ratio in Table 3.3) and the angle of repose are the almost same for the snow and the activated clay. Former determines the initiation of the particle movements, and the latter regulates the total shape of the snow drift. Since Stokes parameter for all particles are less than one, they can follow the flow around the structures. Although the terminal velocity ratio of snow and clay are different, it is not always necessarily to match. By the large turbulence generated by the complicated topographies, particles were easy to transit from the saltation to the suspension at a relatively low wind speed. Then, the saltation motion is not the principal mechanism of the particle transport process any more. Thus, requirement of the Froude number and the terminal sedimentation velocity ratio, in fact activated clay of which is much larger than the snow in Table 3.3, can be relaxed from the similarity parameter. Based on above arguments, we tried the wind tunnel experiments with the activated clay in order to verify the model output of the snow accumulation.

Table 3.2. Characteristic of activated clay (Tsutsumi (2009).

	Natural snow	**Activated cray**
Mean particle size (mm)	0.2～2	0.02
Density (g cm^{-3})	0.03～0.2	0.47
Critical friction velocity u_f^* (m s^{-1})	0.15～0.40	0.16～0.20
Angle of repose (°)	45～50	46

Table 3.3. Characteristic of activated clay, walnuts and snow (Oikawa et al. (2007)).

Parameter		Wind tunnel		Field observation
		Activated cray	Walnut	
Moving critical friction velocity ratio	u_{*t}/U	0.04	0.037	0.037
Angle of repose	Φ	46	36	45～50
Froude number	$\rho_a U^2/\rho_p gL$	61.7	20.3	1.1～11.4
Stokes parameter	S_t	<1	<1	<1
Terminal sedimentation velocity ratio	$\|w_t\|/U$	6.6×10^3	0.029	0.2～0.3

In this study we carried out the experiments with the wind tunnels at Shinjo Cryospheric Environment Laboratory, Snow and Ice Research Center, NIED (tunnel A) and at Northern Regional Building Research Institute, the Hokkaido Research Organization (NRB-HRO) (tunnel B).

The working section of the wind tunnel A, which is used to obtain the wind speed distribution over the Niseko area, is a closed-circuit wind tunnel situated in a large cold laboratory and has a working section of 14 m long, 1 m wide and 1 m high. Schematic view and the picture of the tunnel A are shown in Figs. 3.4. and 3.5. Although the experiments can be carried out at the maximum wind speed of 20 ms^{-1} and the lowest temperature of –30 ˚C, in this study, all the measurements were conducted at 3 ms^{-1} and under the ordinary temperature. The wind speed distribution was measured with a hot wire anemometer at 1 mm high and 5 cm interval over the terrain model (shown later).

On the other hand, we used the wind tunnel B to examine how snow drift develops in the Niseko area. It is also the closed-circuit type and size of the test section is 0.7 m high, 1.5 m wide and 9.5 m long. Schematic figure of the tunnel and the pictures of the facilities are shown in Figs. 3.6. and 3.7. Activated clay was used instead of snow. As is described before, the similarity rule for snow and activated clay has not been established, strictly speaking. However, such clay is known to be useful material to reproduce snowdrift formation around buildings, roads, and snow fences in a wind tunnel. Clays, stored in the tank of feeder equipment, were pressured with the compressor and provided in the wind tunnel from the nozzle with the constant rate. In this study, 10 kg of the clay was supplied under the wind speed of 3 m s^{-1} for the duration of 40 minutes. The thickness of accumulated cray was measured with the laser displacement meter every 3 mm interval with an error of ± 0.1 mm. Experiments with the activated clay and the terrain model of Niseko are introduced in Fig. 3.8.

Terrain model of the Niseko area is shown in Fig. 3.9. It is 90 cm × 90 cm and on a scale of 1:10,000. The model was set in the wind tunnels A and B, and the wind distributions and the accumulation of the activated clay were measured respectively.

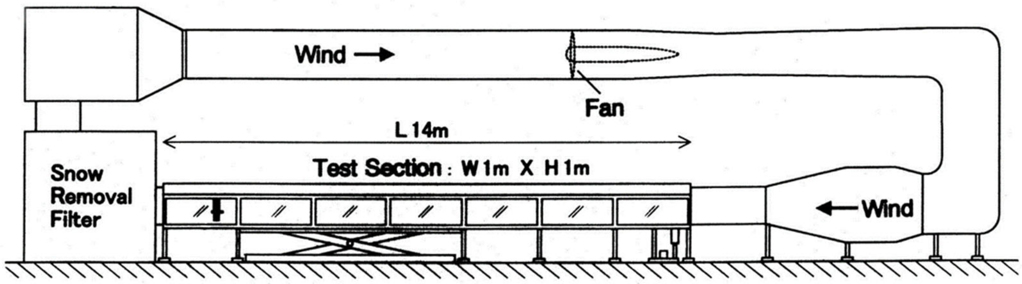

Fig. 3.4. Schematic view of the wind tunnel A at Shinjo Cryospheric Environment Laboratory, Snow and Ice Research Center, NIED (courtesy by Dr. M. Nemoto at NIED).

Fig. 3.5. Wind tunnel A at Shinjo Cryospheric Environment Laboratory, Snow and Ice Research Center, NIED (courtesy by Dr. M. Nemoto at NIED).

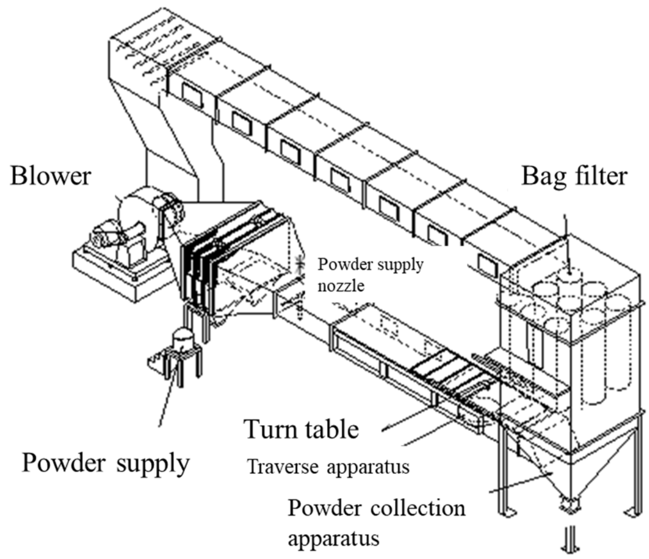

Fig. 3.6. Schematic view of the wind tunnel B at Northern Regional Building Research Institute, the Hokkaido Research Organization (NRB-HRO).

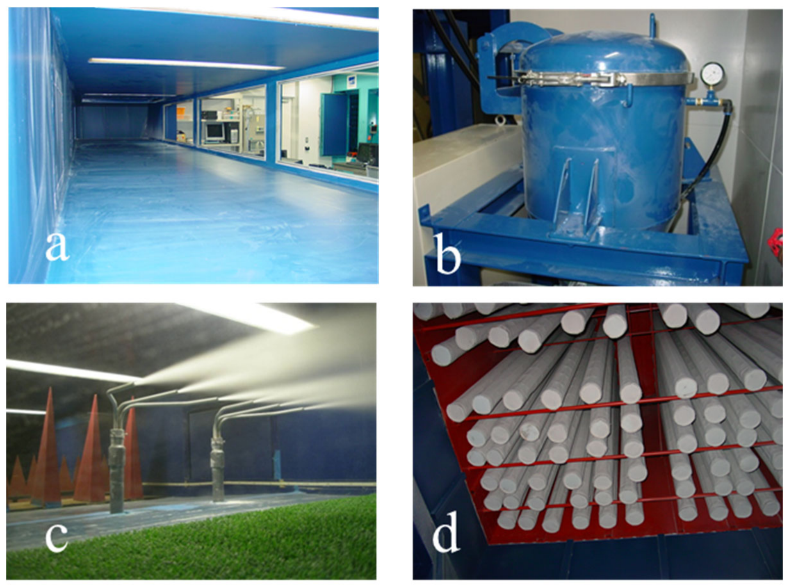

Fig. 3.7. Wind tunnel facilities at Northern Regional Building Research Institute, the Hokkaido Research Organization (NRB-HRO). a: inside of the tunnel, b: powder container, c: powder supply nozzle, d: bag filter.

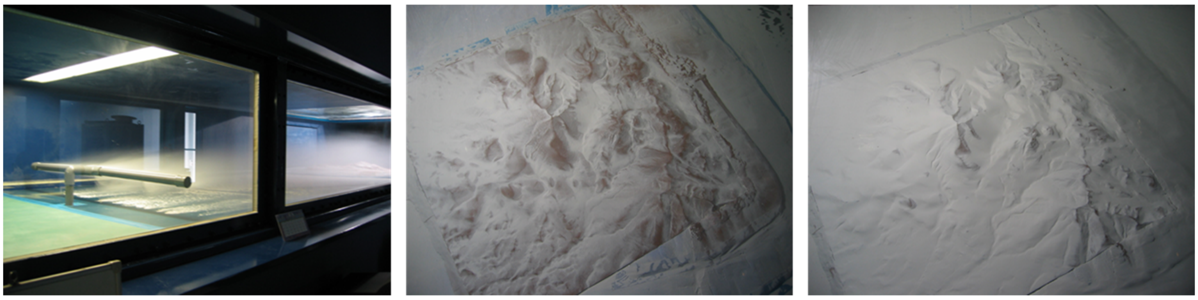

Fig. 3.8. Wind tunnel experiments at wind tunnel B.

left: powder spray from the nozzle, center: initial stage,

right: final stage of the experiment

Fig. 3.9. Terrain model of Niseko with scale of 1:10,000 for the wind tunnel experiments,

2.4. Mobile observation vehicle

Mobile observations by the vehicle, which equipped the meteorological observation gears, are also carried out to examine the model outputs. As is shown in Fig.3.10., the location by the GPS, air and road temperatures, wind speed and direction, visibility along the road are measured and all the data are stored every 0.1 second. Further, the view from the front window was also recorded by the digital video camera.

Observations were conducted at two sites in Hokkaido: not only Niseko in October 2016 and February 2017 but also Wakkanai in December 2009. Observation roots at each sites are shown in Figs, 3.11 and 3.12.

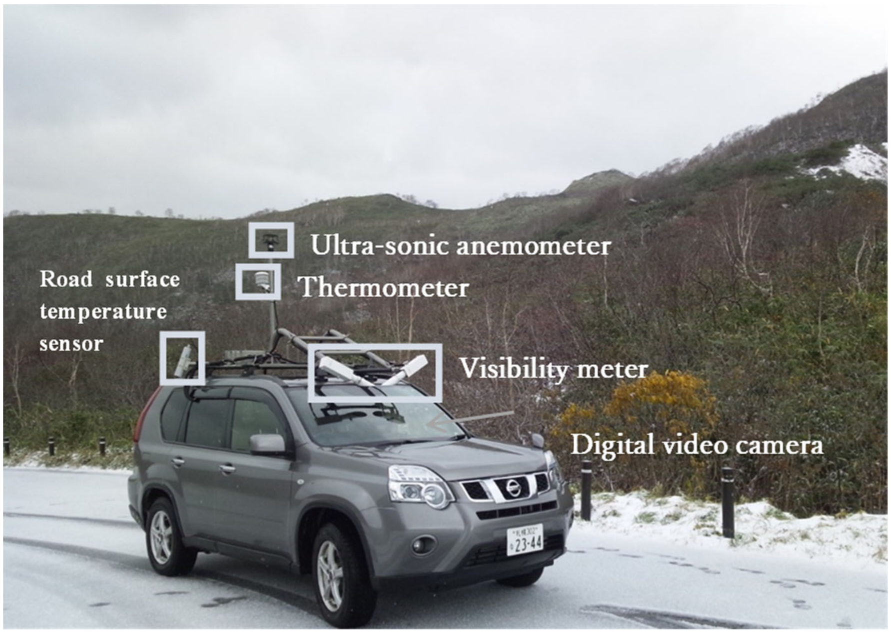

Fig. 3.10. The mobile observation vehicle.

Fig. 3.11. Mobile observation root at Niseko and several views from the front window on the way in October 2016.

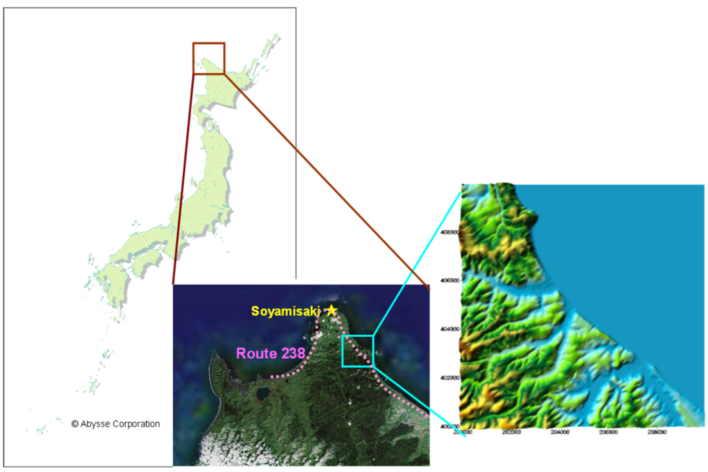

Fig. 3.12. Mobile observation root at Wakkanai in December 2009 shown by the dotted pink line and right figure shows the domain calculated the avalanche danger

level.

3. Numerical simulation results

3.1 Wind distribution

3.1.1. Comparison with the field observations

We first calculated the wind speed distributions when winds of 10 m s^{-1} at 10 m above the surface blew into the domain from the corresponding boundary, and binned each wind calculation into the appropriate 16 wind directions of the compass rose; all of the data were then stored as look-up tables. Fig.3.13 shows the cases for the WNW and SW wind directions, where higher wind speeds are observed across the windward area of the high-altitude region, and lower wind speeds on the leeward side of the mountain and in the valley. Further, Fig. 3.14 and Fig. 3.15 show the cases of the wind speed distributions when winds of 5 m s^{-1}, 10 m s^{-1}, and 15 m s^{-1} blew into the domain from W and WNW. Although the magnitude of the wind speeds differs according to the wind speed blowing into the domain, general trend, such as, at the windward area of the high-altitude region wind speed is high while at the leeward side of the mountain and in the valley it is low, does not vary significantly.

We then set the Kucchan AMeDAS (KA) automatic weather station, which is operated by the Japan Meteorological Agency and located 8.5 km ENE of the summit of Mt. Annupuri, as the reference point in this study. Although KA is outside of the calculation domain, we confirmed that the wind speeds and directions at KA are approximately the same as those at the easternmost grid point at the same latitude in Fig. 3.1, and set that point as the virtual KA reference point; we note that these two points are only separated by flatlands. Furthermore, the wind directions and speeds at the reference point are almost the same as the boundary conditions for all of the 16 wind directions, with most of the wind speed differences being less than 0.5 m/s. We subsequently obtained the ratios between the wind speed data at KA and all of the data in the domain for the 16 wind directions. Furthermore, based on the Figs. 3.14 and Fig.3.15, we assume that the ratio does not vary significantly for different wind speeds. Then we can reasonably calculate the wind speed distribution in the domain by multiplying the wind speed at KA by the ratio map obtained for each wind direction. We confirmed that the wind directions and speeds at the reference point were almost the same as the boundary conditions for all cases. The time series of hourly wind speed at the six observation points in Fig. 3.1. was calculated for one month (February 2020). The time series for three cases at Moiwa, Village and Annupuri are shown in Fig. 3.16 and the scatter plot of observed and calculated wind speeds for all sites are shown in Fig. 3.17. Three agreement scores [i.e., mean bias (observed value – model value), root mean square error (RMSE), and correlation coefficient between the observed and simulated wind speeds at the six sites] are listed in Table 3.4. The model worked reasonably well, as the correlation coefficients for all of the sites are ~0.8, the biases are within $\pm 1.5 \text{ m s}^{-1}$, and the RMSEs are $2.5 - 3.3 \text{ m s}^{-1}$. We also note that the periods of strong wind during 17–18 and 22–24 February are well reproduced by the model.

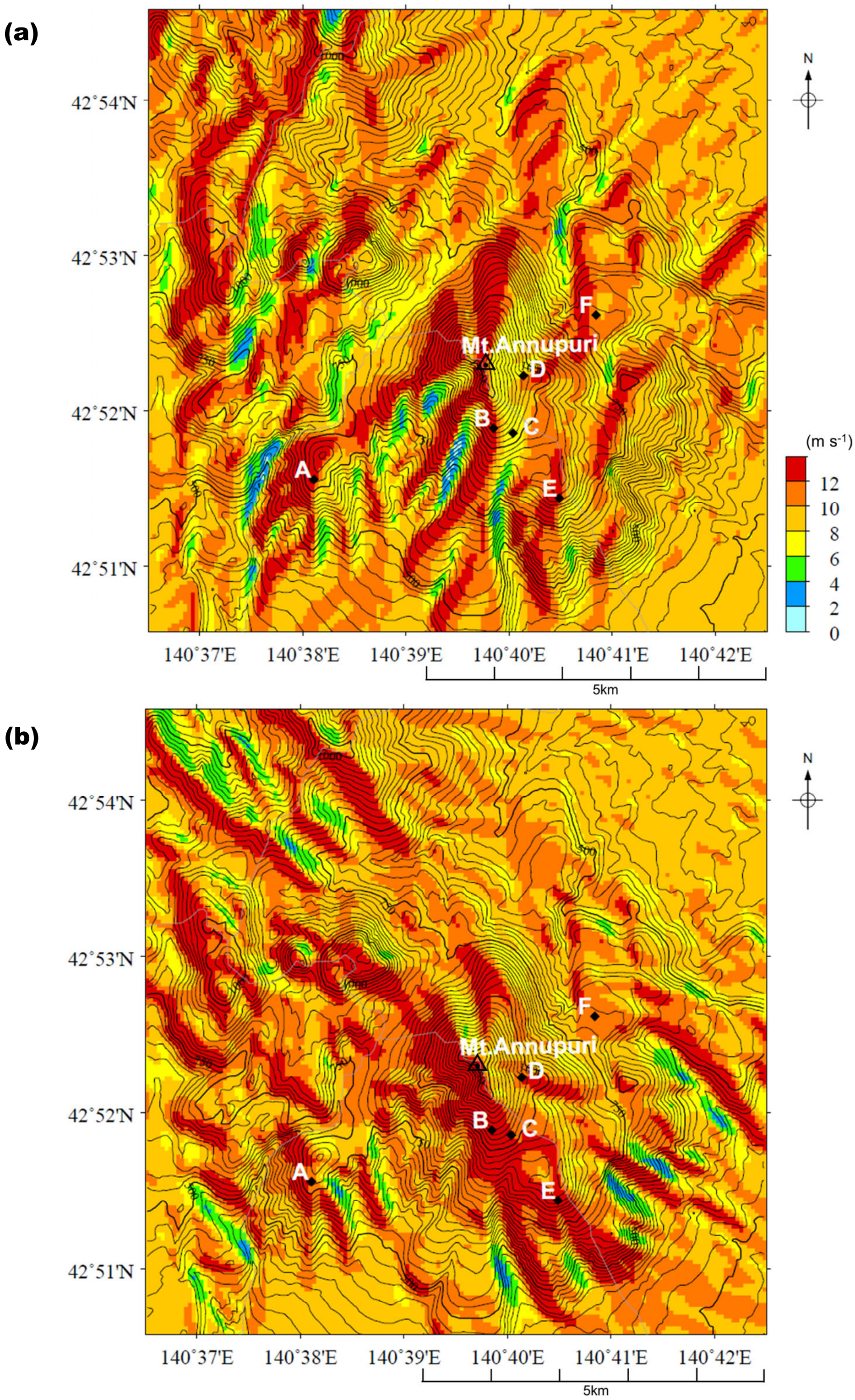

Fig.3.13. Wind speed distributions for the period when winds of 10 m s^{-1} at 10 m above the surface blew into the domain from the corresponding boundary, for winds from the (a) WNW and (b) SW.

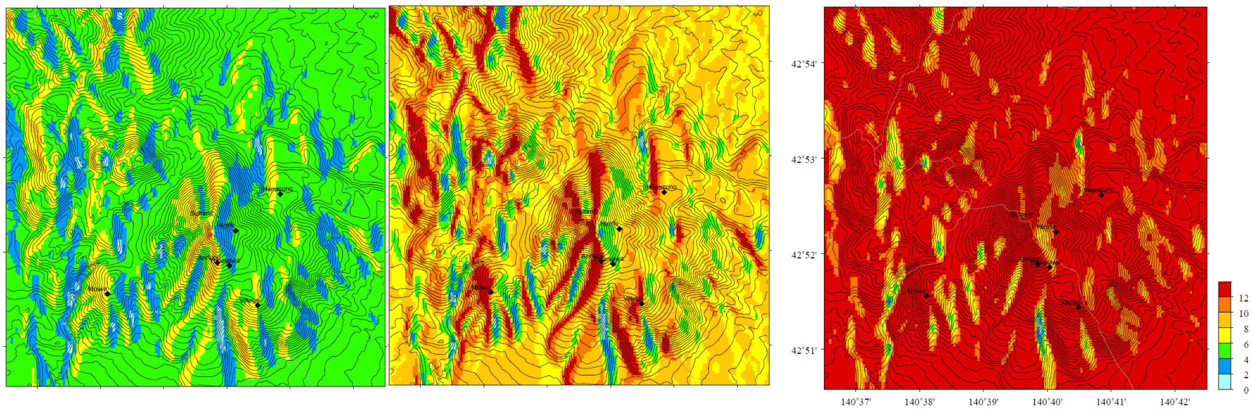

Fig.3.14. Wind speed distributions for the period when winds of 5 m s^{-1} (left), 10 m s^{-1} (center), and 15 m s^{-1} (right) at 10 m above the surface blew into the domain from the corresponding boundary, for winds from the W.

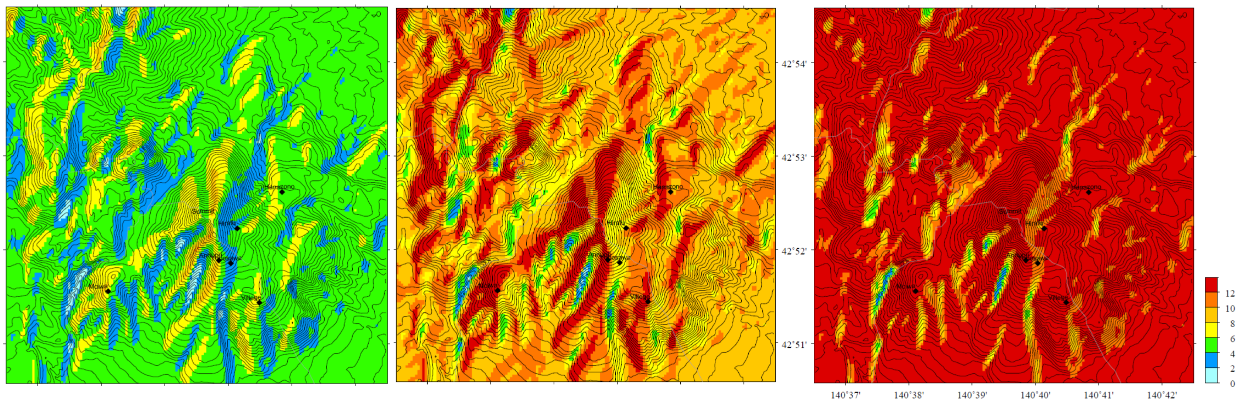

Fig.3.15. Wind speed distributions for the period when winds of 5 m s^{-1} (left), 10 m s^{-1} (center), and 15 m s^{-1} (right) at 10 m above the surface blew into the domain from the corresponding boundary, for winds from the WNW.

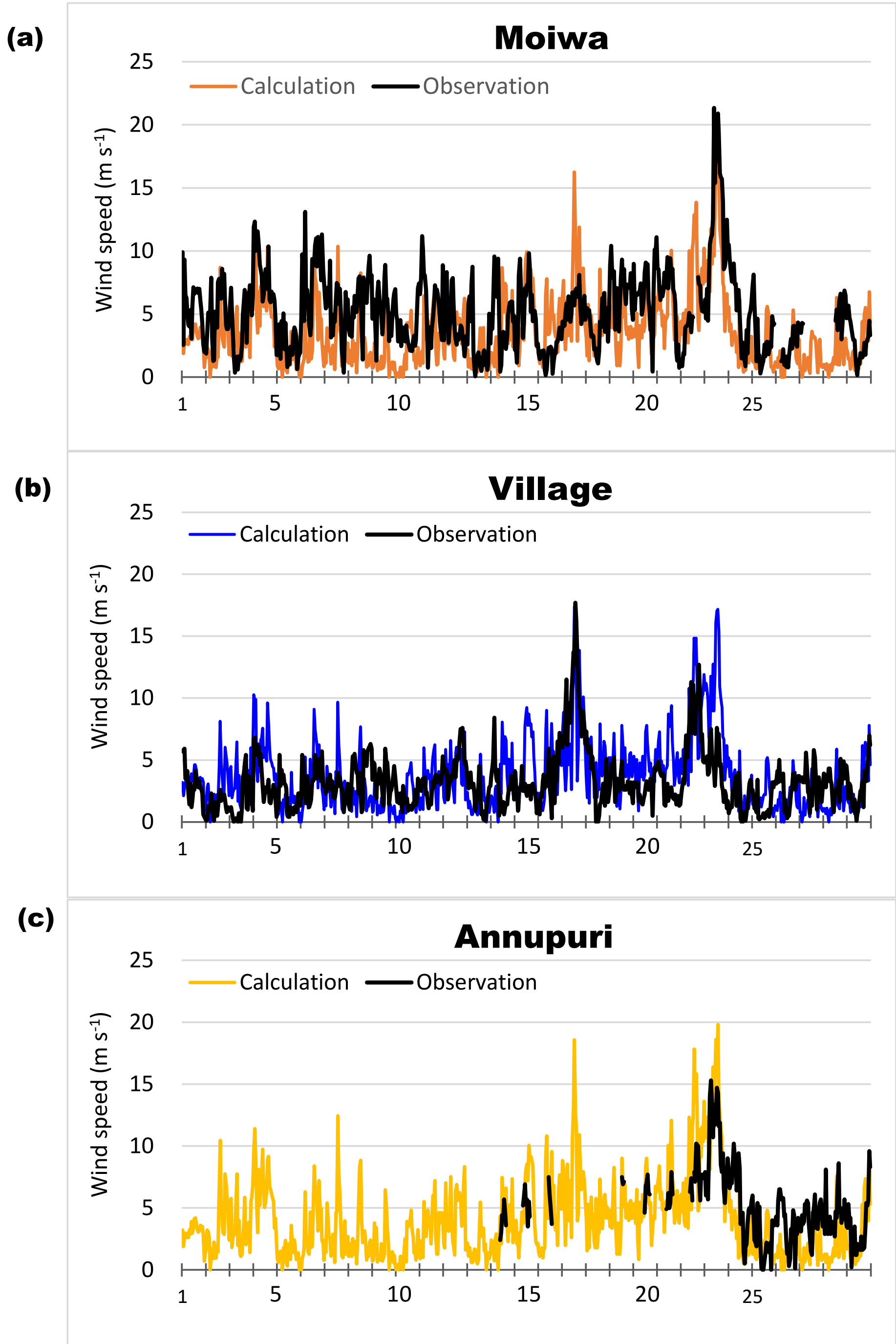

Fig.3.16. Time series of observed and calculated wind speeds in February 2020. (a) Moiwa station (A in Fig.3.1). (b) Village station (E in Fig.3.1). (c) Annupuri (B in Fig.3.1). The observed and calculated wind speeds are shown as black and colored lines, respectively.

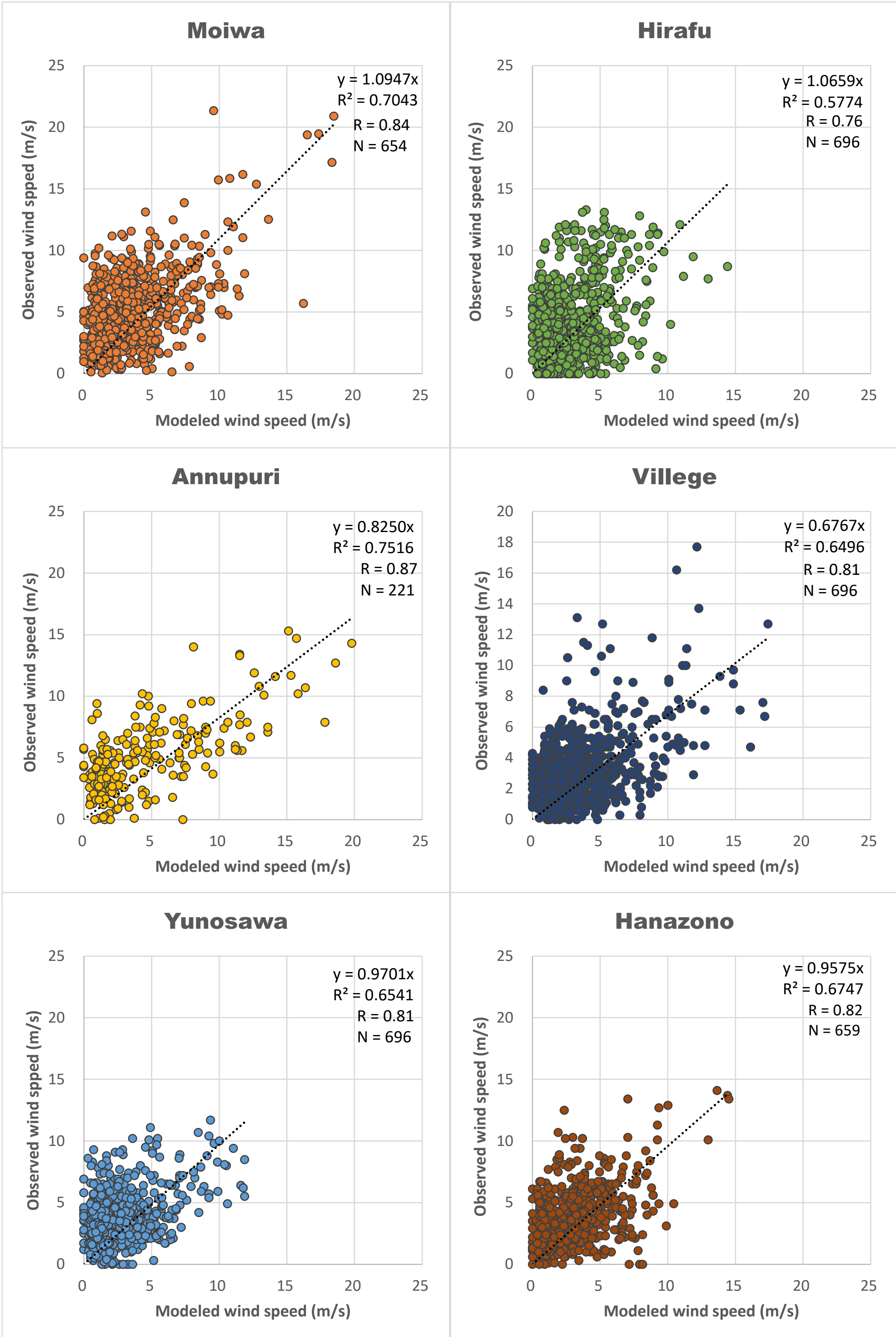

Fig.3.17. The scatter plot of the observed and calculated wind speeds for six observation sites in Niseko, February 2020.

Table 3.4. Statistical analysis of simulated and observed wind speeds at sites across the Niseko region in February 2020. The number of samples (n), correlation coefficient (R), mean bias (observed value – model value), and root mean square error (RMSE) are provided.

	Moiwa	Annupri	Yunosawa	Hirafu	Village	Hanazono
n	654	221	696	696	696	659
R	0.84	0.87	0.81	0.76	0.81	0.82
Bias (m s^{-1})	1.5	0.5	0.9	1.2	-0.5	0.7
RMSE (m s^{-1})	3.3	3.1	2.5	2.8	2.8	2.5

3.1.2 Comparison with the wind tunnel experiments

Fig. 3.18 shows the comparison of wind speed distributions between model calculation and wind tunnel experiment when the wind blew from the west. As is introduced before, winds of 10 m s^{-1} at 10 m above the surface blew into the domain for the model calculations, whereas the wind tunnel experiments were carried out at 3 ms^{-1}. Displayed the calculated wind speeds correspond to the ones at 2 m. On the other hand, wind speeds were measured one mm above the terrain at the experiment. Further, grid size differed largely between the model and the experiment (wind tunnel grid size: 500m; simulation grid size: 50 m). Thus, quantitative comparisons were beyond our scope. Nevertheless, both the experiments and the numerical simulation show that the wind speed generally increases on windward slopes of the mountain and conversely, the wind speed decreases on the leeward slopes. Simulation shows the correct trends in general.

Fig. 3.19 indicates the cross-section from west to east which goes through the summit of the Mt. Annupuri. Here the summit wind speed experimentally measured were adjusted to fit the one for the calculated one. Again, strict comparisons are hard because of the grid size difference. However, general trend of wind variation from west east roughly agree each other.

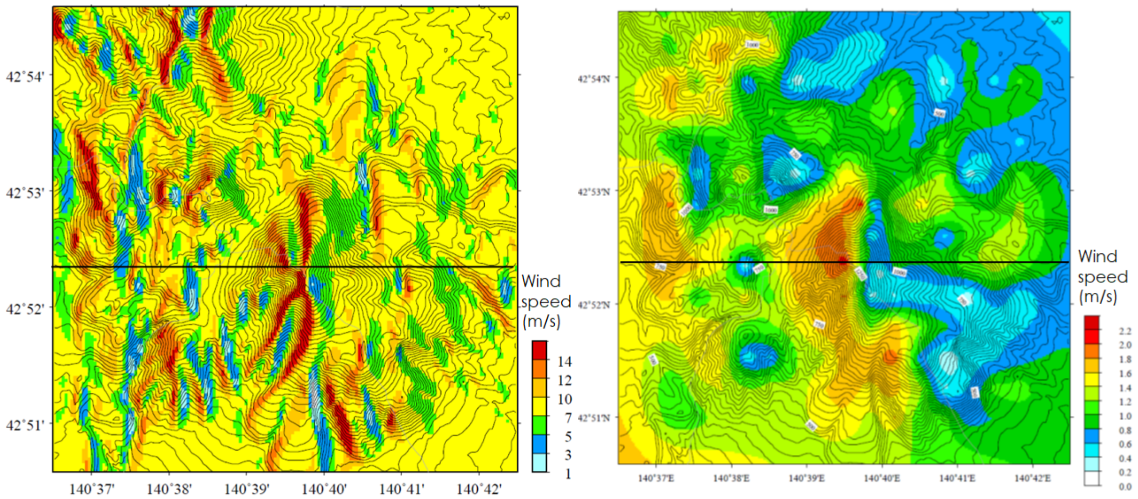

Fig.3.18. The comparison of the wind speed distribution between model calculation (left) and wind tunnel experiment (right). Wind direction is west.

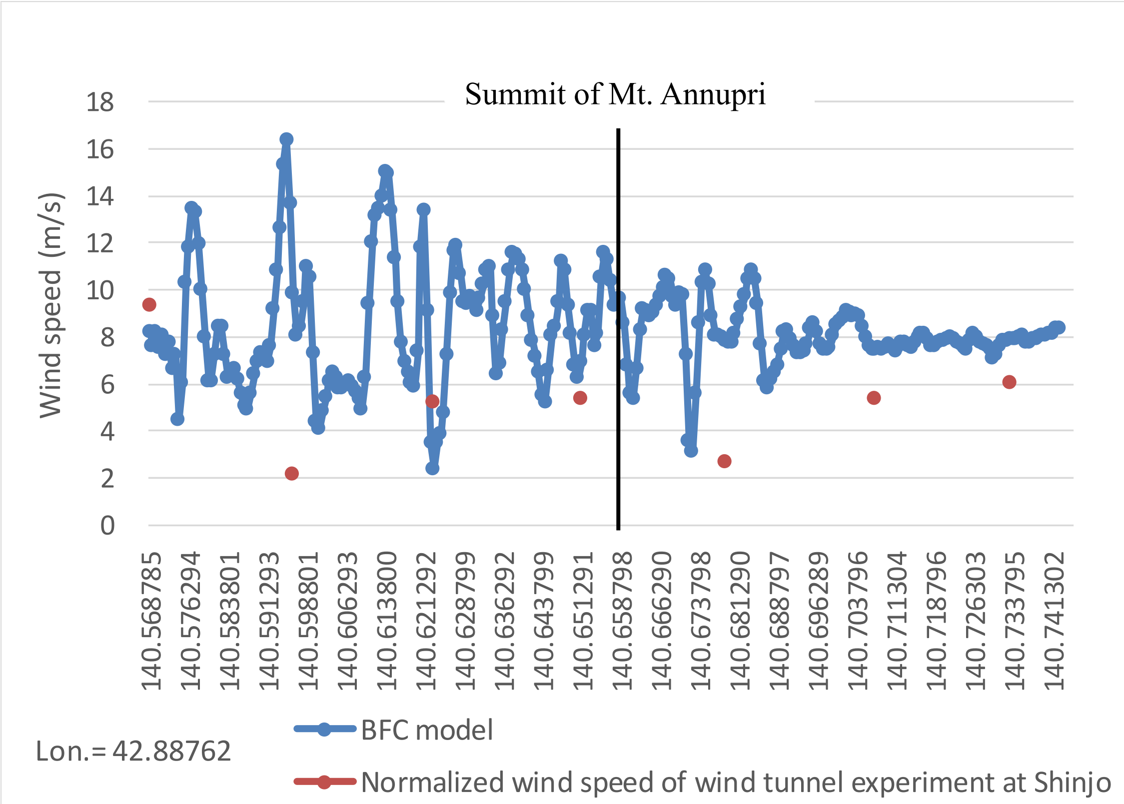

Fig.3.19. The cross-section of wind speed distribution.

3.1.3 Comparison with the moving observations

Mobile observation data with the vehicle in Niseko on 20 October 2016 are displayed in Fig. 3.20 with the model outputs. Detailed data including wind speed, wind direction, and temperature are shown in Appendix D. In Fig. 3.20 maximum wind speeds obtained every 100 m are plotted with circles. On the other hand, model calculation shows the case when the wind blew into the domain from WNW according to the record during the observation period at KA. Wind speed flows into the domain was also adjusted following the data at KA and the output of vehicle was converted from 2m to 10 m high; former is the sensor height of the vehicle and latter is the one at KA. Although unfortunately most of the observation route was outside of the calculation domain, wind speeds roughly agree with area indicated with black circle or box in the figure. However, large differences are also found widely; generally observed one is lower than the calculations. It is probably because the road, along which wind speeds were measured, has dense population of trees on both sides as shown in Fig. 3.11. If we could try the same observation in the mid-winter, most of the trees shed their leaves and may not protect the wind. However, northern part of the route shown in the figure were closed in winter.

On the other hand, along the observation route in Wakkanai, population of trees and obstacles were rather sparce. Fig. 3.21 shows the wind speed measurement conducted in December 2009 along the route introduced in Fig. 3.12 with the model calculation output.

Both agreed quite well, and validity of the model was attested.

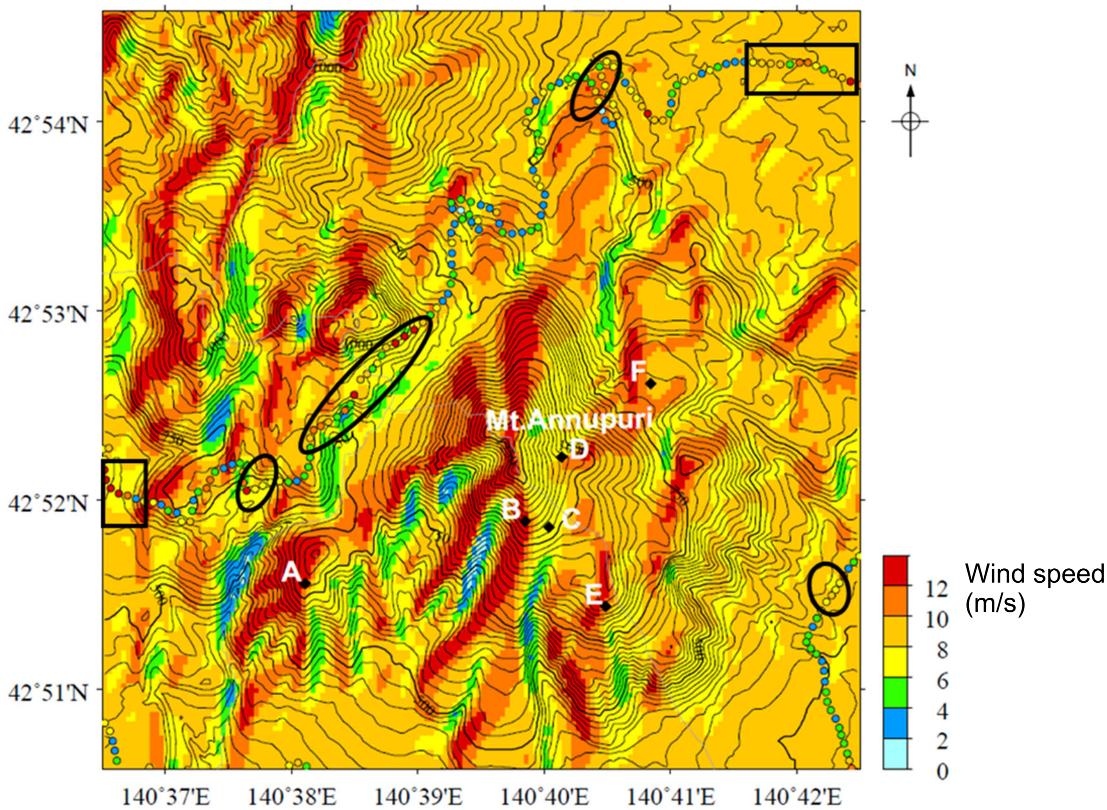

Fig. 3.20. Comparison of the wind speed distribution between the moving observation and the numerica simulation on 20 October 2016. Former shows the maximum wind speeds obtained every 100 m with circles, whereas calculation shows the case when the wind blew into the domain from WNW based on the record during the observation period at Kucchan AMeDAS. Wind speed flows into the domain was also adjusted following the AMeDAS data and the observed data are converted from 2 m to 10 m high; former is the sensor height of the vehicle and latter is the one at KA.

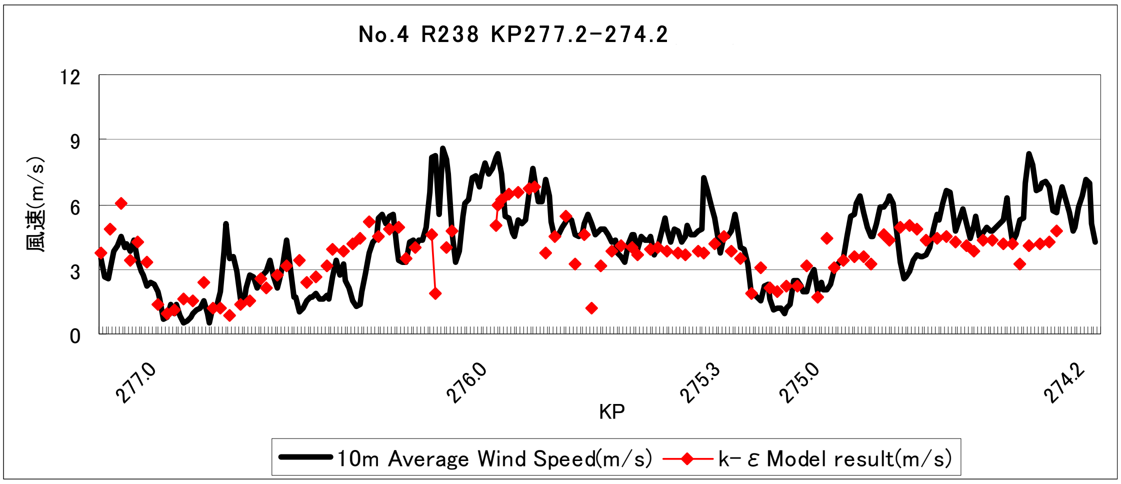

Fig. 3.21. Comparison of wind speeds obtained with the moving observation (black) at Wakkanai in December 2009 (along Route 238) and the numerical simulations (red).

3.2 Snowdrift formation

3.2.1. Case study

We obtained numerical results for snowdrift formation across the target area. Here we introduce the results for 23 February 2020 as a case study, when a cyclone passed over Hokkaido and produced a typical winter atmospheric pressure pattern and brought strong winds and snowfall. Figure 3.22(a) shows the meteorological conditions recorded at KA. High wind speeds (>10 m s^{-1}) were observed between 11:00 and 14:00 local time (LT), and the snow depth increased by nearly 25 cm.

Since the wind directions and speeds at the reference point, which corresponds to KA, are almost the same as the boundary conditions for all of the 16 wind directions, we first divided the observed hourly wind speed at KA into three categories: $\leq 5, >$

$5\ to\ 10, and\ >\ 10\ m\ s^{-1}$. We then obtained the snow deposition and erosion rates over the target area for 5, 10, and 15 m s^{-1} based on the KA wind direction and the wind speed ratio distribution across the study area. Calculated snow drift 5, 10, and 15 m s–1 for wind direction of W and WNW are shown in Fig. 3.23. and Fig. 3.24. We set the $\leq 5, > 5\ to\ 10, and\ >\ 10\ m\ s^{-1}$ wind speeds at KA to 5, 10, and 15 m s^{-1}, respectively, and evaluated the change in snow depth in each grid cell by multiplying the deposition and erosion rates by their associated durations. Snowfall rates of 0–6 cm h^{-1}, which are assumed to be uniform over the area, are also included in the calculations (Fig. 3.22 (a)).

An example of temporal changes in the snow depth distributions is shown in Figure 3.25. The snow depth is relatively thick and evenly distributed across the entire area at 10:00 LT (Fig. 3.25. (a)). However, the snow distribution was becoming localized by 12:00 LT (Fig. 3.25. (b)), with obvious zones of preferential drift as the wind speed increased. An uneven snow distribution was clearly recognized by 21:00 LT (Fig. 3.25. (c)), whereby snow was removed from the windward side of the ridge and accumulated on the leeward side and valley after the snowfall ceased and the winds weakened. We overlaid the snowdrift observations of Dr. Y. Ito that were acquired in March 2021 (pers. comm.) onto the modeled snowdrift distribution in Fig. 3.25. (c). Further three locations from I to III where the snow drifts were clearly recognized as shown in Fig. 3.26, correspond well with the calculations. Obviously, we cannot make a direct comparison of the calculated drift distribution and observations because the former is based on a single storm event, whereas the latter shown in Figs. 3.25(c) and 3.26 represents the observed accumulation for almost an entire winter. However, we note that the locations of the snowdrifts in the region agree fairly well.

Finally, we applied the above case to assess its effectiveness in avalanche warning. Two locations (G and H in Fig. 3.25 (c)) were selected for the analysis. There was substantial snow accumulation in both areas, and sites G (Osawa) and H (Harunotaki) are two areas where a number of snow avalanche accidents have previously been reported (McElwaine et al. 2000; Nishimura et al. 2005). Substituting the obtained snow depth and the air temperature into SSCM (Komatsu and Nishimura, 2020), the snow stability index (SI), which is the ratio of the shear stress to the shear strength of snow, was calculated. As shown in Fig. 3.22. (b), the SI values at both locations decreased to 2.0, which is much smaller than the value estimated at KA. Hirashima et al. (2006, 2008) set 2.0 as an appropriate SI threshold for evaluating avalanche susceptibility in Japan, indicating that the modeled avalanche danger level was high at both locations. Fortunately, there were no reported snow avalanche incidents during this period. However, it is clear that applying the observed snow depth at a given location in the study area is much more appropriate for snow avalanche warning than the observed snow depth at KA.

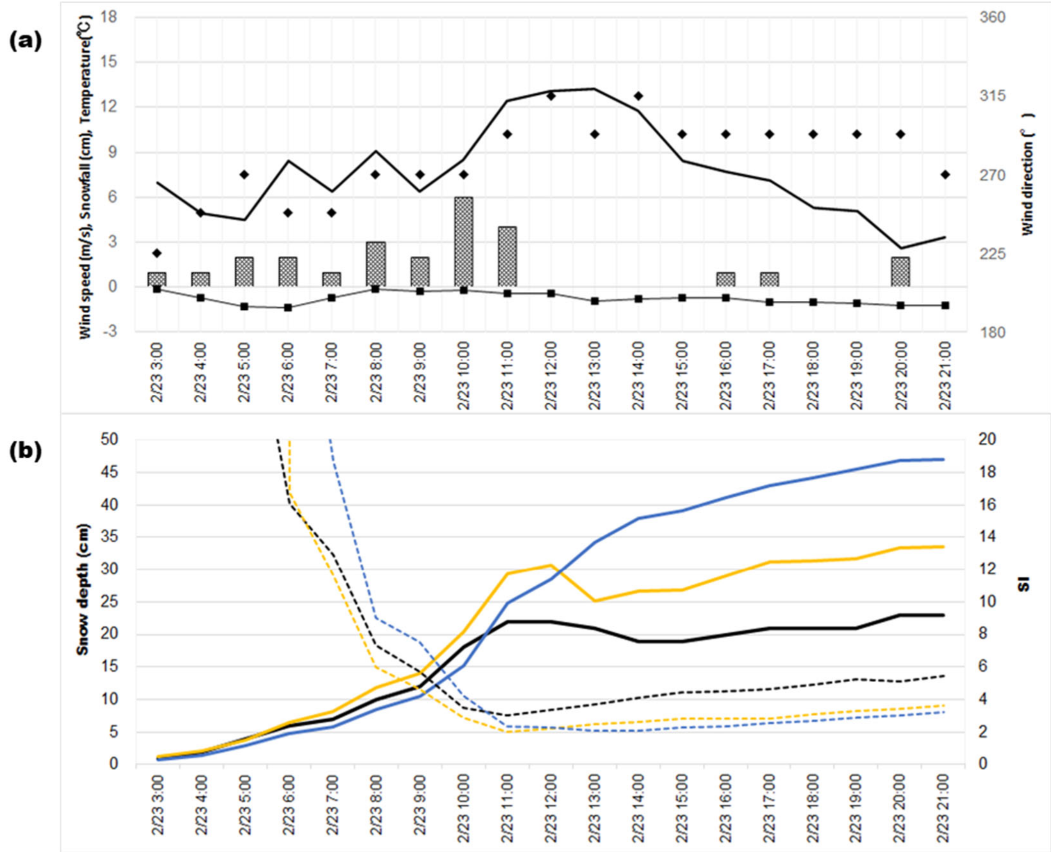

Fig. 3.22. (a) Time series of observed meteorological variables at KA during the case study on 23 February 2020. The wind speed (solid line), wind direction (diamonds), snowfall (gray boxes), and temperature (line with solid squares) are shown. (b) Solid lines show the snow depth at KA (observed, black), G (calculated, yellow), and H (calculated, blue). Dotted lines indicate the SI calculated with the SSCM at KA (black), G (yellow), and H (blue). The sites G (Osawa) and H (Harunotaki) are the locations where snow avalanche accidents have previously been reported.

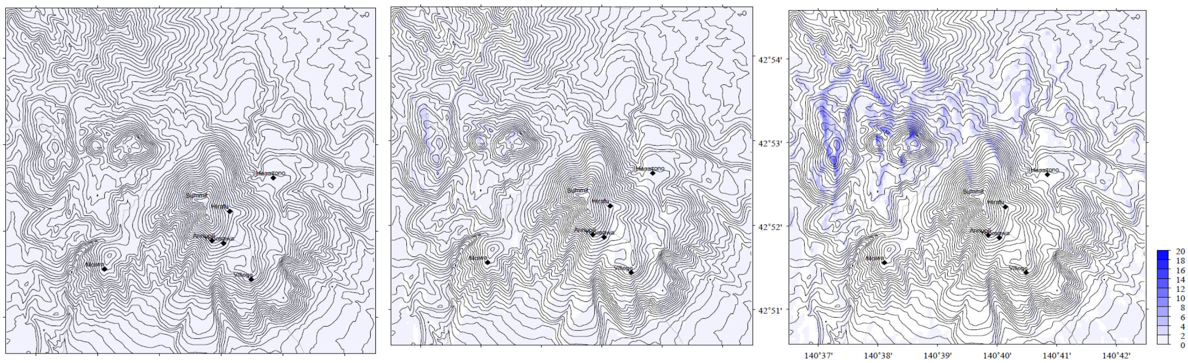

Fig.3.23. Calculated snowdrift distribution when winds of 5 m s^{-1} (left), 10 m s^{-1} (center), and 15 m s^{-1} (right) blew into the domain from the direction of W.

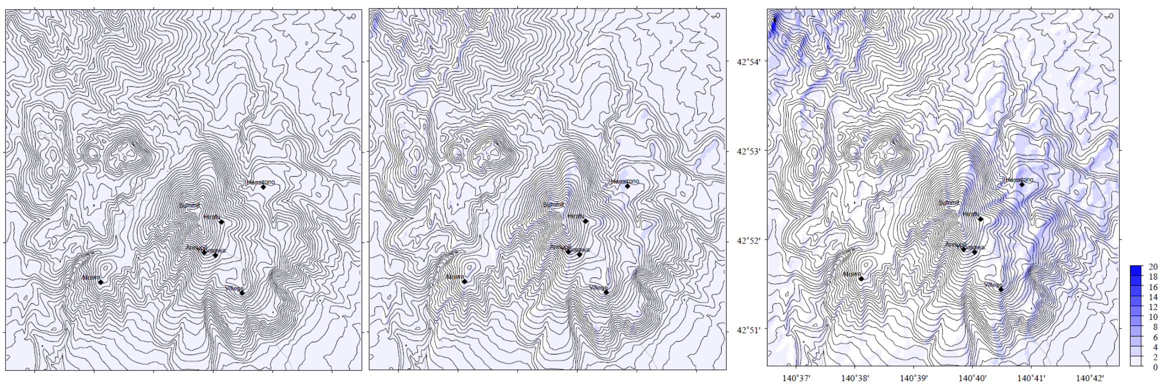

Fig.3.24. Calculated snowdrift distribution when winds of 5 m s^{-1} (left), 10 m s^{-1} (center), and 15 m s^{-1} (right) blew into the domain from the direction of WNW.

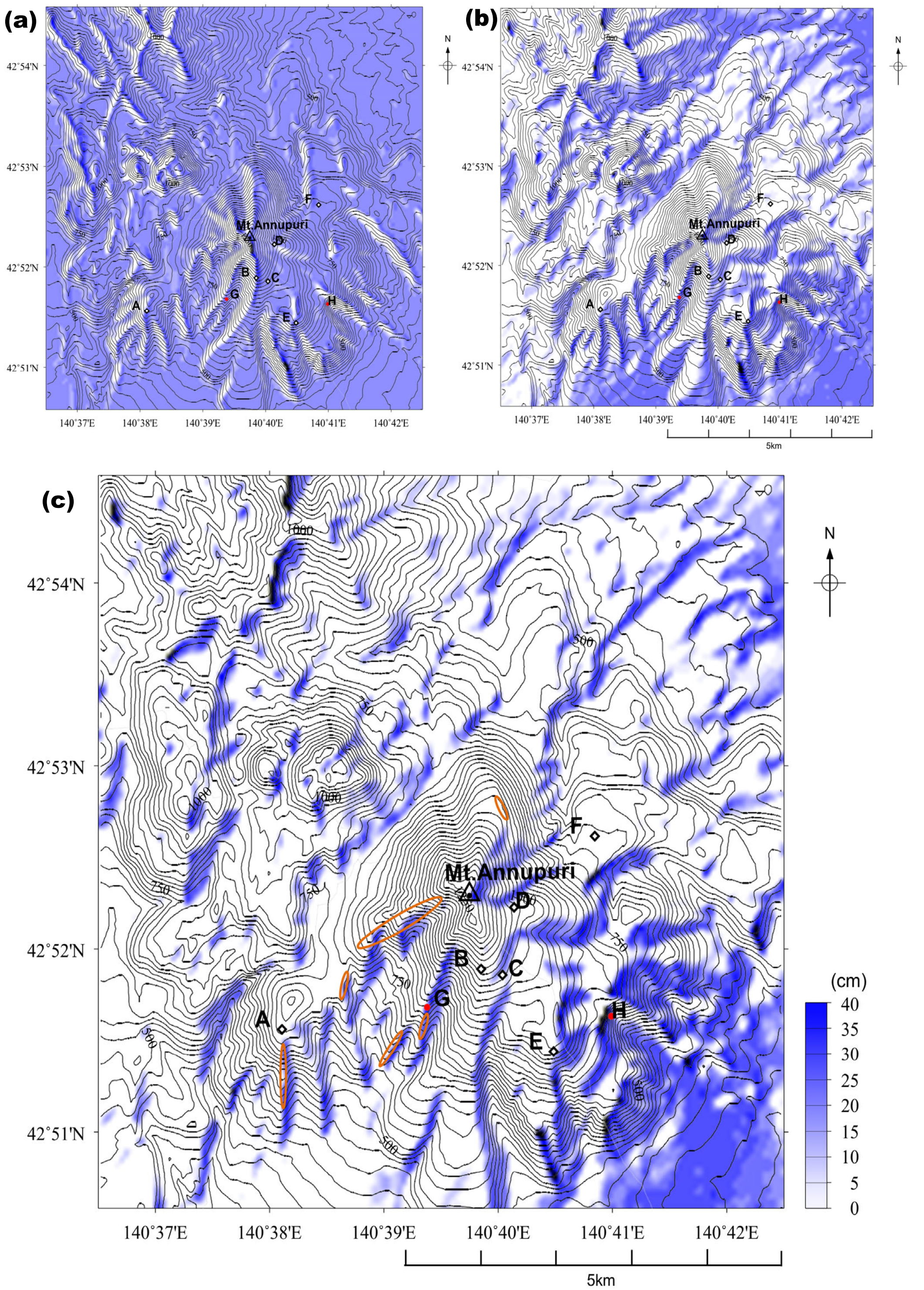

Fig. 3.25. Calculated snowdrift distribution at (a) 10:00, (b) 12:00, and (c) 21:00 local time on 23 February 2020. Points A to F mark the locations of the wind observation points. G and H (in red) are Osawa and Harunotaki, respectively. The orange areas are snowdrifts that were visually confirmed by Dr. Ito (NIED).

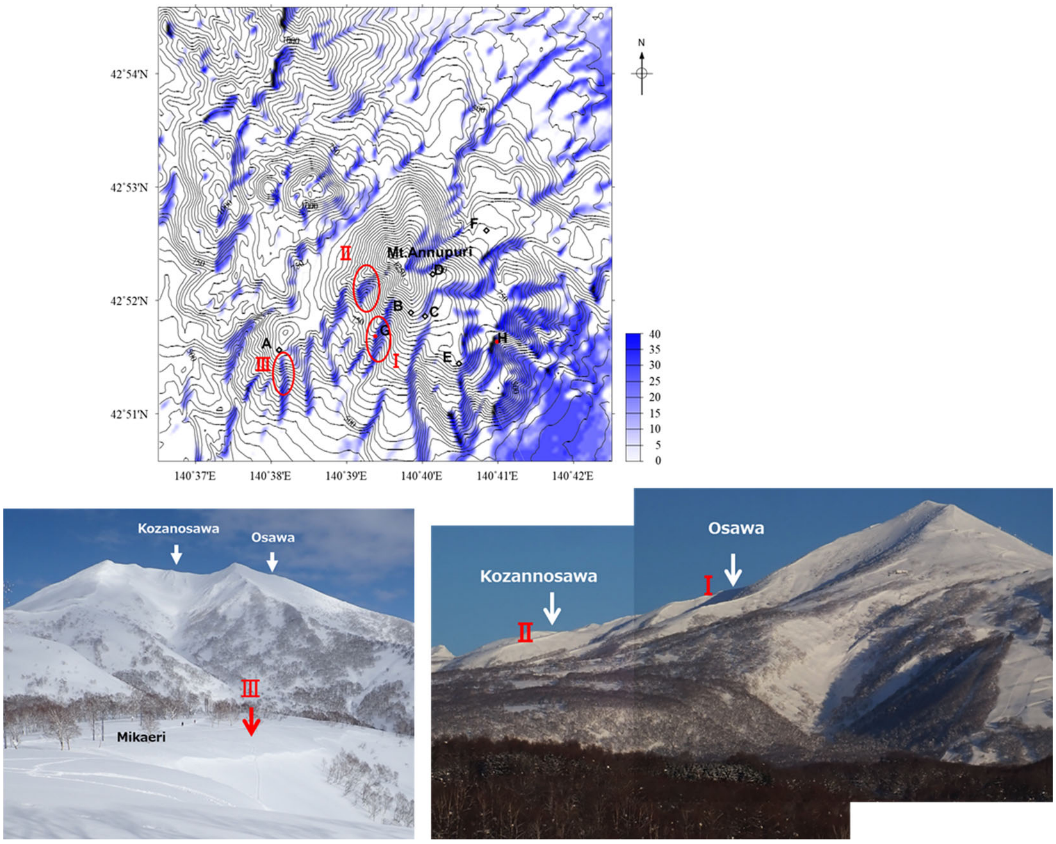

Fig. 3.26. Calculated snowdrift distribution (above) and observed snowdrifts at I to III by Dr. Ito (NIED).

3.2.2. Comparison with wind tunnel observations

Comparison between the model calculation and wind tunnel observation, when the wind blew into the domain from west, was also carried out as shown in Fig.3.27. Left figure shows the snow drift rate, thus the negative value indicates the accumulation, whereas the positive value means the erosion. Thus, the output of the model is multiplied by minus one to compare with the wind tunnel output directly. Regions exposed to the strong wind in Fig. 3.18 correspond to the erosion zone and outcome of the simulations and wind tunnel experiments agreed very well each other. Further, larger accumulations are recognized not only in the valley but also along the downstream shoulder (eastern side) of ridges in both cases. Same trend can be also recognized from Fig. 3.28. which depicts the cross section of wind speed profile along the black line in Fig. 3.28. Although quantitative evaluations are beyond our scope, wind tunnel experiments also proofed the validity of the model qualitatively.

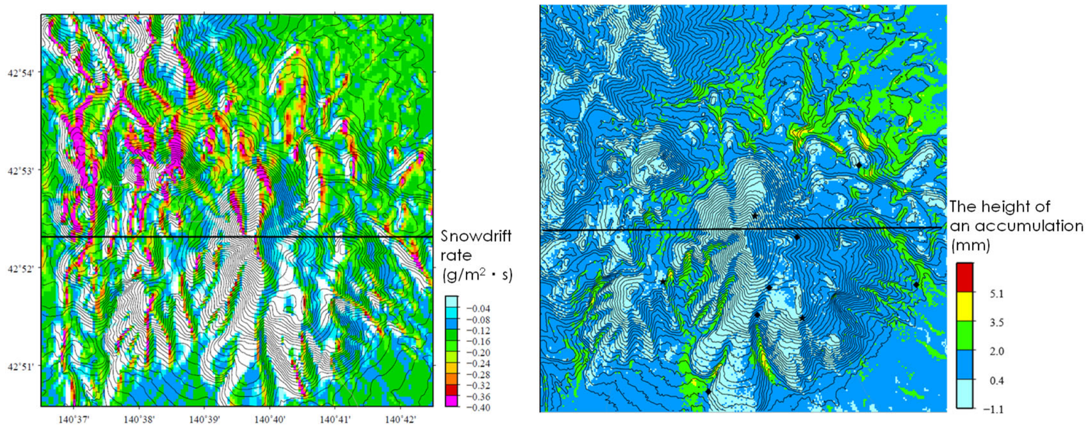

Fig.3.27. The comparison of snow accumulation between model calculation (left) and wind tunnel experiment (right). In the left figure, white color indicates the erosion, and the accumulation increases from blue to red. The black lines show the cross-section in Fig. 3.28.

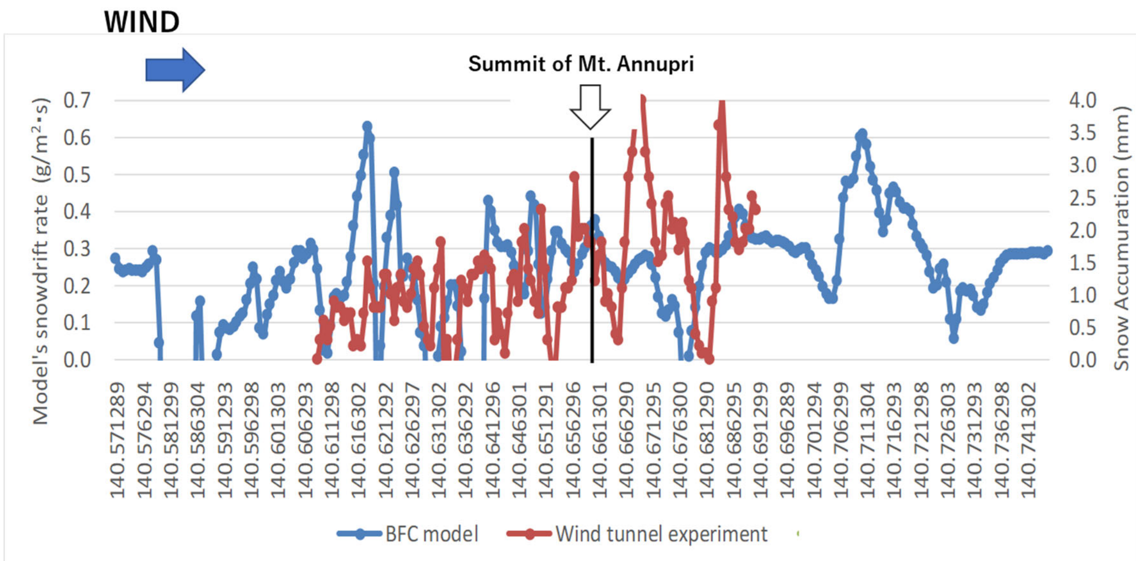

Fig.3.28. Comparison between the model calculation and the wind tunnel experiment. Model output shows the accumulation rate along the cross-section in Fig. 3.27 and wind tunnel experiment gives the height of accumulated activated clay.

4. Discussion

We introduced a new set of procedures to evaluate snowdrift distribution over complex topography and improved the accuracy of snow avalanche warning systems. We selected the Niseko region as the target area due to its popular ski resorts and dense coverage of weather stations across the region. We first obtained the wind distribution map at a 50-m grid spacing for the 16 wind directions of the compass rose. We then employed these wind maps to calculate the amount of snow erosion and deposition in each grid cell. Our February 2020 case study demonstrated that the model output agreed fairly well with the recorded wind speeds and snowdrift distribution observations across the area. Therefore, we can reasonably conclude that it is appropriate to incorporate our presented snowdrift analysis procedure into a snow avalanche warning system that employs the SSCM (Komatsu and Nishimura, 2020). In fact, when we applied the system to the avalanche release during the strong wind of nearly 20 m s^{-1} in Wakkanai, Hokkaido, it successfully indicates the avalanche danger level with high accuracy, as is introduced in Chapter IV. However, there is still room for improvements as shown below.

We set KA as the reference point in the case study because the variety of meteorological data are available. However, as the reference point in the model we had to set the easternmost grid point at the same latitude as KA, since KA is outside of the model domain. Although the wind speeds and directions at both points were almost the same for all of the wind directions, the model domain needed to be expanded to include KA. We note that the avalanche warning system should be combined with the hourly meteorological forecasts that are provided by JMA and the Japan Weather Association (JWA) on a 1-km grid. A smaller model domain is probably sufficient for practical applications in the future.

We divided the observed wind speeds at KA into three categories, $\leq 5, > 5\ to\ 10, and\ >\ 10\ m\ s^{-1}$, and obtained their associated snowdrift distribution with applying the result of 5 m s^{-1}, 10 m s^{-1} and 15 m s^{-1} respectively. Thus, the degree of snow erosion and deposition might be overestimated. Although this approach was introduced to reduce the computational requirements, the pitch of the wind speeds in the calculation should also be considered to further improve the accuracy of the model results. Further, the finer grid spacing might be taken into consideration. Although we used 50 m grid size to reduce the computational load, the higher-resolution simulations seem suitable to express the smaller-scale deposition pattern such as snow dunes and cornices (Mott and Lehning 2011).

5. Conclusions

The snowdrift distributions obtained in this study were qualitatively compared with visual observations and wind tunnel observations. However, more precise observations in the target area, such as those obtained via airborne laser Doppler profiling over the entire target area, are desirable for a quantitative comparison and a more accurate snowdrift evaluation. Furthermore, our simulation only employed a single snowdrift density of 100 kg m^{-3}, which is probably not always true; additional snowdrift densities should be considered. Precise data acquisition is also needed to better constrain future model simulations.

Snowdrifts generally develop over time during the winter season, and the topography of the snow surface changes accordingly. These drifts may then evolve substantially based on the wind speed and direction effects over the terrain. Such interactions between the wind field and snowdrift formation need to be considered to simulate snowdrift formation and evolution more precisely.

IV. Summary and outlook

In this research, we have developed a snow avalanche warning system combined the SSCM which is able to reproduce the change in snowpack properties substituting only air temperature and precipitation or snow depth and a system to calculate snow transport and deposition across complex topography.

In Chapter II, after introducing the model configuration of SSCM, we have compared the model outputs with the snowpack observations. Then, application to the avalanche incidents were carried out. The SSCM can reproduce changes in snowpack properties having good accuracy that is comparable to the more sophisticated model like SNOWPACK. Comparison with the avalanche incidents also suggest the suitability of the SSCM. However, the SIs calculated for a couple of avalanche cases are apparently larger than the values which is critical for the avalanche release. Then, we recognized the effect of snow drifts should be incorporated into the system to make it more precise.

In Chapter III, we developed a system to calculate snow transport and deposition across complex topography and coupled this system to the SSCM. We then applied this coupled model to the Niseko area, Hokkaido, Japan. For this target area, we have used anemometers to verify the performance of air flow simulations. Also. we assigned the wind tunnel and moving vehicle observation data to compare with calculations. For snowdrift simulation results, we used the snowdrift observations by Dr. Y. Ito (NIED) and the wind tunnel observation using the activated cray to verify the modeled snowdrift distributions. Additionally, we have calculated SI results for a strong wind case in Niseko (no avalanche) and an avalanche case in Wakkanai by the SSCM. Both results are compatible for the situation of avalanche risks.

This system still has some tasks to overcome, for example, a more accurate snowdrift evaluation such as a change of density and interaction between snowdrift and air flow. However, this system have a possibility to more useful information to prepare for surface avalanche.

Nowadays JMA observation network allows us to generate accurate weather forecasts. By inputting these data into the SSCM, we have developed an avalanche warning system for road administrators. The system calculates the SI every hour and it is offered to whom it may concern through the specific website, the warning e-mail and FAX for 24 hours as shown in Fig. 4.1. So far, it worked pretty well in general. However, the accuracy strongly depends on not only the accuracy of the weather forecast it self but also the amount of snow accumulated over the target region. Apart from the former issue, the latter can be solved with introducing the procedures developed in Chapter III in this study.

Figs 4.2 to 4.4 show the case when we applied both SSCM and the snow drift simulation procedures in Wakkanai, Hokkaido. A large volume of snow avalanche broke out at the position shown in Fig. 4.2 at 1845 JST, 13 February. When we calculate the SI simply using the recordings at Soyamisaku AMeDAS, which is the closest observation site, and do not take into account the snow drift effect, change in SI are given as Appendix C. Although SI decreased below the critical value, it increased gradually and reached to around 6 at the time of the avalanche release. The avalanche site is located on the route 238 which goes along the seashore of Okhotsk sea as is shown in Fig. 3.12 and the monsoon from the west becomes strong in winter season occasionally. In fact, Fig. 4.2 shown the wind speed at Soyamisaku AMeDAS increased from 5 to 20 m s^{-1}. Thus, the snow re-distribution by the wind is inevitable. Applying the snow drift model developed in this study, change in the snow heights at A and B, both of which are very close to the avalanche release point are shown in Fig. 4.3. It increased drastically from 1300JST and amounted to two to three m high. Substituting the snow height obtained into the SSCM, the SI was recalculated and is shown in Fig. 4.2. SI at the avalanche release was less than one and we can conclude this procedure is appropriate to calculate the avalanche danger level with high accuracy.

At this stage, the avalanche warning system is mainly focused on the surface avalanche and it doesn’t cover the full-depth avalanches in early spring when the highest air temperature is continued to be over zero degree. Considering the snow melting process precisely we would like to improve the system, which is able to forecast the danger of not only the dry snow avalanches but also the wet ones, before long.

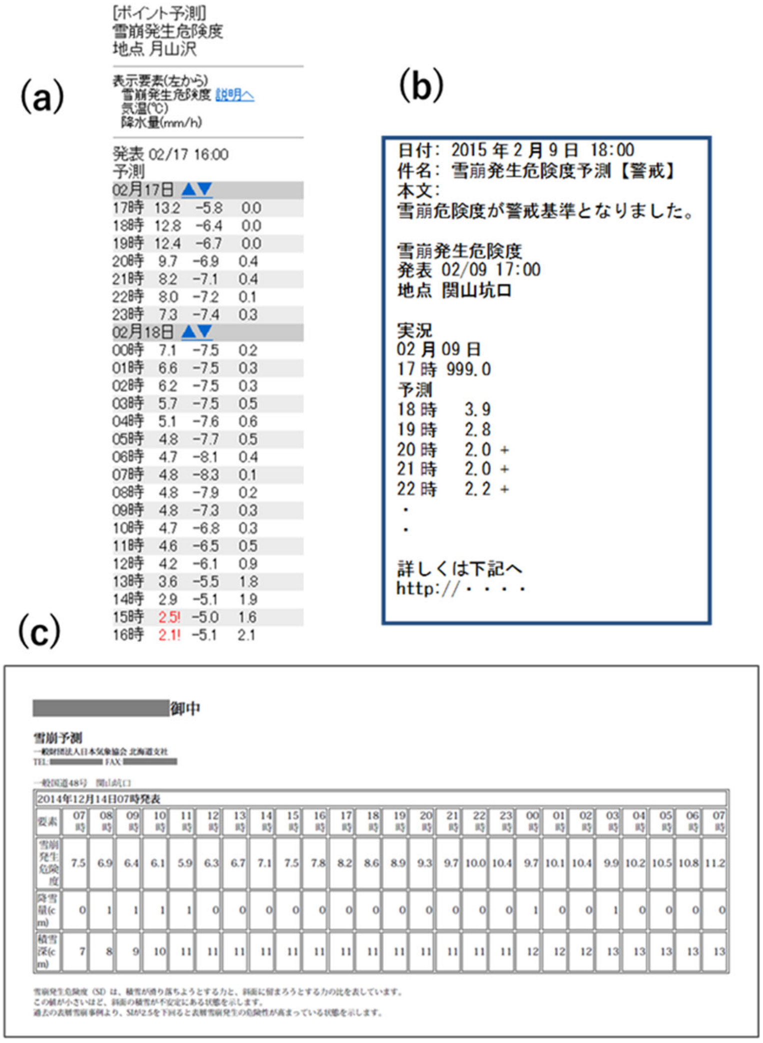

Fig. 4.1. Avalanche warning information provided to the road administrators.

(a) the website for the mobile phone, (b) the warning e-mail, and (c) FAX

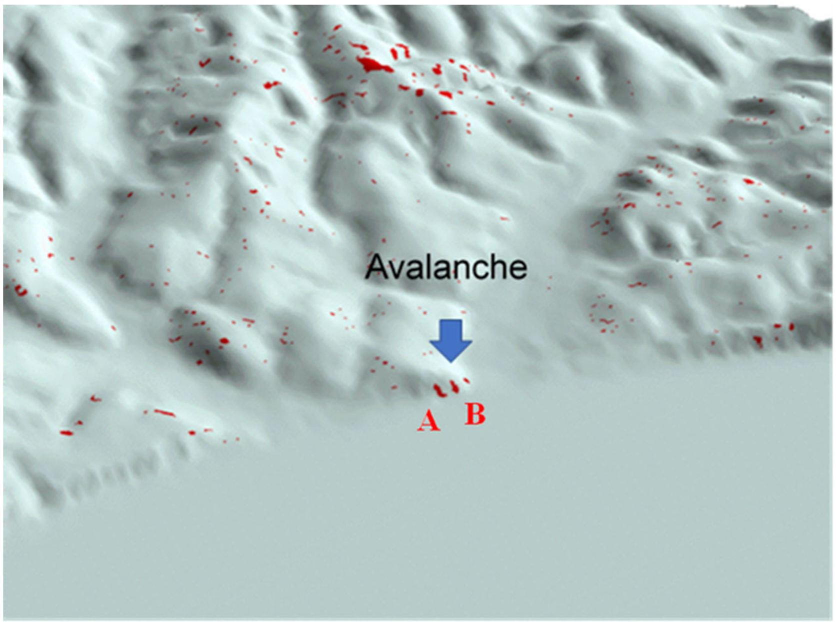

Fig. 4.2. Snow accumulation near the avalanche release point. The area shown in red indicates the snow height became larger than 0.5 m at the time of the avalanche release.

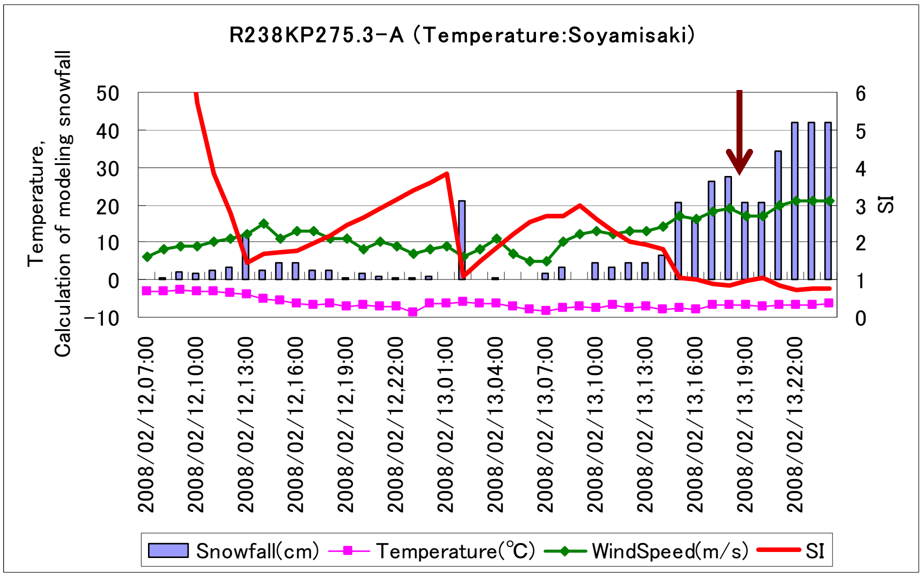

Fig. 4.3. Time series of air temperature, wind speed observed at Soyamisaki AMeDAS, and snow fall amount based on the change in snow depth at A in Fig. 4.2, from 12 to 13 February 2008. Calculated SI is also shown.

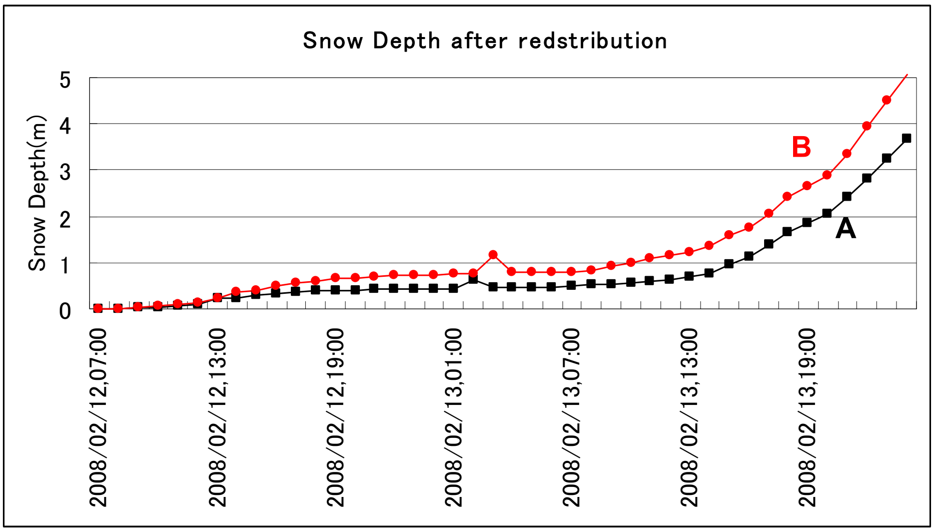

Fig. 4.4. The time series of calculated snow accumulation due to the snow drift near the avalanche release point (at A and B in Fig.4.2).

Acknowledgements

I wish to express my sincere thanks to Prof. Koji Fujita, Prof. Tetsuya Hiyama, and Associate Prof. Akiko Sakai at Nagoya University (NU) for evaluating my doctoral paper, and kind and helpful discussions. I am also very grateful to Dr. Kouichi Nishimura, Prof, Emeritus (NU) for his deep suggestions and persevering advice when we had compiled the research results. Further, I would like to mention that my research was truly supported by Japan Weather Association (JWA).

I would like to thank my colleagues at Cryosphere Research Laboratory in Graduate School of Environmental Studies, NU for useful discussions and suggestive comments. I acknowledge laboratory member of Dr. Hirofumi Niiya (currently Niigata University), Dr. Sojiro Sunako (currently Snow and Ice Research Center, NIED), and Mr. Hiroki Tsuji (currently Railway Technical Research Institute).

I am also particularly grateful to Dr. Takamitsu Sato (JWA) for his constructive suggestions and giving his careful assistance in numerical modelling. Dr. Hironori Nakabayashi, and Dr. Keishi Ishimoto kindly helped snowpack observations and conference presentations and always discussed intensively. Thanks a lot.

The wind tunnel experiments were performed at NRI-HRO and Shinjo Cryospheric Environment Laboratory, NIED. I would like to thank Dr. Takuya Tsutsumi (NRI-HRO) for technical assistance with the wind tunnel experiments. Further, I am grateful to Niseko

Town and NIED for providing the wind data that were acquired across the Niseko ski area. I thank Dr. Yoichi Ito (NIED) for providing snowdrift information across the Mt. Annupuri region. Hokkaido RDB, MLIT kindly supported our snow pit observations and supplied meteorological data and information regarding the snow avalanches in the Tohoku region was provided by Tohoku RDB, MLIT; I would like to express my sincere thanks to these organizations.

This work was partly supported by JSPS KAKENHI Grant Number JP15H02992.

References

Abe, O., Mochizuki, S., Yamaguchi, S., Hirashima, H., Sato, A., 2005: Shear strength of depth hoar snow layers. *Cold Region Technology Conference Proceedings*, **21**, 249–252, (in Japanese).

Bagnold, R. A. 1941: The physics of Blown Sand and Desert Dunes, 265 pp. Methuen, New York.

Bartelt, P., Lehning, M., 2002: A physical SNOWPACK model for the Swiss avalanche warning Part I: numerical model. *Cold Regions Science and Technology*, **35**, 123–145.

Brun, E., Martin, E., Simon, V., Gendre, C., and C. Coleou, 1989: An energy and mass model of snow cover suitable for operational avalanche forecasting. *J. Glaciology*, **35**(121), 333–342.

Endo, Y., Kominami, Y., Yamanoi, K., Niwano, S., 2002: Calculation method of hourly snowfall and initial snow density using the visco-elastic deformation. *Seppyo*, **64**, 3–13 (in Japanese with English abstract).

Endo, Y., Kominami, Y., Yamanoi, K., Takeuchi, Y., Murakami, S., 2004: Calculation method of snow depth and density from precipitation data. *Seppyo*, **66**, 17–25 (in Japanese with English abstract).

Fierz, C., Armstrong, R., Durand, Y., Etchevers, P., Greene, E., McClung, D., Nishimura, K., Satyawali, P., Sokratov, S., 2009: The International Classification for Seasonal Snow on the Ground. *In: Tech. Doc. Hydrol.*, **83**. UNESCO, Paris, pp. 80.

Hirashima, H., K. Nishimura, E. Baba, A. Hachikubo, and M. Lehning, 2004: SNOWPACK model simulations for snow in Hokkaido, Japan. Ann. Glaciol., 38. 123−129.

Hirashima, H., Nishimura, K., Yamaguchi, S., Sato, A., and M. Lehning, 2006: Evaluation of snow stability index in a snow cover model for avalanche accidents. *Cold Region Technology Conference*, **22**. 26-30. (in Japanese)

Hirashima, H., Nishimura, K., Yamaguchi, S., Sato, A., and M. Lehning, 2008: Avalanche forecasting in a heavy snowfall area using the snowpack model. *Cold Reg. ci. Technol.*, **51 (2-3)**. 191-203.

Izumi, K., Kawashima, K., Iyobe, T., Matsumoto, T., 2014: Characteristics of avalanche accidents caused by heavy snowfall in mid-February 2014. *Department of Grants-in-Aid for Scientific Research Report*, 111–118 (in Japanese).

Iversen, J. D., Greeley, R., White, B. R., and J. B. Pollack, 1980: Eolian erosion of the Martian surface, Part I; Erosion rate similitude. *Icarus*, **26**(3), 321-331.

Kajikawa, M., 1989: Relationship between the density of new snow and snow crystal form. *Seppyo*, **51**, 178–183 (in Japanese with English abstract).

Kajikawa, M. Ono, N., 1990: Relationship between the compactive viscosity of new snow and the shape of snow crystals. *Seppyo*, **52**, 283–287 (in Japanese with English abstract).

Kamiishi, I., Nakamura, K., 2016: Natural Disaster Research Report.National Research Institute for Earth Science and Disaster Prevention, Japan, **49**, 1–10 (in Japanese with English summary).

Kawashima, K., Iikura, S., Sugiyama, S., Endo, T., Fujii, T., 2002. Development of a simple method for estimating daily amount of snowmelt with the object of application to railway disaster prevention. Seppyo, 64, 605–615 (in Japanese with English abstract).

Kikuchi, T., 1980: Studies on aerodynamic surface roughness associated with drifting snow. *Mem. Fac. Sci. Kochi Univ.*, **2**, Ser. B, 13-37.

Kojima, K., 1967: Densification of Seasonal Snow Cover. *Physics of Snow and Ice*, part 1, ed. Oura, Sapporo, Inst. Low Temp. Sci., Hokkaido Univ., 929-952.

Komatsu, A., 2019: A simple snow cover model for avalanche warning systems. *Meteorological Research Note*, **241**, 593−604. (in Japanese)

Komatsu, A., and K. Nishimura, 2020: A Simple Snow Cover Model for Avalanche Warning. SOLA, 16, 246−251.

Lafore, J., J. Stein, N. Asencio, P. Bougeault, V. Ducrocq, J. Duron, and de Arellano, J. V.-G., 1998: The Meso-NH atmospheric simulation system. Part I: Adiabatic formulation and control simulations. Annales Geophysicae, 16, 90–109.

Launder, B. E., and D. B. Spalding, 1974: The numerical computation of turbulent flow. Comp. Meth. in Appl. Mech. and Eng., 3, 269-289.

Lehning, M., Fierz, C., Lundy, C., 2001: An objective snow profile comparison method and its application to SNOWPACK. *Cold Regions Science and Technology*, **33**, 253–261.

Lehning, M., Bartelt, P., Brown, B., Fierz, C., Satyawali, P., 2002: A physical SNOWPACK model for the Swiss avalanche warning Part II: Snow microstructure. *Cold Regions Science and Technology*, **35**, 147–167.

Lehning, M., H. Löwe, M. Ryser, and N. Raderschall, 2008: Inhomogeneous precipitation distribution and snow transport in steep terrain, *Water Resour. Res.*, **44**, W07404, doi:10.1029/2007WR006545.

Lundy, C., Brown, R., Adams, E., Birkeland, K., Lehning, M., 2001: A statistical validation of the snowpack model in a Montana climate. *Cold Regions Science and Technology*, **33**, 237–246.

McElwaine, J., A. Hachikubo, M. Nemoto, Y. Kaihara, T. Yamada and K. Nishimura, 2000: Observations and simulations of the formation of the faceted snow crystals in the week-layer of the 1998 Niseko haru no Taki avalanche, *Cold Reg. Sci. Technol.*, **31**, 235-247.

Morin, S., Horton, S., Techel, F., Bavay, M., Coléou, C., Fierz, C., Gobiet, A., Hagenmuller, P., Lafaysse, M., Ližar, M., Mitterer, C., Monti, F., Müller, K., Olef, M., Snook, J. S., van Herwijnen, A. and Vionnet, V., 2019: Application of physical snowpack models in support of operational avalanche hazard forecasting: A status report on current implementations and prospects for the future. *Cold Regions Science and Technology*, **170**, 237–246.

Mott, R., and M. Lehning, 2011: Meteorological modeling of very high-resolution wind fields and snow deposition for mountains, *J. Hydrometeor*, **11**, 934-949.

Murakami, S., K. Shunsuke, and Y. Ishida, 1989: Numerical simulation of room air flow with generalized curvilinear coordinates. *Journal of Architecture, Planning and Environmental Engineering*, **400**, 39-49. (in Japanese with English abstract)

Nakamura, H., 1988: Studies on the Settlement Force of Snow as a Generation Mechanism. *Report of the National Research Center for Disaster Prevention*, **41**, 361-385.

Patankar, S. V., 1981: Numerical Heat Transfer and Fluid flow. Hemisphere, Washington, D. C. 193 pp.

Perla, R. 1977: Slab avalanche measurements. *Canadian Geotechnical Journal*, **14**, 206-213.

Oikawa S., Tomabechi T., and Ishihara T., 2007: Study of Wind Tunnel on Snowdrift around Buildings, *J. of Snow Eng. of Japan.*, **23**(2), 13-32 (in Japanese with English abstract).

Orlanski, U., 1976: A simple boundary condition for bounded hyperbolic flows. *J. Comput. Phys.*, **21**, 251-269.

Osabe, T, Izumi, K., and Kawashima, K., 2008: The characteristic of avalanche cases in 2007/08 winter. Seppyo Hoku-shin-etsu, **28**, 62. (in Japanese)

Saito, Y., Enomoto, H., 2003: Development and application of snow cover model simulation., *Annual Report on Snow and Ice Studies in Hokkaido*, **22**, 33–36 (in Japanese).

Sato, T., and F. Yasuda, 2014: A numerical simulation of snowdrift around blower snow fence. *The proceeding of cold region technology conference*, **30**, 47-52. (in Japanese)

Suizu, S., 2002: Calculation model for stability index of snow for dry surface snow avalanche derived by heavy snowfall. *Seppyo*, **64**, 15–24 (in Japanese with English abstract).

Sommerfeld, R. A., 1984: Instructions for using the 250 cm^2 shear frame to evaluate the strength of a buried snow surface., *U.S. For. Serv. Res.* Note RM-446, 1-6.

Schmucki, E., Marty, C., Fierz, C., Lehning, M., 2014: Evaluation of modelled snow depth and snow water equivalent at three contrasting sites in Switzerland using SNOWPACK simulations driven by different meteorological data input. *Cold*

Regions, **99**, 27–37.

The Meteorological Society of Japan, 1985: Meteorological fluid experiments. *Meteorological Research Note*, **152** (in Japanese).

Tsutsumi, T., 2009: Snowdrift Wind tunnel., *Wind Engineers*, **34**(1), 36-41 (in Japanese).

Uematsu, T., K. Nakata, K. Takeuchi, Y. Arisawa, and Y. Kaneda, 1991: Three-dimensional simulation of snowdrift. *Cold Regions Science and Technology*, **20**, 65-73.

Vionnet, V., Brun1, E., Morin, S., Boone, A., Faroux, S., Le Moigne, P., Martin, E. and Willemet, J.-M., 2012: The detailed snowpack scheme Crocus and its implementation in SURFEX v7.2, *Geosci. Model Dev.*, **5**, 773–791.

Willmott, C. J., Wicks, D.E., 1980: An empirical method for the spatial interpolation of monthly precipitation within California. Phys. Geogr. 1, 59-73.

Xue, M., K. K. Droegemeier, V. Wong, A. Shapiro, and K. Brewster, 1995: ARPS version 4.0 user's guide, 380 pp., *Cent. for Anal. and Predict. Of Storms, Univ. of Okla.*, Norman, Okla.

Yamanoi, K, Endo, Y., 1998: Measurement of the compactive viscosity coefficient of wet snow. *Preprints of the 1998 Conference Japanese Society of Snow and Ice*, 86.

Yamanoi, K., Endo, Y., 2002: Dependence of shear strength of snow cover on density and water content. *Seppyo*, **64**, 443–451 (in Japanese with English abstract).

Yamanoi, K., Takeuchi, Y., Murakami, S., 2004: Estimate of snow stability index using "Push Pull Gauge". *Seppyo*, **66**, 669–676 (in Japanese with English abstract).

Yamazaki, T., 2001: A one-dimensional land surface model adaptable to intensely cold regions and its applications in Eastern Siberia. *J. Meteor. Soc. Japan*, **79**, 1107–1118.

Appendix A

Main morphological grain shape classes. (Fierz et al., 2009)

Class	Symbol	Code
Precipitation Particles	+	PP
Decomposing and Fragmented precipitation particles	⁄	DF
Rounded Grains	●	RG
Faceted Crystals	□	FC
Depth Hoar	∧	DH
Surface Hoar	∨	SH

This table displays the main morphological classes of grain shapes. The IACS (the International Association of Cryospheric Sciences) working group defined main grain shape classes are classified by using either a symbol or a unique two-letter upper case abbreviation code. The characteristics of snow types are as shown below.

PP is for classifying the first, usually short lived, stage of seasonal snow on the ground. DF has characteristic shapes of precipitation particles still recognizable; often partly rounded. RG is rounded, usually elongated particles. FC is solid faceted crystals; usually hexagonal prisms. DH is hollow skeleton type crystals; usually cup-shaped. SH is striated, usually flat crystals; sometimes needle-like.

Appendix B

Properties of the snow layer measured and calculated by the SSCM. Measured and modeled snow heights are each assigned a unit height. Profiles of snow temperature (upper), density (middle), shear strength converted from snow hardness (lower).

B-1. The Mikuni pass, Kamikawa, Hokkaido

1) 0900 JST 27 January 2013

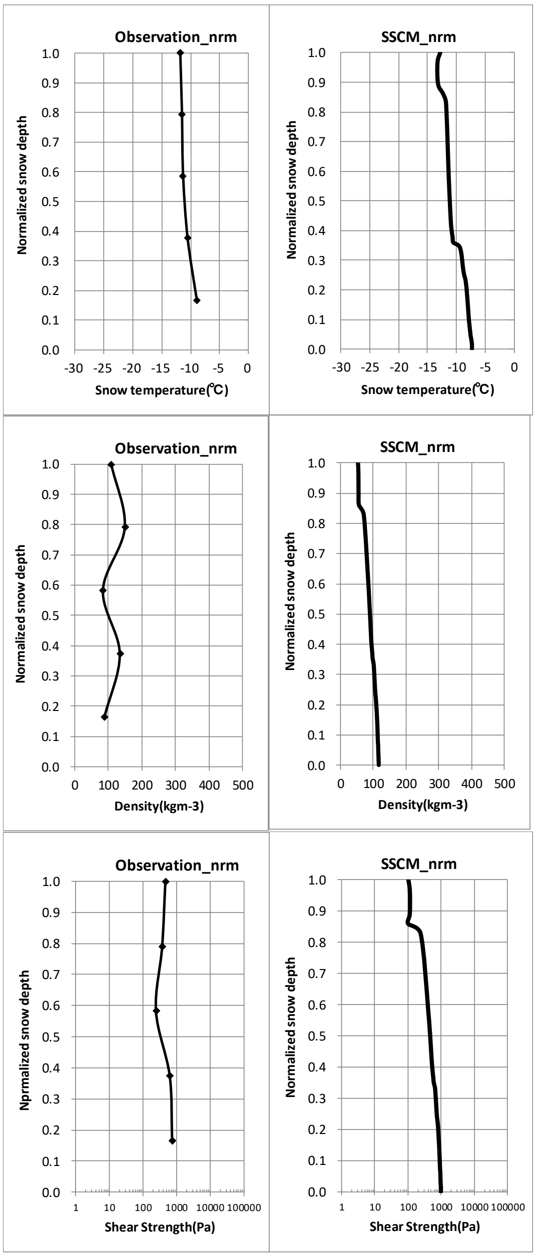

2) 1600 JST 27 January 2013

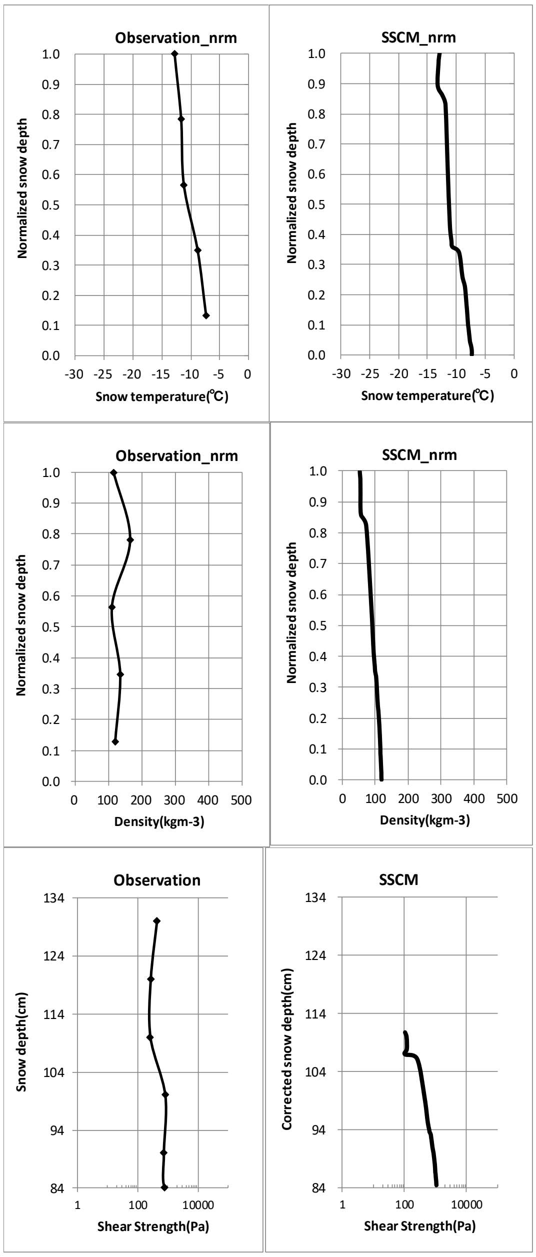

3) 0800 JST 28 January 2013

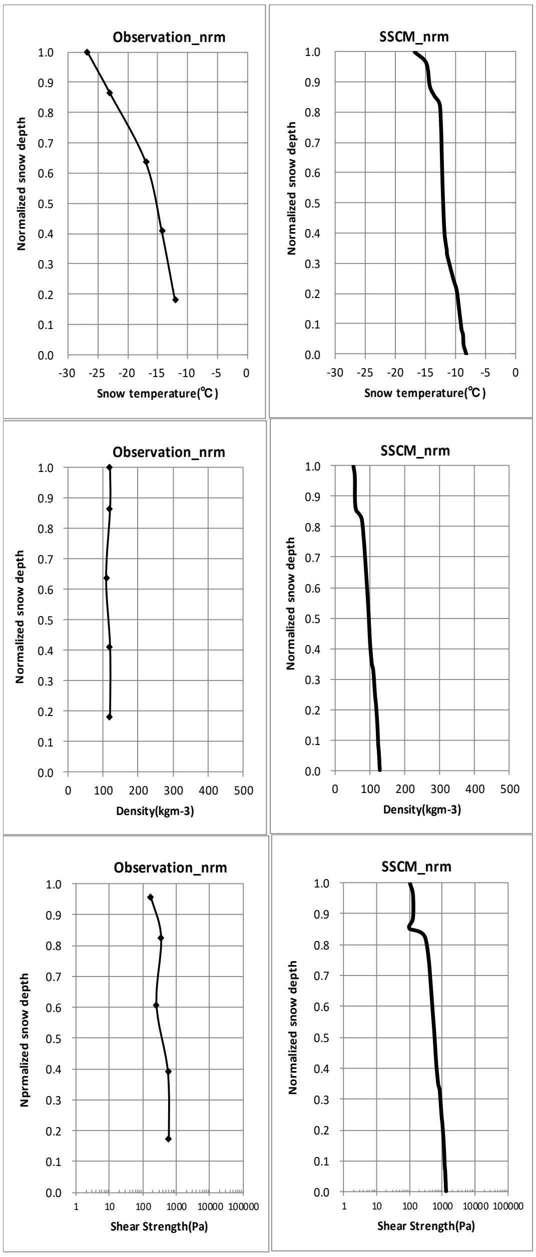

4) 1200 JST 28 January 2013

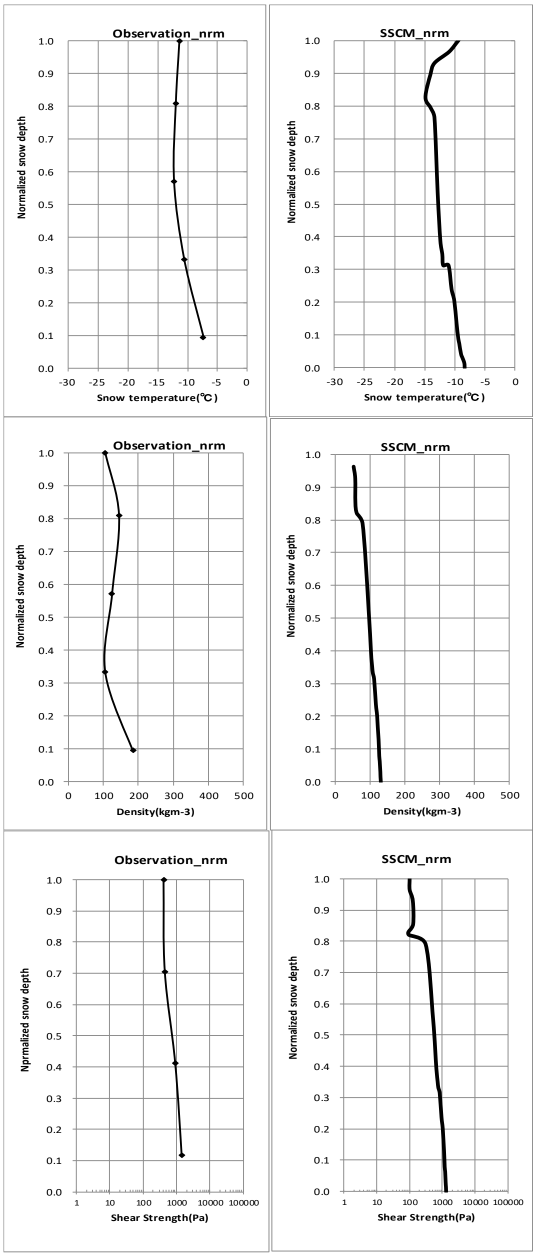

5) 0800 JST 29 January 2013 6) 1200 JST 29 January 2013

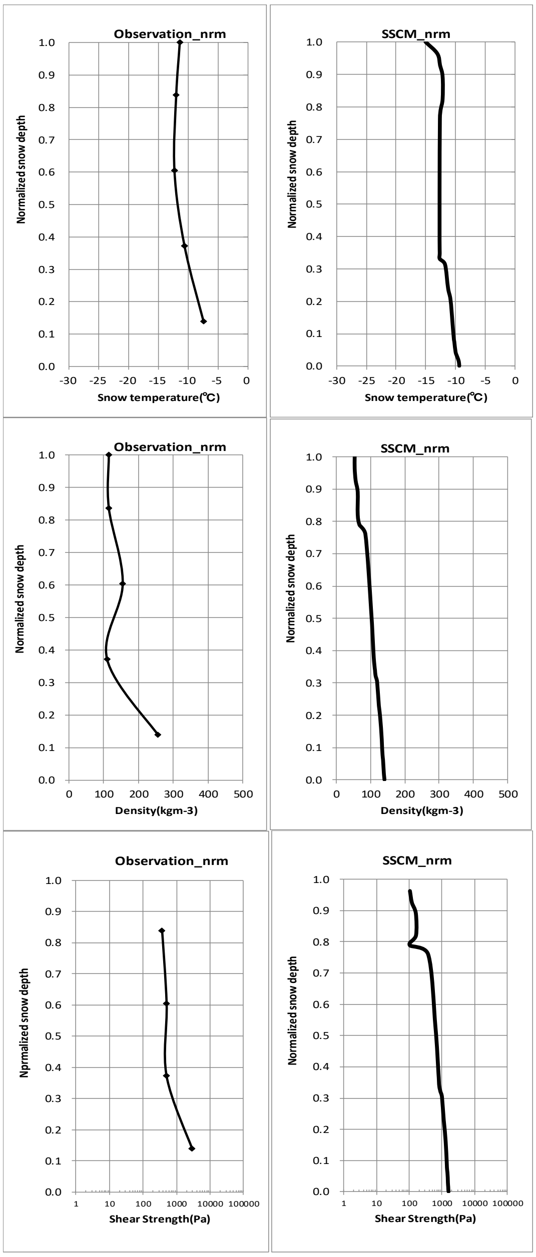

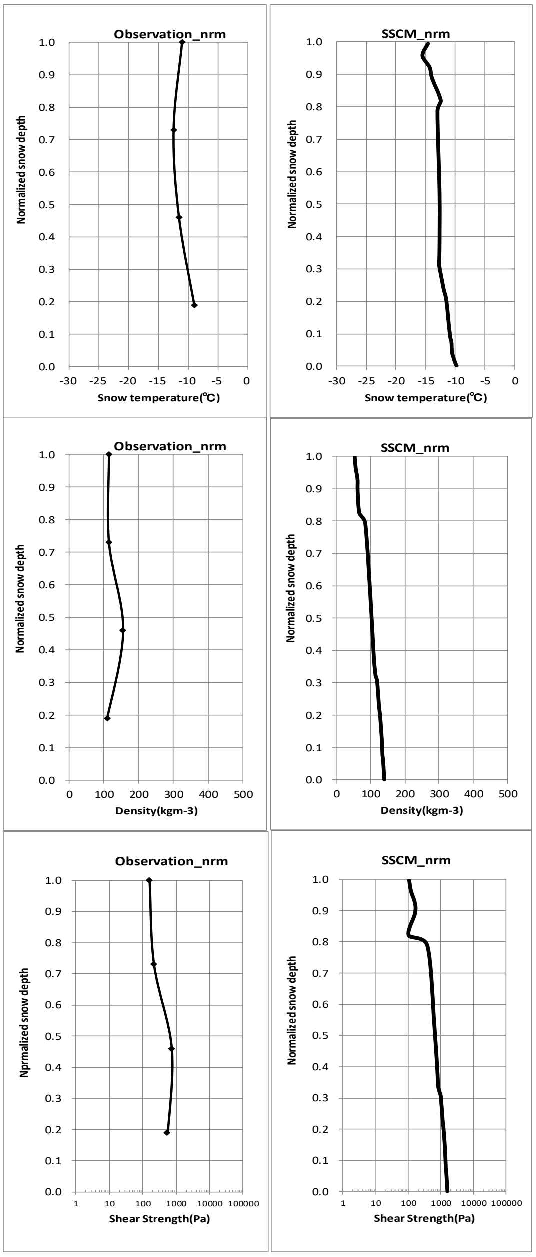

7) 1500 JST 29 January 2013

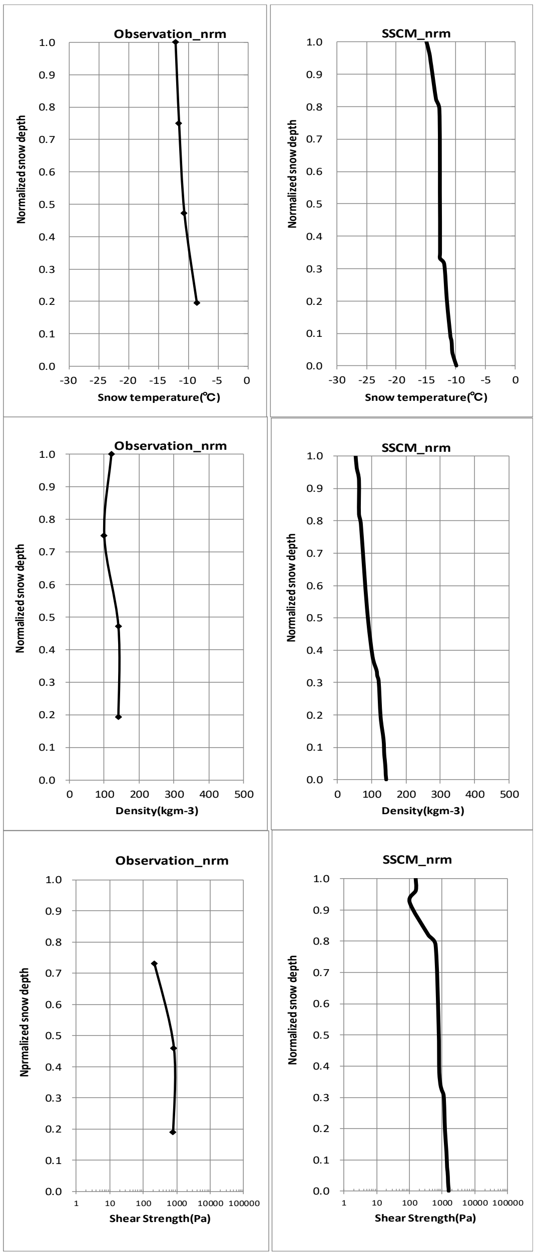

B-2. Properties of the snow layer measured calculated using data from the Mikuni AWS at 0800 28 January, 2013 and simulated by the SSCM and SNOWPACK.

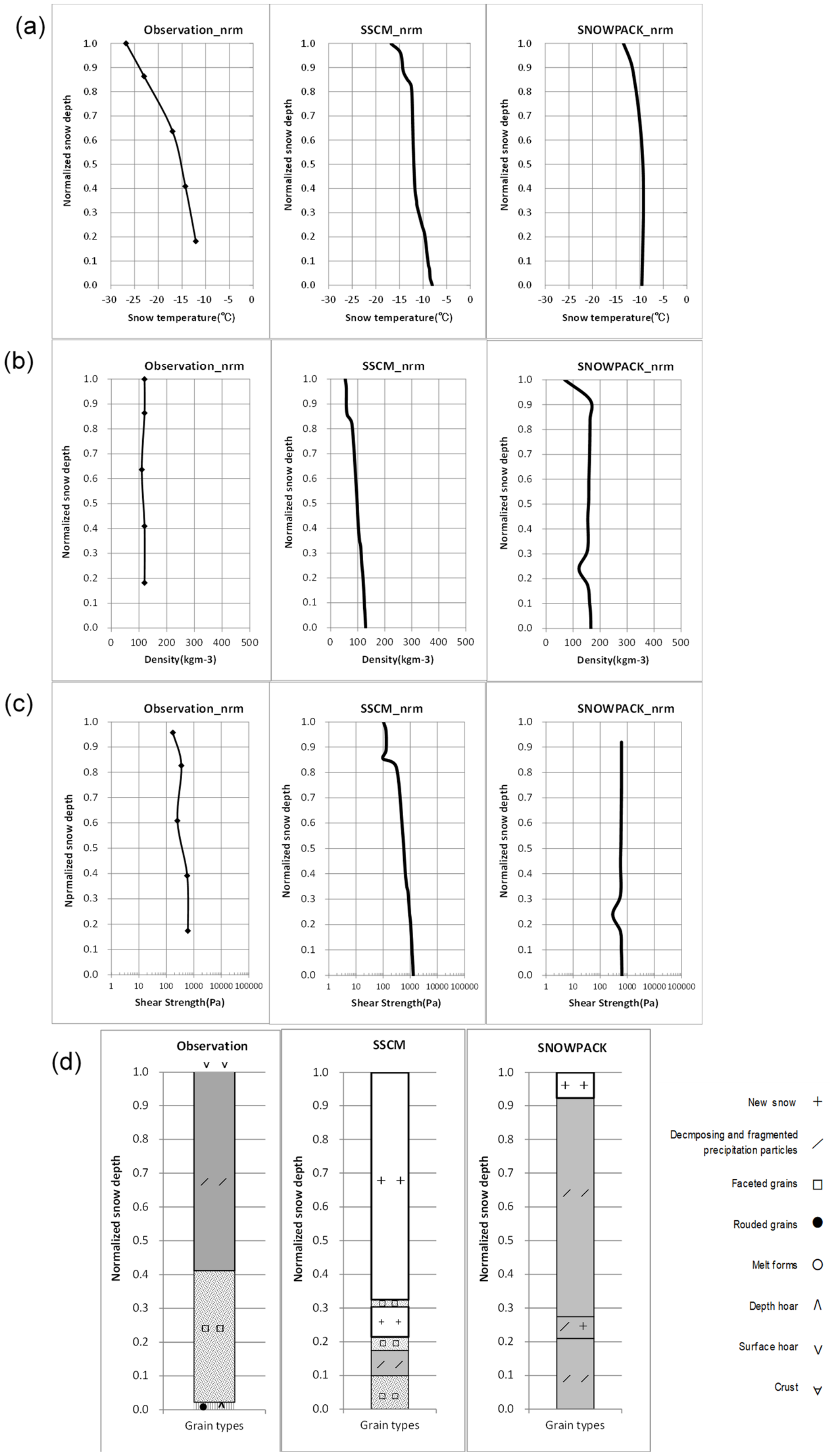

Measured and modeled snow heights (0.44 m, 0.25 m (SSCM) and 0.26 m (SNOWPACK), respectively) are each assigned a unit height. Profiles of (a) snow temperature, (b) density, (c) shear strength converted from snow hardness, and (d) grain types are shown.

B-3. The Kiritachi pass, Rumoi, Hokkaido

1) 1600 JST 12 February 2013　　　　2) 1400 JST 9 March 2014

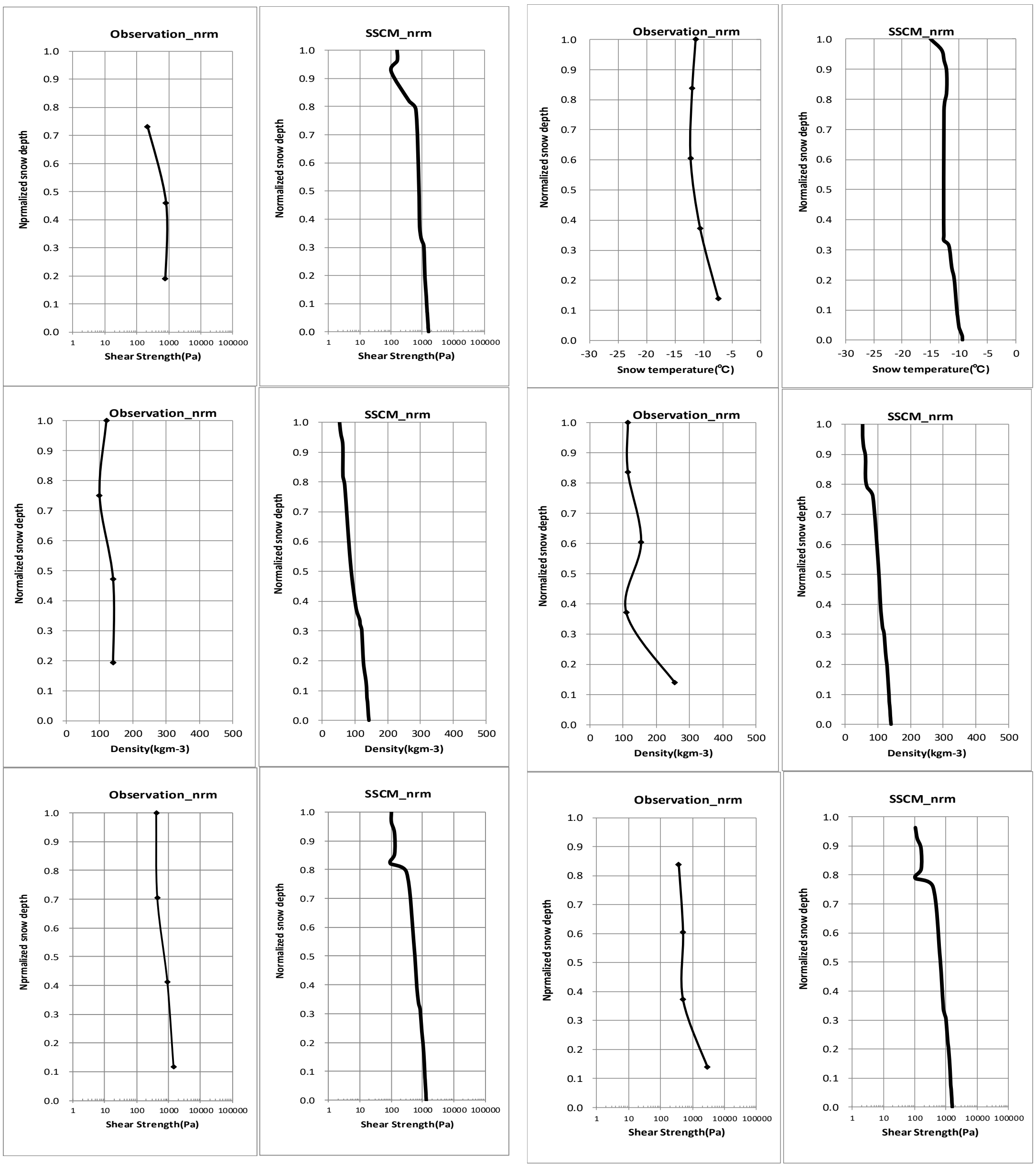

Appendix C

SSCM calculation for the avalanche incidents

In the following, case number corresponds to one in Table 2.2..

Case1: 2004/1/14 The Sekihoku pass, Kamikawa, Hokkaido

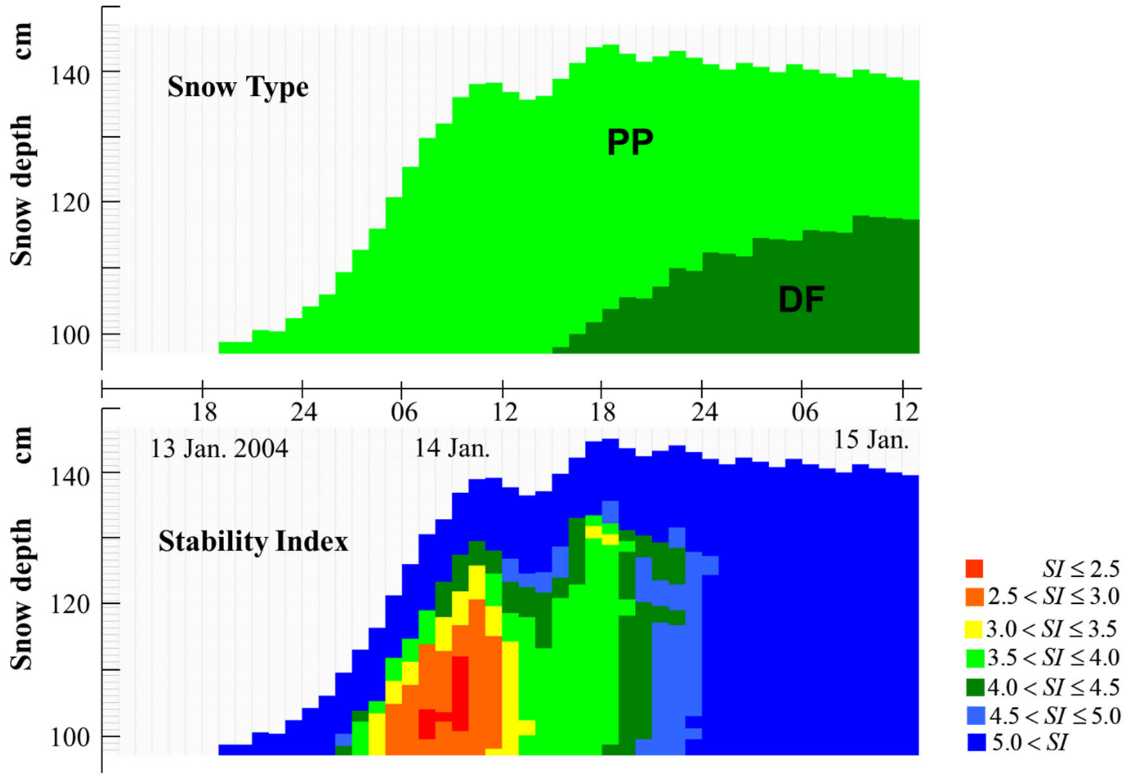

Time series of snow type (above) and SI (below) calculated using the SSCM for January 13–15, 2004. Air temperature and snow depth at the Sekihoku pass AWS was used for this simulation.

Case2: 2008/2/13 Wakkanai, Hokkaido

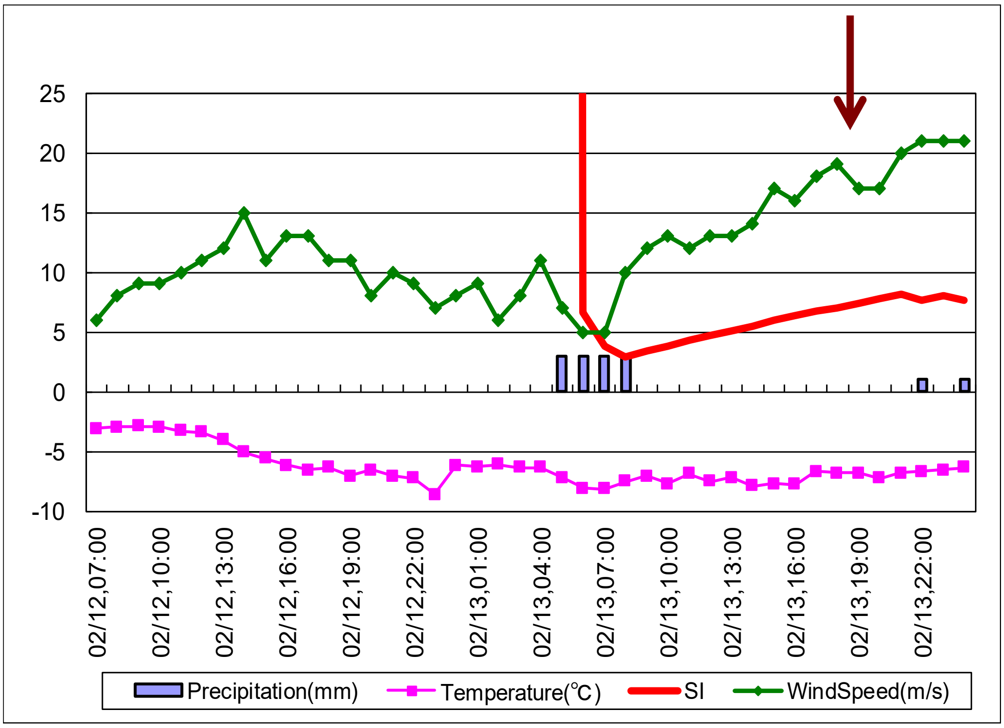

Observation at Soyamisaki AMeDAS (Precipitation, Temperature, Wind speed) and SSCM output. Arrow indicates the time when the avalanche broke out.

Case3: 2010/2/19 The Notsuka pass, Tokachi bureau, Hokkaido

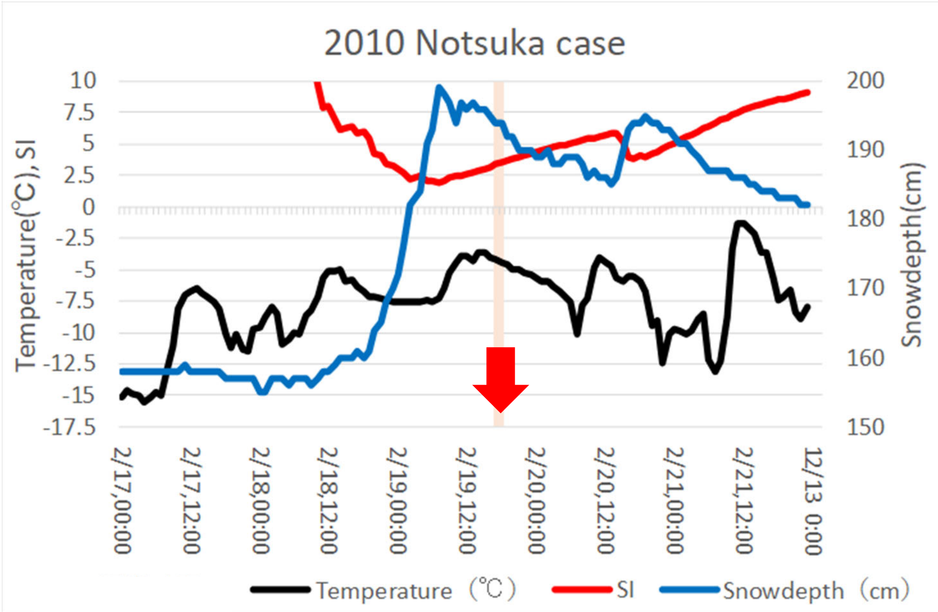

Time series of air temperature, snow depth, snowfall at Notsuka Pass AWS, and SI calculated using the SSCM for February 17–5, 2010.

An avalanche occurred at the time indicated by the arrow and ten automobiles on the road were involved.

Case4: 2011/1/24 Bekkari, Rumoi, Hokkaido

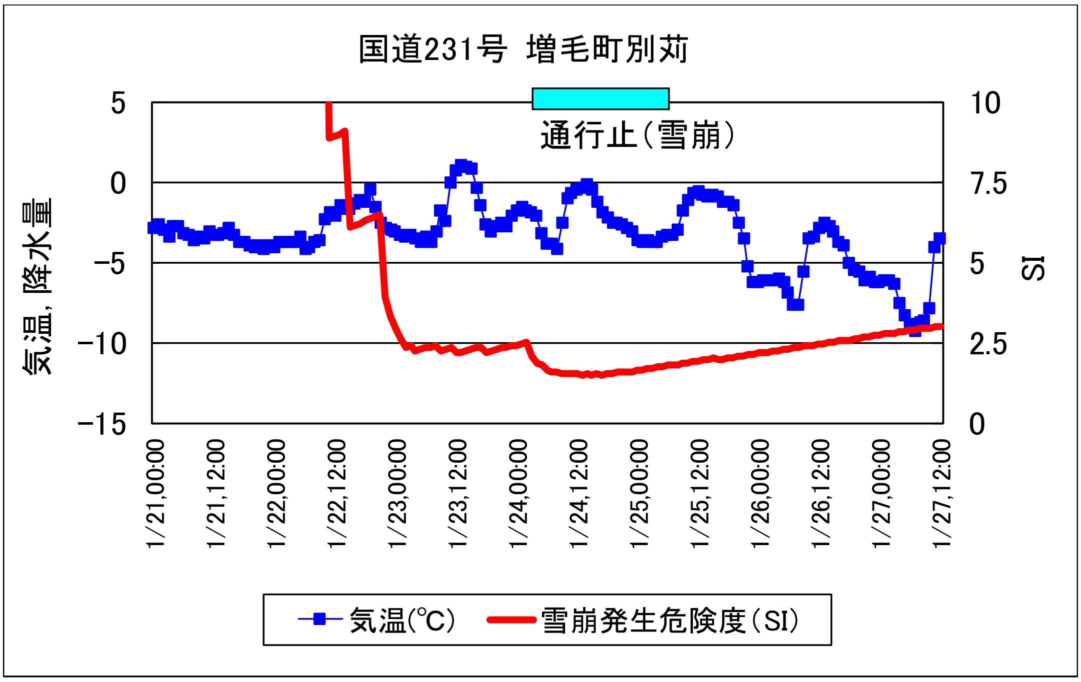

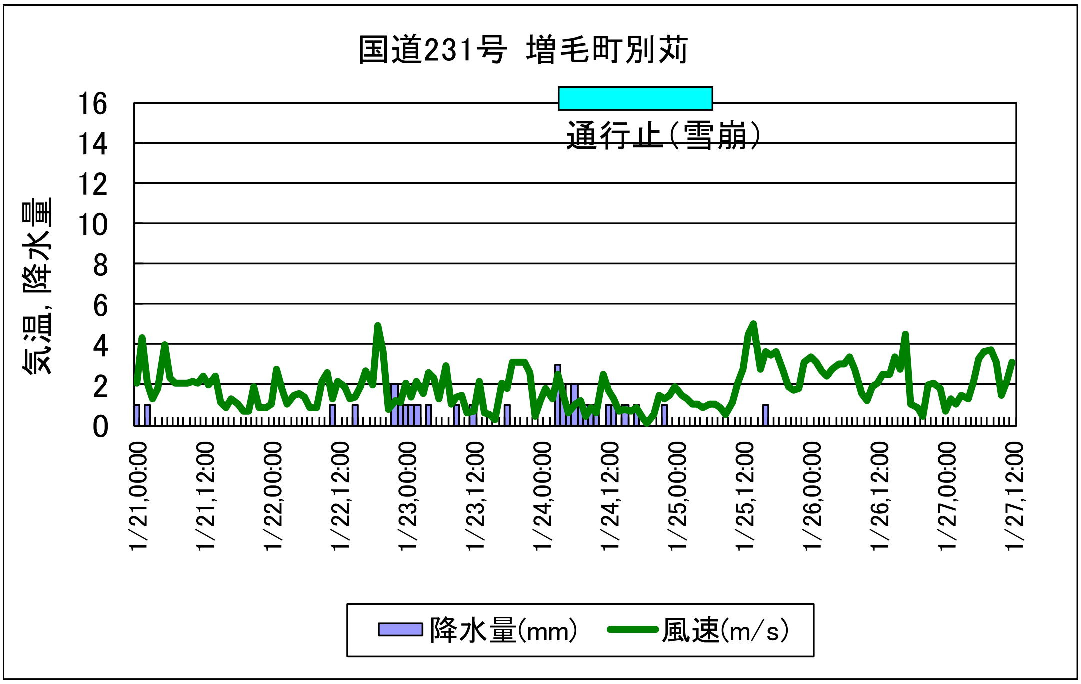

Time series of air temperature (upper), precipitation, and wind speed (below) at Bekkari AWS from 21 to 27 January, 2011. Although the avalanche release time is not known precisely, Route231 was closed for the period indicated as blue bar. SI calculated with the SSCM is also shown in the figure.

Case5: 2012/12/11 The Mikuni pass, Kamikawa, Hokkaido

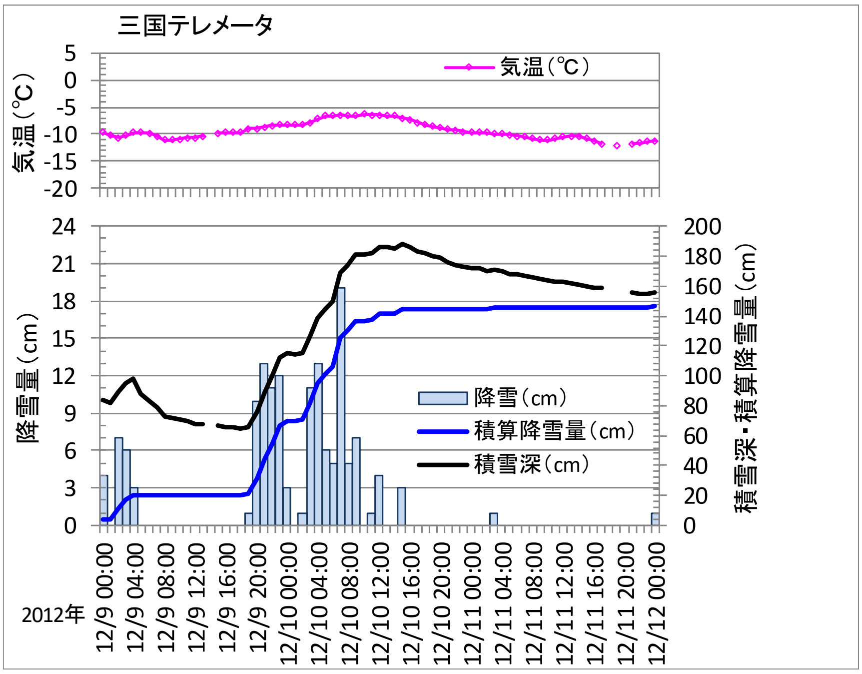

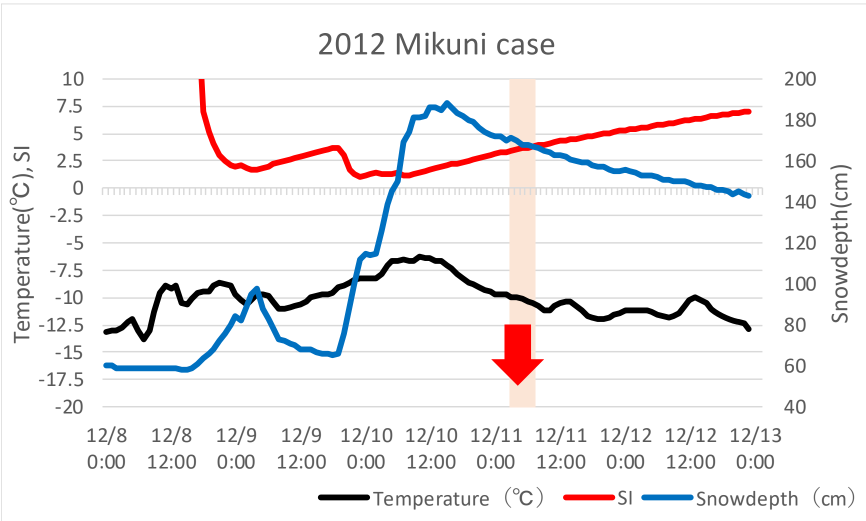

Upper figure shows the time series of weather conditions at Mikuni AWS from 9 to 11,2014. Lower one indicates the SI calculated with the SSCM together with the air temperature, and the snow depth

Case8: 2020/2/1 Mt. Pineshiri, Kamikawa, Hokkaido

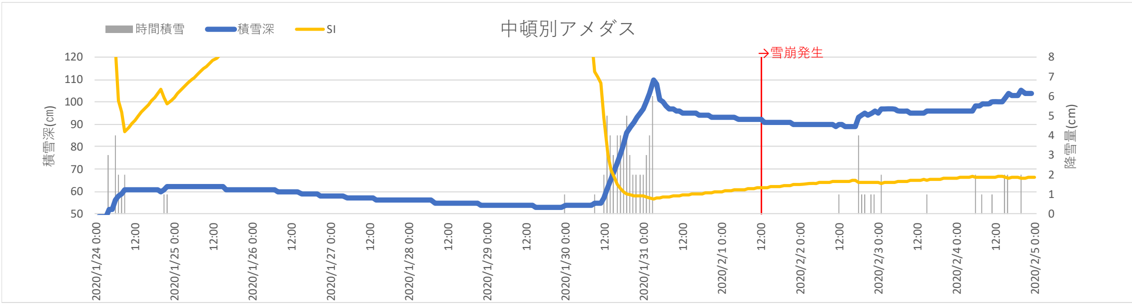

Upper picture shows the air temperature and the wind speed at Nakatonbestu AMeDAS from 24th January to 4th February 2020.

Lower one indicates the observed snow depth, the snow fall amount and the SI calculated with the SSCM. Avalanche broke out at 12h on 1st February.

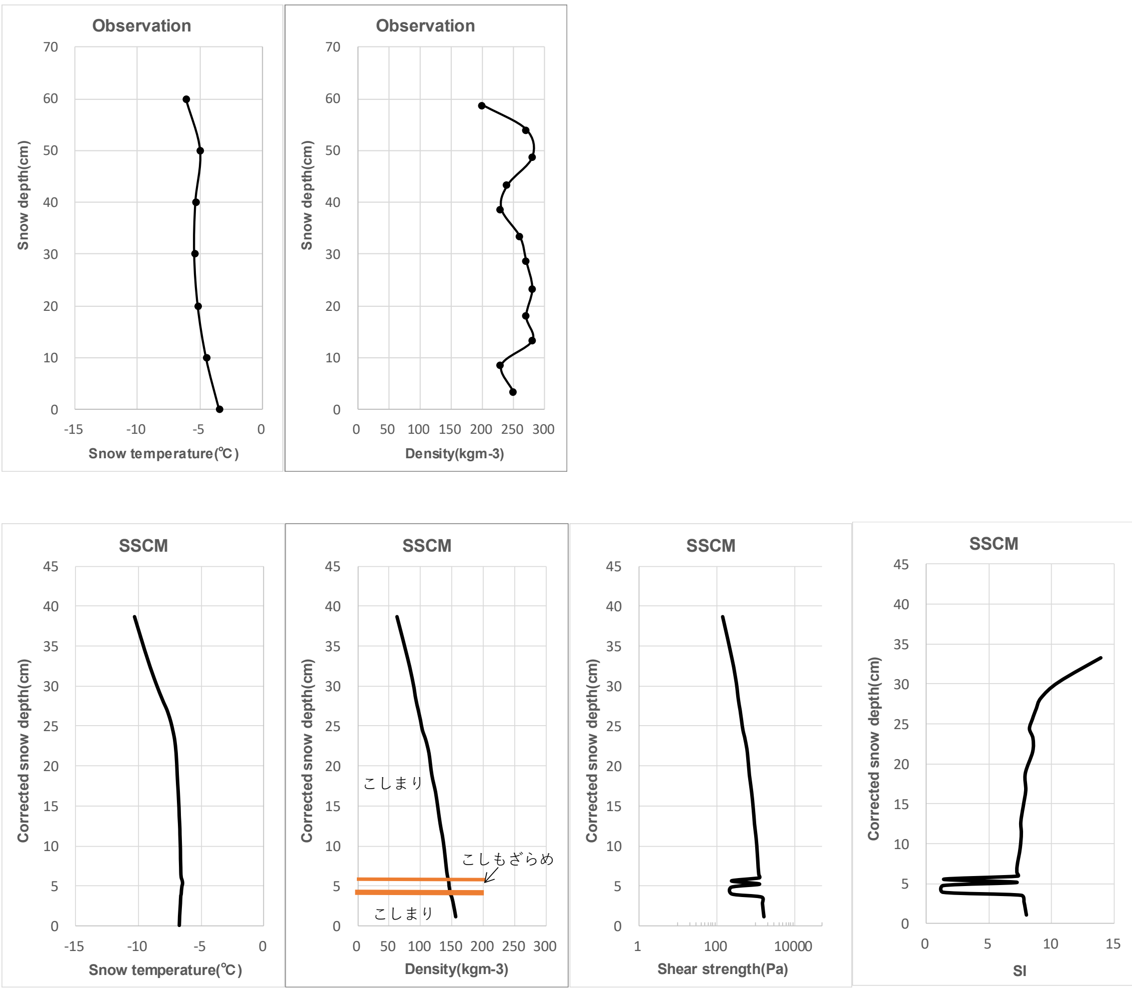

Properties of the snow layer measured (upper, snow temperature and density) and calculated by the SSCM (lower, snow temperature, density, shear strength, and SI) using the data from Nakatonbetsu AWS at 1200 JST 2 February 2020.

Case9: 2020/3/6　The Notsuka pass, Tokachi, Hokkaido

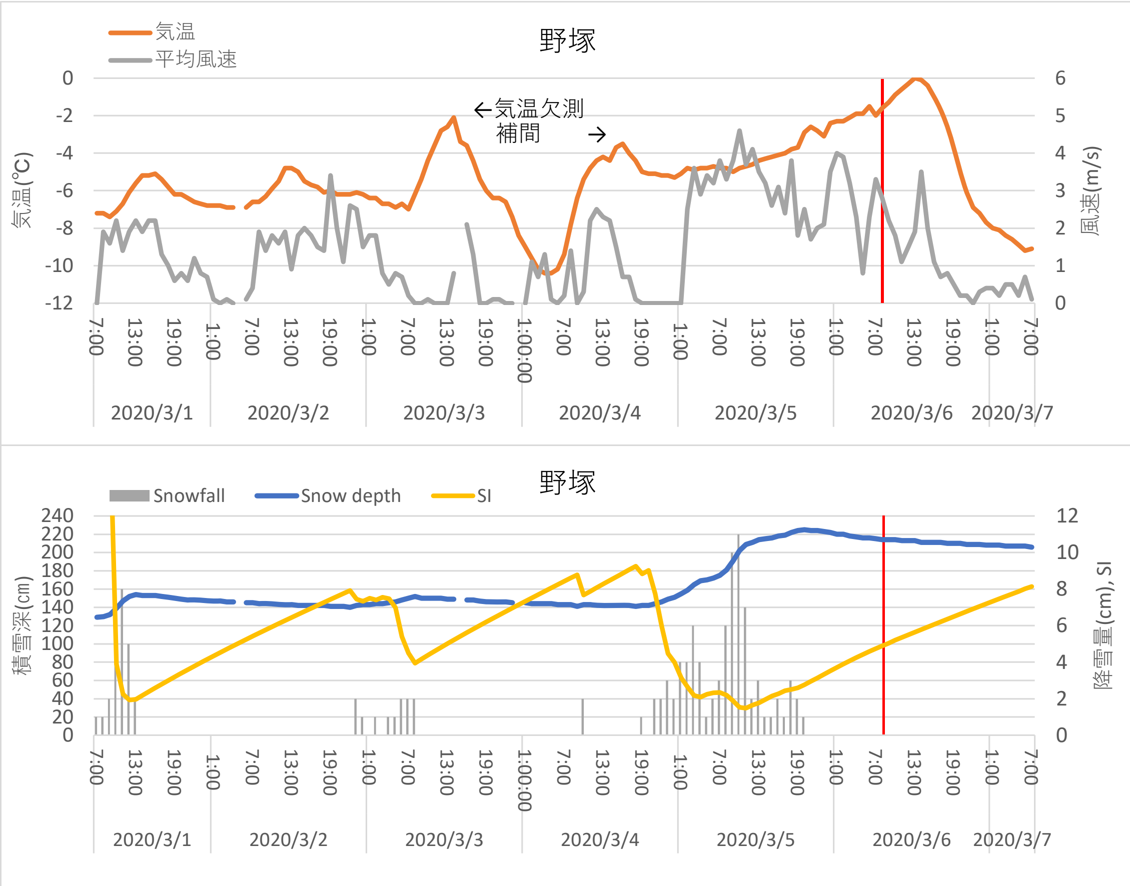

Time series of observed meteorological conditions and SI calculated using the the SSCM for March 1 to 7, 2020 at Notsuka Pass AWS.

Upper figure shows air temperature and wind speed, and lower one displays snow depth, snowfall and SI. Air temperature data during the missing period of from 3 to 4 March were interpolated by JMA GPV.

Case11: 2014/2/9 Ooisawa, Yamagata

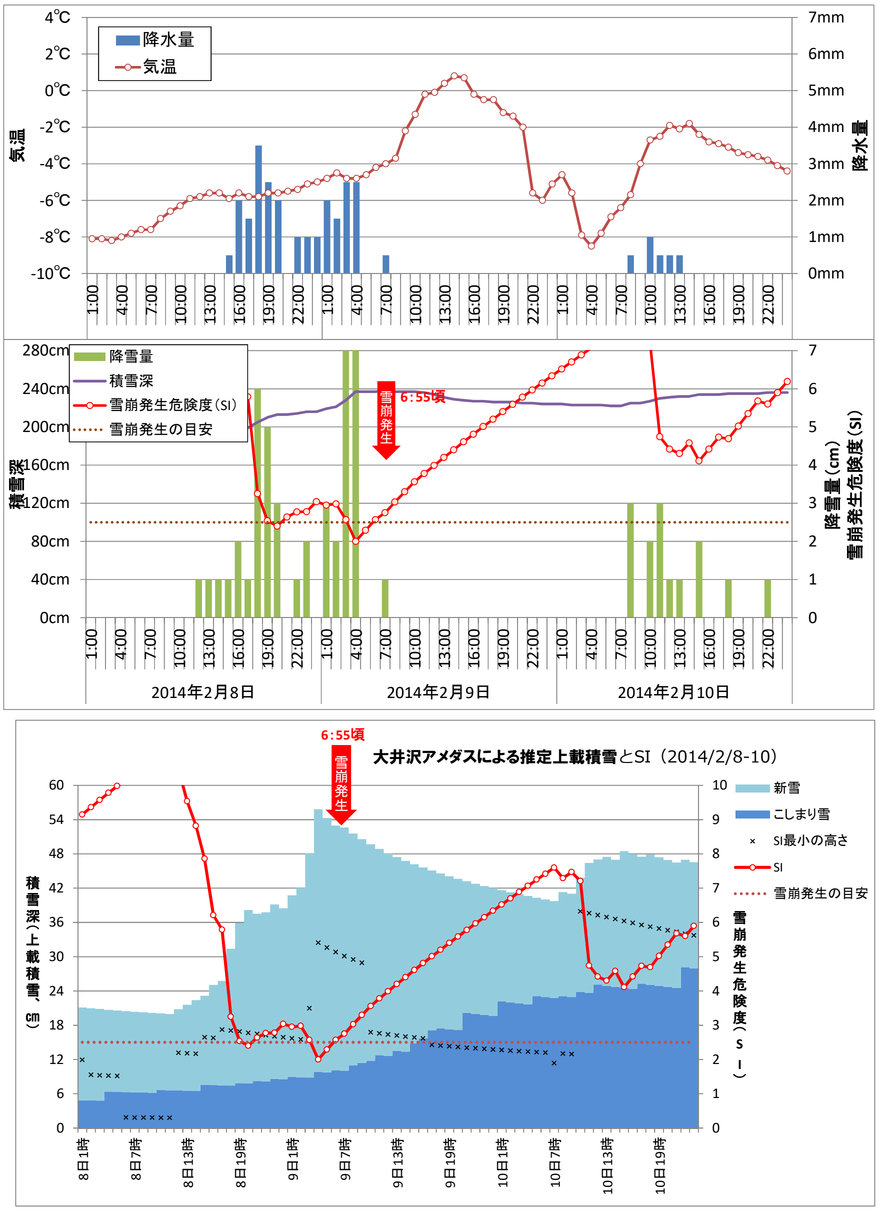

Time series of weather conditions at Ooisawa AMeDAS and SI calculated using the SSCM from 8 to 10 March, 2014. Upper figure shows the observed precipitation and air temperature. Lower one displays snow fall amount, snow depth and SI. Cited from Komatsu (2019).

Properties of snowpack profile (snow grain types and SI) calculated using the SSCM. Cited from Komatsu (2019).

Case12: 2010/12/31 Okudaisen, Tottori Prefcture

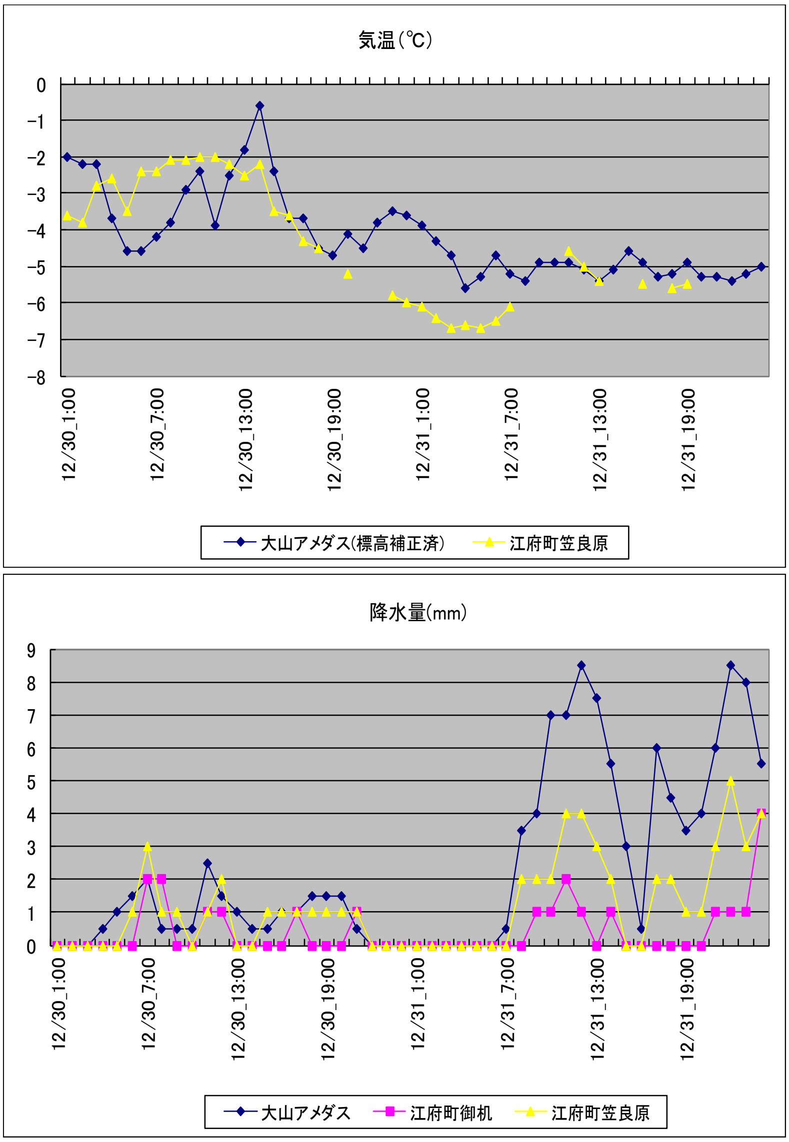

Time series of weather conditions at Ooyama AMeDAS and two AWSs in the neighborhood from 30 to 31 December, 2010. Upper figure shows the air temperature and the lower one displays the precipitation amount. Since air temperature has not been measured at Ooyama AMeDAS, it was estimated with the data at Yonago AMeDAS and the altitude difference between two stations.

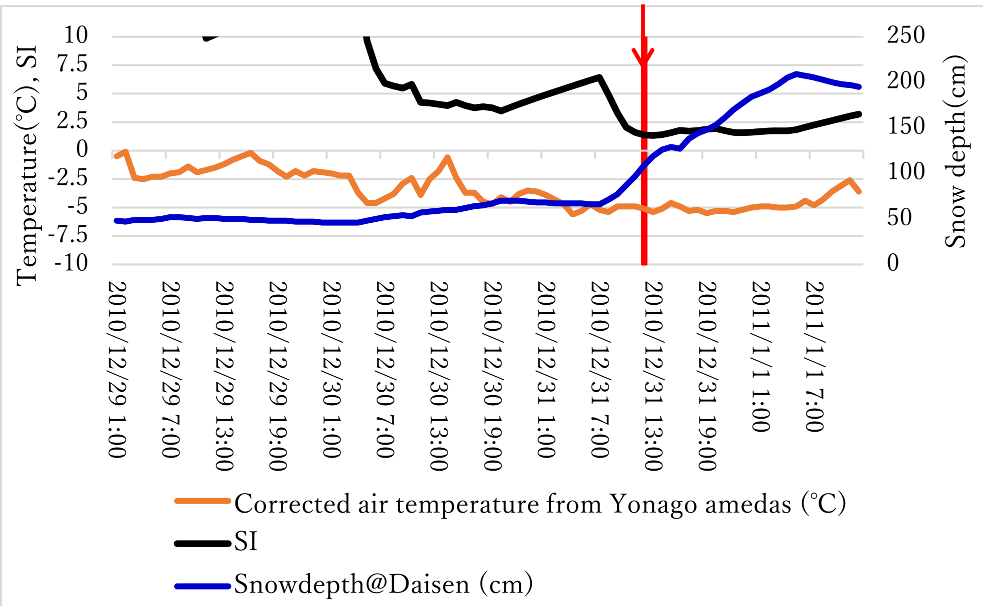

Time series of air temperature, snow depth, snowfall at Okudaisen AWS, and SI calculated using the SSCM from 29 December, 2010 to 1 January, 2011. Two snow avalanches broke out between 1200 JST and 1400JST 31 December.

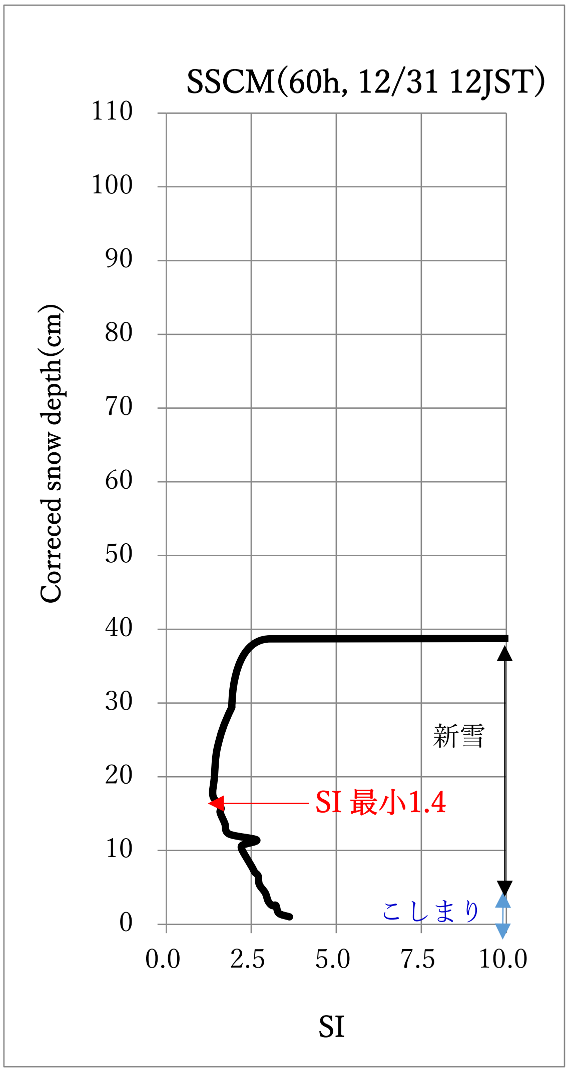

Properties of the snow layer (grain type and SI) simulated by the SSCM.

Appendix D

Moving observations results for all cases in Niseko town

In Niseko town, the observation (2016-Run 3) under rain and snow on 20 October 2016. The observation is conducted 1103 to 1219 JST.

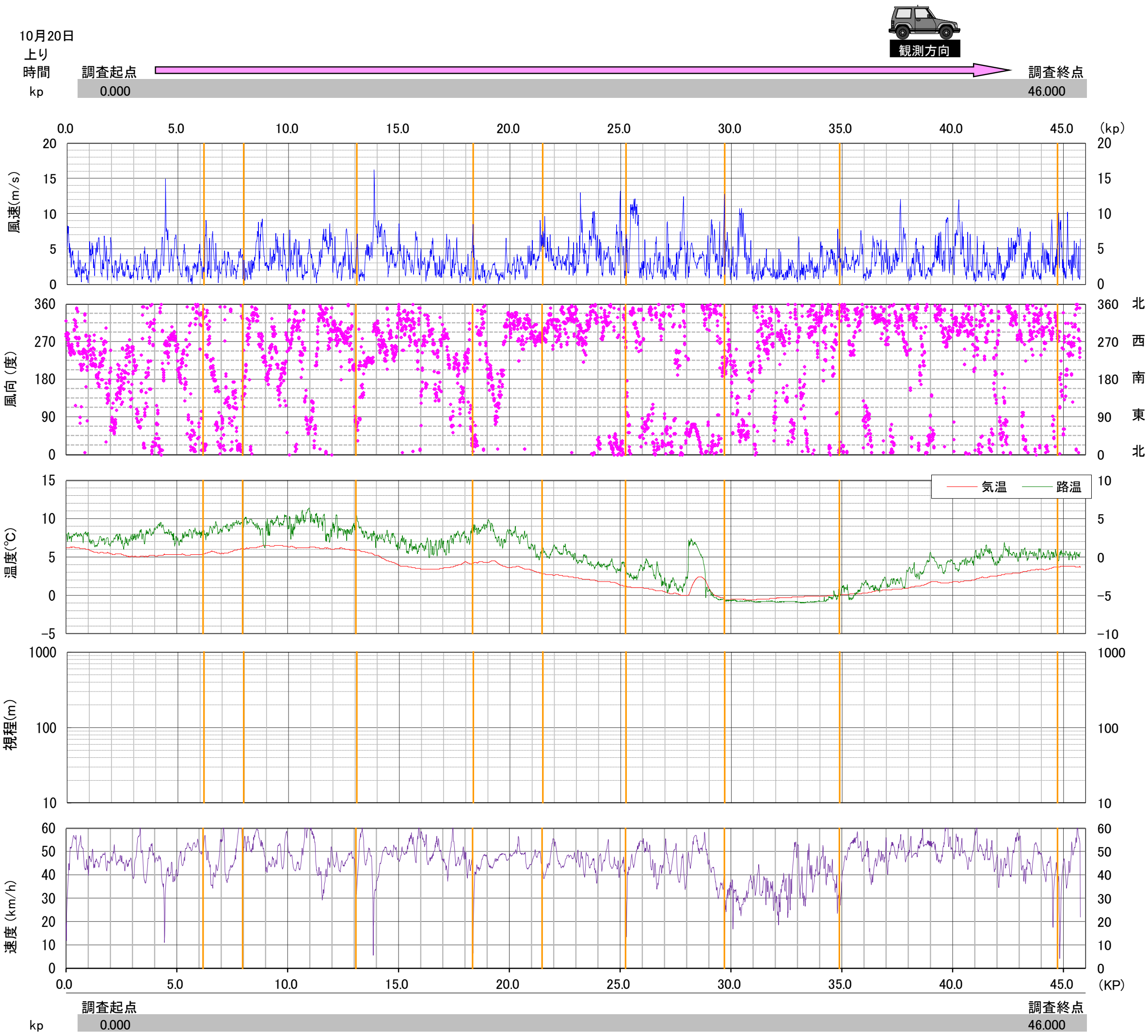

Fig. D.1. The moving vehicle observation results for Run 2016-3. The rime series of wind spend and direction, air temperature (left-hand scale) and road temperature (right-hand scale), visibility, and car’s moving speed from the top to the bottom.